EXPERIMENTS AND THEORY ON A BIO-INSPIRED FILM-TERMINATED MICRO-FIBER ADHESIVE

A Dissertation

Presented to the Faculty of the Graduate School

of Cornell University

In Partial Fulfillment of the Requirements for the Degree of

Doctor of Philosophy

by

Lulin Shen

January 2009

EXPERIMENT AND THEORY ON A BIO-INSPIRED FILM-TERMINATED MICRO-FIBER ADHESIVE

Lulin Shen, Ph. D.

Cornell University 2009

The structure considered in this thesis is a simple array of micro-pillars terminated by a continuous thin film. The normal adhesive properties of this structure are studied in chapters 2 and 3. In chapter 2, we present experimental data which shows that adhesion hysteresis, measured in cyclic indentation experiments, can be nearly five times the absolute work of adhesion of a flat control sample. To demonstrate how a purely elastic system can be dissipative, we present a model which shows that adhesion hysteresis develops due to trapping of the interface crack by fibril edges. Since a compliant interface promotes good contact, we present a contact mechanics model to predict the contact compliance of fibrillar structures. In chapter 3, we studied the effect of geometry on the crack trapping mechanism using a two dimensional finite element model. Several experimental observations are explained by this model: (1) the work to separate a unit area of the interface (W^+) is larger than the work of adhesion (W_{ad}) of the flat control sample; (2) the work to heal a unit area of the interface (W^-) is smaller than the work of adhesion of the flat control sample; (3) W^+ increases with fibril spacing; (4) W^+ decreases with film thickness; (5) W^+ decreases with fibril height.

The response of our film-terminated micro-fiber array under shear is studied in chapter 4. These friction experiments are carried out by dragging the samples indented by a spherical glass indenter with a constant normal force. Our experiments shows that

the force requires to initiate sliding between the indenter and the sample, its static friction, is strongly enhanced compared to a flat unstructured control sample. This enhancement is due to the crack trapping mechanism and increases with inter-fibril spacings. Our experiment shows that the transition from static to dynamic friction is due to a mechanical instability. A surprising result is that the dynamic friction is independent of the fibril spacing. Furthermore, the dynamic friction is practically the same as that of control sample. A preliminary explanation of these observations is given.

The friction response of our fibrillar samples is studied using different indenters in chapter 5. We investigate the effect of displacement rates on friction properties. We study in detail the mechanism governing both the static and dynamic friction. We demonstrated that the static friction and adhesion are correlated and can be attributed to the crack trapping mechanism. During steady sliding of the indenter, we observed micro stick-slip in the contact region. The contact shear stress as well the nominal contact area are found to be independent of fibrillar spacing and loading displacement rate. Our data supports a simple model which states that the dynamic friction force is a constant shear stress multiplied by the nominal contact area.

BIOGRAPHICAL SKETCH

Lulin Shen was born on February 14, 1979, in Shanghai, P.R. China. After six years of elementary and three years of middle school, she finished her high school education in Xiang-Ming high school. Then she attended Fudan University, where she received the Bachelor of Science degree of applied mechanics. In 2001, she was accepted by the department of engineering and mechanics and science at Pennsylvania State University (University Park) where she received the Master Science degree before she joined Cornell University.

To my loving mother, Ms. Jingxian Zhuang, who passed away in 1998.

May her soul rest in peace.

ACKNOWLEDGMENTS

I would like to thank the many people who have helped me throughout my time at Cornell and have enabled me to complete this work. Among these people, I am most indebted to my advisor, Professor Chung-Yuen Hui, who has helped me at nearly every step along the way. Words can not express how grateful I am. His enthusiasm, insights and intelligence greatly contribute to this work as well as to my interest in scientific research. I also highly appreciate his patience and all the time he spent guiding me and helping me correct the English in my manuscripts. It has been a great pleasure to have worked with him. What I learned from him will benefit me for rest of my life.

I would also like to thank the other members of my special committee, Professor Stuart Leigh Phoenix and Professor Michael Thompson. Their courses provided me with valuable knowledge. In addition, my occasional consultations with them were also very helpful and pleasure experience.

Another who has played an important role in this work, especially the experimental part, is Professor Anand Jagota of Lehigh University. I spent one and half year working in his lab. Before that, I did not have much experiment experience. It is his generous and patient guidance that make the completion of this work possible and make a reasonable experimentalist out of me.

Outside my special committee, I acknowledge Nicholas Glassmaker, Professor Hui's former student, for his brilliant invention of this film-terminated fibrillar sample which provides interesting subject to this work. I also wish to thank former and fellow students of Professor Hui, Tian Tang, Vijayanand Muralidharan, Jingzhou Liu, Venkat Krishnan and Rong Long for their helpful comments and discussion throughout this

work. In addition, I am also very grateful to Shilpi Vajpayee, my lab mate in Lehigh University, for her help and aid during the entire experiments.

Not to be forgotten are those whose aid is precious and dear to me. The first special thanks goes to my loving husband Yuqing Liu for making the past four years more memorable to me. It is his love and patience helped me build up my confidence and overcome many difficulties. I also would like to thank my farther, Yukang Shen, for his selfless love and support in spite of the physical distance.

Finally I acknowledge Department of Energy and National Science Foundation for their support on the project. And I also wish to thank Cornell Nanoscale Facility for their permission of access to its vast laboratory resources and facilities. Without their help, this work would not have been possible.

TABLE OF CONTENTS

LIST OF FIGURES

LIST OF TABLES

LIST OF ABBREVIATIONS

CB……cantilever beam

DCB…….……double cantilever beam

FEM…….…..finite element method

JKR…….……...Johnson-Kendall-Robert

PMS……polydimethylsiloxane

PSA……. pressure sensitive adhesives

SAM……..……self assembly monolayer

SB……Savkoor-Briggs

PREFACE

This dissertation presents four chapters (chapter 2, 3, 4 and 5) that represent work on two individual projects in the area of adhesion of fibrillar samples. These chapters were originally written as separate papers; therefore the same symbol in different chapters may have different physical meanings, although effort was made to use consistent notation throughout. Reference numbers in a given chapter only correspond to the list at the end of that chapter.

CHAPTER 1

INTRODUCTION

Many small insects and animals use hierarchical fibrillar structures on their feet to make contact and adhere to various surfaces [1, 2]. For example, a Tokay Gecko has nearly six million hairs or setae, each of which is 30 to 130 μm long. Each seta contains hundreds of projections or pillars terminating in 0.2 to 0.5 μm spatula shaped pads [3, 4]. They can adhere to a wide variety of surfaces using materials considerably stiffer than those used in pressure sensitive adhesives (PSAs). However, unlike PSAs, 'setal' adhesion surfaces are reusable and self-cleaning [5-6]. The fact that setal adhesion is not surface specific strongly suggests that this type of adhesion is controlled chiefly through geometry. Consequently, there is considerable interest in developing synthetic structures that mimic the unique properties of natural fibrillar adhesives and contact structures.

The simplest synthetic interface is a one level structure consisting of an array of micro-pillars or fibrils [7-13]. Typically, these structures do not exhibit good adhesion. This is partly due to the fact that such arrays have a much smaller total area of contact than do the flat surfaces [9]. In addition, fibrils in the array tend to be quite fragile. For example, they can buckle during preload, they can also adhere laterally to other pillars to minimize surface energy, or stick to adjoining structures [7, 9]. A quantitative theoretical understanding of these difficulties is now available and can be found in literature [14].

A two level structure that overcomes many of the above difficulties have been fabricated by Glassmaker *et al* [15]. This structure consists of an array of Polydimethlysiloxane (PDMS) fibrils which are roofed by a continuous terminal film,

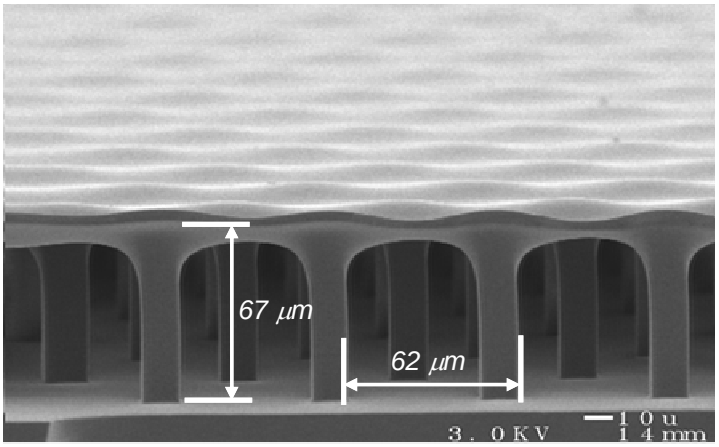

Figure 1.1 Scanning electron micrograph of a synthetic fibrillar array with a terminal thin film. Fibril height is about 67 μm and spacing is 62 μm. Each fibril is square in cross-section with sides nominally 14 μm wide. The terminal film is about 4 μm thick.

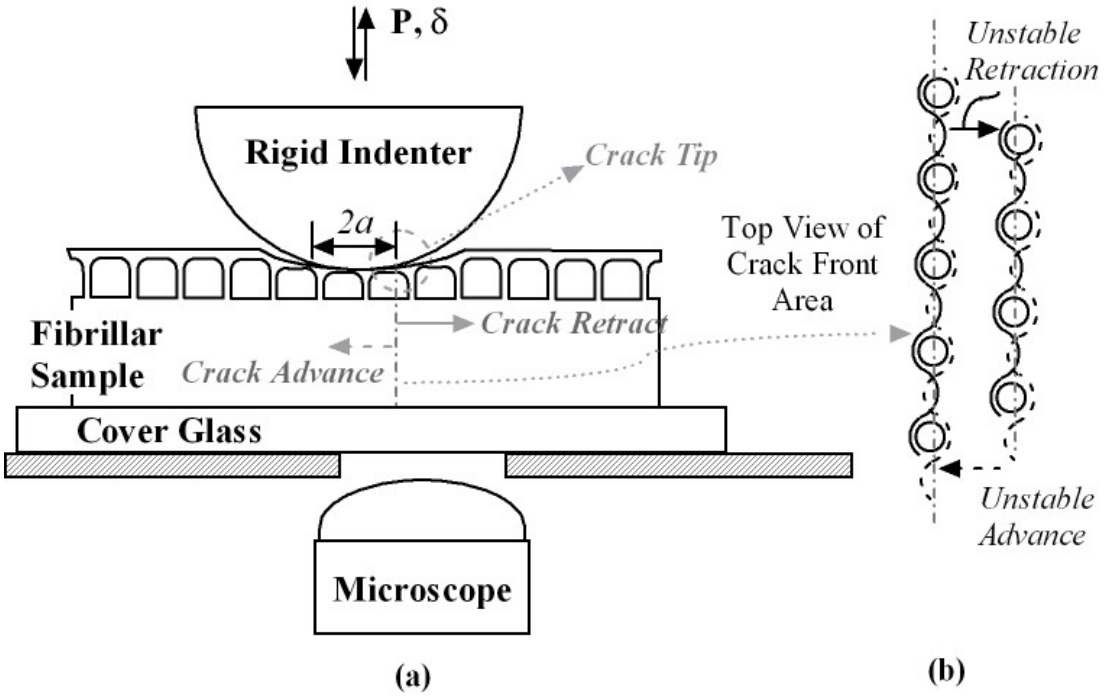

Figure 1.2 (a) Schematic diagram of the indentation test. Force is measured by an in-line load cell. The test is carried out in displacement control where the glass sphere is lowered and raised by a precision linear stage. (b) The crack front is trapped by fibril edges and 'bounce' through before them. At the same 'mean' location, its shape during crack advance is different than during retraction.

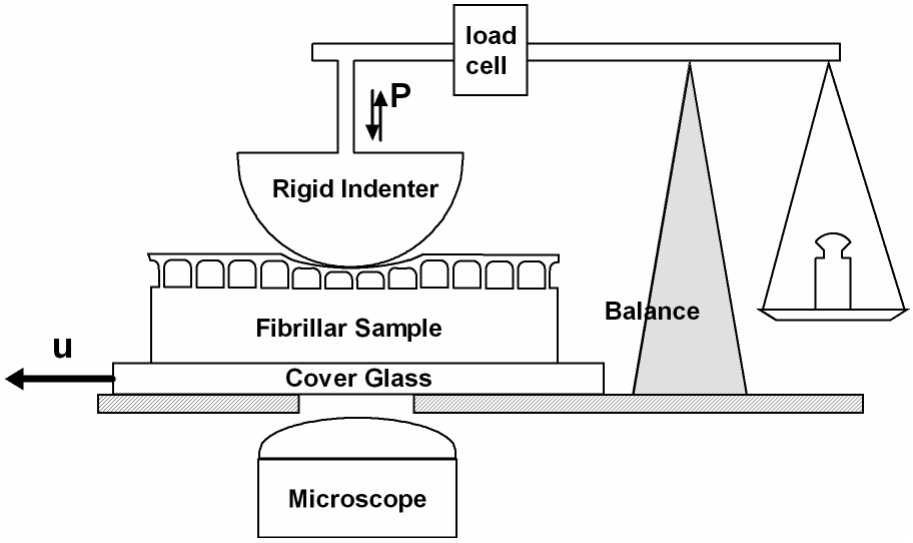

Figure 1.3 A glass indenter is placed on the fibrillar surface under fixed normal force (P) (applied via a mechanical balance). The sample is translated at a fixed velocity $\dot{u}$ and the shear force is measured by the load cell. Deformation near the contact region is recorded by means of an inverted optical microscope.

also made of PDMS (see Figure 1.1). Glassmaker *et al* [15] have shown that the effective work of adhesion this structure can be 5 times higher than flat unstructured samples of the same material.

In chapters 2 and 3, we present further studies on the normal adhesion of this structure. Normal adhesion is determined by conducting indentation tests via a custom apparatus shown schematically in Figure 1.2. Consistent with previous experiments, we found hysteresis in our film-terminated fibril array. However, cyclic loading at fixed contact area shows that bulk dissipation can be neglected. How then is energy dissipated in a purely elastic system? The key to understand this paradox is that during retraction, the interfacial crack front is trapped at the edge of fibrils (see Figure. 1.2).

This crack trapping mechanism creates an elastic instability which allows energy to be dissipated by vibration. A simple two dimensional model for crack trapping is proposed in chapter 2. The dependence of the crack trapping mechanism on the architecture of the fibrillar structure is studied in detail in chapter 3.

It has been observed by biologist that friction plays a significant role in the contact mechanics of small animals such as Gecko [16]. For example, the force that supports a Gecko on a vertical wall is mostly due to shear. In chapters 4 and 5, we carried out experiments to study the friction behavior of our film-terminated fibril array by dragging the sample across a glass indenter which is compressed by a fixed normal force. This apparatus is shown schematically in Figure 1.3. Using this apparatus, we study static and dynamic friction. We also determine the effect of displacement rate on them. We investigate the connection between normal adhesion and static friction. The use of optical microscope (see Figure 1.3) allows us to determine the deformation of fibrils in the contact zone and to determine the contact area. These results allow us to qualitatively understand the mechanics of dynamic and static friction.

REFERENCES

[1] M. Scherge and S. N. Gorb, *Biological Micro and Nanotribology: Nature's Solutions*, Springer-Verlag, Berlin 2001.

[2] E. Arzt, S. Gorb and R. Spolenak, *Proc. Natl. Acad. Sci.*, USA, 2003, **100**, 10603-10606.

[3] U. Hiller, *J. Bombay Natural Hist. Soc.* 1976, **73,** 278-282.

[4] K. Autumn, Y. A. Liang, S. T. Hsieh, W. Zesch, W. P. Chan, T. W. Kenny, R. Fearing and R. J. Full, *Nature*, 2000, **405**, 681-685.

[5] C. Creton, *Pressure Sensitive Adhesives: An Introductory Course*, MRS Bulletin 2003, June 1-6.

[6] W.R. Hansen and K. Autumn, *Proc. Natl. Acad. Sci.* USA 2005, **102**, 385-389.

[7] C.-Y. Hui, N.J. Glassmaker, T. Tang and A. Jagota, *J. R. Soc. Interface,* 2004*,* **1**, 35-48.

[8] E. Arzt, S. Gorb and R. Spolenak, *Proc. Natl. Acad. Sci. USA,* 2003*,* **100**, 10603-10606.

[9] N.J. Glassmaker, A. Jagota, C.-Y. Hui and J. Kim, *J. R. Soc. Interface*, 2004, **1,** 22-33.

[10] B. Yurdumakan, N. R. Raravikar, P. M. Ajayan and A. Dhinojwala, *Chem. Comm.*, 2005, **30**, 3799-3801.

[11] C. Majidi, R.E. Groff, Y. Maeno, B. Schubert, S. Baek, B. Bush, R. Maboudian, N. Gravish, M. Wilkinson, K. Autumn and R.S. Fearing, *Phys. Rev. Lett.*, 2006, **97**, 076103.

[12] M. Sitti and R.S. Fearing, *J. Adhes. Sci. Technol.,* 2003, **17,** 1055-1073.

[13] S. Kim and M. Sitti, *Appl. Phy. Lett.*, 2006, **89**, 26, 261911.

[14] Hui, C-Y.; Jagota, A.; Shen, L.; Rajan, A.; Glassmaker, N.; Tang, T., *J. Adhes. Sci. Technol.*, 2007, **21**, 12-13, 1259-1280.

[15] Glassmaker N J, Jagota A, Hui C-Y, Noderer W L and Chaudhury M K *Proc. Natl. Acad. Sci. USA* 2007, **104** 26 10786-10791.

[16] D.J. Irschick, C.C. Austin, K. Petren, R. Fisher, J.B. Losos and O. Ellers, *Biol. J. Linn. Soc*., 1996, **59,** 21-35.

CHAPTER 2

A STUDY ON ADHESION AND COMPLIANCE ENHANCEMENT OF FILM-TERMINATED FIBRILLAR SURFACES

2.1 Abstract

A bio-inspired film-terminated fibrillar surface has significantly enhanced adhesion and contact compliance compared to a flat control. Adhesion hysteresis, measured in cyclic indentation experiments, can be nearly five times the absolute work of adhesion for a flat control. A two-dimensional finite element model is used to show that adhesion hysteresis arises from the architecture of the interfacial region and develops due to crack trapping by fibril edges. Contact compliance of the fibrillar structure was measured up to seven times more than that of a flat control. A contact mechanics model is developed for the contact compliance of such structures which is in good agreement with measurements.

2.2 Introduction

Fibrillar surfaces are commonly found on the contact surfaces of the feet of many lizards and insects (see, e.g. Scherge & Gorb (2001), Rizzo *et al*. (2006), Autumn *et al*. (2000), Eisner & Aneshansley (2000), Ruibal & Ernst (1965), Hiller (1968,1976)). Since these creatures rely on clinging and climbing abilities for survival, a plausible supposition is that they have evolved fibrillar surface architectures in a way that enhances their chance of survival (Scherge & Gorb 2001). Drawing this hypothesis a bit further, one deduces that fibrillated surfaces must provide desirable adhesion and friction properties. In particular, past studies have shown that fibrillar surfaces are more compliant than flat surfaces of the same material, which allows

better adhesion against rough surfaces (Persson (2003), Persson & Gorb (2003), Hui *et al*. (2005)). Moreover, due to the small size and compliant nature of the contacting tips or 'spatulas' of biological setae, fibrillar surfaces are able to attain stronger adhesion than flat surfaces of the same material (Autumn *et al*. 2000, Arzt *et al*. 2003).

With such biological systems as motivation, several groups have recently attempted to mimic the biological architecture in order to attain enhanced adhesion (Glassmaker *et al*. (2004), Hui *et al*. (2004), Yurdumakan *et al*. (2005), Majidi *et al*. (2006), Peressadko & Gorb (2004), Sitti & Fearing (2003), Kim & Sitti (2006), Gorb *et al*. (2006)). Simple, single-level, structures generally fail to achieve theoretically predicted enhancement in strength and toughness due to loss of contact area, lateral collapse and buckling of fibrils (Glassmaker *et al*. (2004), Hui *et al*. (2004)). Fibrillar structures with 'mushroom' ends have been shown to enhanced adhesion significantly (Kim & Sitti (2006), Gorb *et al*. (2006)). (See Jagota *et al*. (2007) and other articles from the same issue for reviews on this subject.)

A two-level structure that consists of a simple array of micro-posts connected at the terminal end by a thin, flexible film has recently been shown to significantly improve adhesion compared to a flat unstructured control (Figure 1.1) (Glassmaker *et al*. (2006), Glassmaker *et al*. (2007)). While inspired by biological setal adhesion, this architecture is distinct from any that we are aware of in nature, although the geometry of the setal system found in the insect *Tettigonia viridissima* is quite similar (Gorb & Scherge 2000). Our design contains only one degree of sophistication over the preceding simple micro-pillar arrays, i.e., a thin film at the terminal, contacting end of the fibrils. As we show in this paper, adhesion enhancement is due to the spatial variation of energy available to drive a crack (for monotonically changing remote load) as it moves from fibril to fibril. With this undulation in available energy, the crack is

forced to propagate unstably, and requiring a larger load than would be necessary when the fibrillar region is not present.

In addition to enhancing adhesion, the structure shown in Figure 1.1 is advantageous for several other reasons as well. Specifically, by its design, it avoids two undesirable phenomena observed for large aspect ratio, free standing posts: lateral collapse and buckling (Glassmaker *et al*. 2004, Hui *et al*. 2002, Sharp *et al*. 2004). These phenomena both reduce contact area and adhesion. Another advantage of the structure in Figure 1.1 is the fibrillar geometry and terminal film provide increased compliance precisely where it is needed, i.e. at the contact interface. This allows the surface to achieve initial contact more easily and, as just mentioned, it also results in crack tip pinning, which helps to maintain contact.

The plan of this chapter is as follows: a detailed summary of the experimental methods is given in section 2.3. Some of the experimental results that are relevant to our theoretical modeling are also presented in this section. These experiment work were jointly carried out by Norderer, W. and Vajpayee, S. and were reported in Norderer *et al* (2007).

2.3.1 Sample Fabrication

The fabrication method for the structure shown in Figure 1.1 has been discussed in Glassmaker *et al.* (2006) and (2007). Briefly, a fibrillar array is created by moulding a polymer precursor (in this case, poly(dimethylsiloxane) (PDMS)) using a negative topographic master. The master consists of an array of square holes in Si, created by photolithography and a deep reactive ion etching process. Then, the liquid polymer precursor is poured into the holes, cured and subsequently peeled out of the master. An array of polymer posts results. The cross-sectional geometry and spacing

of the posts is identical to that of the array of holes on the master, and the post height is equal to the depth of the hole.

To attach the terminal film to the ends of the posts, a polymer precursor (again PDMS, here) is first spin-coated on a hydrophobic substrate. Then, the array of posts is placed on the film while the film is still liquid. The liquid film partially wicks up the fibrils and is cured in place. The entire sample is removed from the substrate manually after a glass cover-slip is attached as a cantilever to the backing of the sample. All samples have the same terminal film thickness. Our analysis predicts that thinner films would increase adhesion. However, thinner films more readily tear and are therefore more difficult to manufacture. A typical final fibrillar structure is shown in Figure 1.1. We usually fabricate three fibrillar samples with different structures on a single 10 cm Si wafer. On each wafer, we also fabricate a flat control. The thin film is adhered onto the flat control in the same fashion as to the fibrillar sample.

Nine fibrillar samples are discussed in this paper. All of the samples have a nominal film thickness of 4 μm and have fibrils with a square cross-section of 14 μm per side arranged in a hexagonal pattern on a 650 μm thick backing. The fibril height and fibril spacing were varied to analyse the effects of geometry. Each sample had a fibril height of 53, 60 or 67 μm and a fibrillar spacing of 38, 62 or 87 μm. For purposes of clarity and brevity, samples are referred to simply by their fibrillar spacing and fibrillar height. For example, a sample with a fibrillar spacing of 87 μm and a fibrillar height of 60 μm is referred to as 'S87H60'.

2.3.2 Review of experimental results via indentation test

The indentation experiments were carried out in a custom apparatus built on an inverted optical microscope as shown schematically in Figure 2.1. This set-up and experiment procedure was designed by our research group and described in detail in

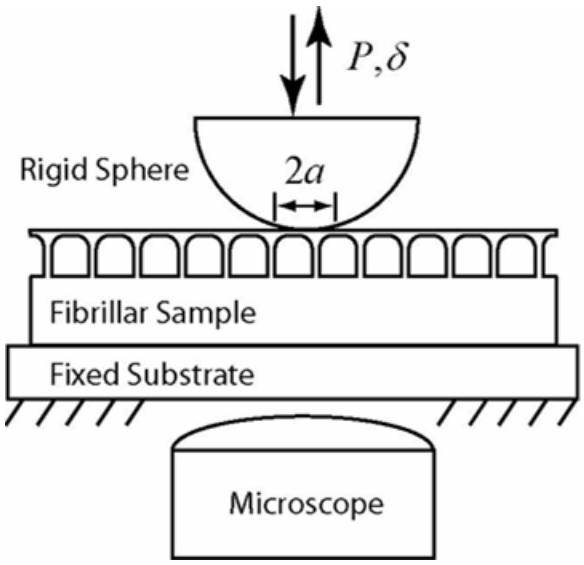

Figure 2.1 Schematic of the experimental indentation apparatus. The sphere was lowered and raised by a precision linear stage in displacement control, and an in-line load cell measured the force on the sphere

Noderer *et al* (2007). It consists of a precision vertical stage attached to a rigid load train containing a strain gage type load cell in line with a spherical glass indenter with a 4mm radius. The surface of the glass indenter was treated with an organo-silane monolayer in order to minimize hysteresis and time-dependent effects in the control samples[1]. The stage lowered the indenter into contact with the sample of interest, which was supported on the microscope platform. As this happened the load cell voltage and stage displacement were recorded by a computer data acquisition system, and the contact area between the indenter and sample was viewed through the microscope. The computer used for data acquisition also recorded a direct digital streaming video of the contact evolution.

Typical experimental force and displacement data from a fibrillar surface (S87H60) and a flat control surface are shown in Figure 2.2. In either case, the specimen was indented to a depth of 30 μm in the first cycle; the indenter was retracted to different depths, then cycled to the maximum depth 10 times and finally retracted completely out of contact. Note the markedly different behavior of a fibrillar surface and flat control surface. First, the fibrillar surface is much more compliant than the flat surface; the latter requires much greater force for the same indenter depth. Second, the fibrillar surface requires a greater tensile force to separate the indenter from the sample. Third, the fibrillar surface requires a greater amount of work to separate the indenter from the sample. Fourth, the fibrillar sample shows greater hysteresis in an indentation cycle. Contact micrographs are shown in Figure 2.2 for when the indenter is at a depth of 0 μm (a,e), 15 μm (b,d), and 30 μm (c) for both

[1] Our purpose in treating the indenter with a hydrophobic self-assembled monolayer is to establish a control with minimal hysteresis and adhesion dominated by van der Waals forces. Absent such a treatment, it is well-known that rate-dependent and hysteretic interfacial processes occur that (Ghatak et al. 2000), in our experiments, would cloud the effects of specimen geometry on hysteresis that we wish to establish. Hexadecyltrichlorosilane was evaporated for 1 hour onto the glass after precleaning it with 70% H_2SO_4, 30% H_20_2 for 30 min., and then low energy oxygen plasma for 1 minute.

indentation and retraction. The fibrillar surface has a greater contact area at all indentation depths. As will be clearer following our discussion of contact compliance, this is because compliance of the fibrillar material is in large measure due to the deformation of the thin surface layer (fibril + film). This fact changes the kinematic relationship between indenter depth and contact area (Johnson (1985)). Figure 2.2 shows that the evolution of contact of the flat control surface is approximately symmetric about maximum indentation; note the similarity between pairs (a,e) and (b,d). This is not the case for the fibrillar samples; note the difference between micrographs (a,e) and (b,d). In fact, the contact area on the fibrillar surface remains pinned when the indenter retracts from 30 μm to 15μm. Crack pinning is of central importance in our explanation of the energy dissipation process. It also turns out to be useful in determining sample contact compliance and work of adhesion. Particular attention should be directed towards the shape of the contact areas. As expected, the spherical indenter produces circular contact areas on the flat control surface. However, the same spherical indenter produces irregular contact areas which approach a hexagonal shape, especially when the contact area is small.

The behavior of the control corresponds to adhesive indentation, fitting the Johnson-Kendall-Roberts (JKR, 1970) model, which implies that

$$\frac{P}{a^{3/2}} = \frac{4E^* a^{3/2}}{3R} + \sqrt{16\pi\gamma E^*} \tag{2.1}$$

where P is the load, a is the radius of contact, R is the radius of the indenter, E^* is the plane strain elastic modulus, and γ is the surface energy. Plotting the left hand side of equation (2.1) as a function of $a^{3/2}$, a JKR plot as shown in Figure 2.3, was used to estimate the surface energy and elastic modulus of the flat controls in this experiment. The flat control samples fabricated from PDMS had an average work of adhesion (on contact growth) and plane strain modulus with a 95% confidence interval of

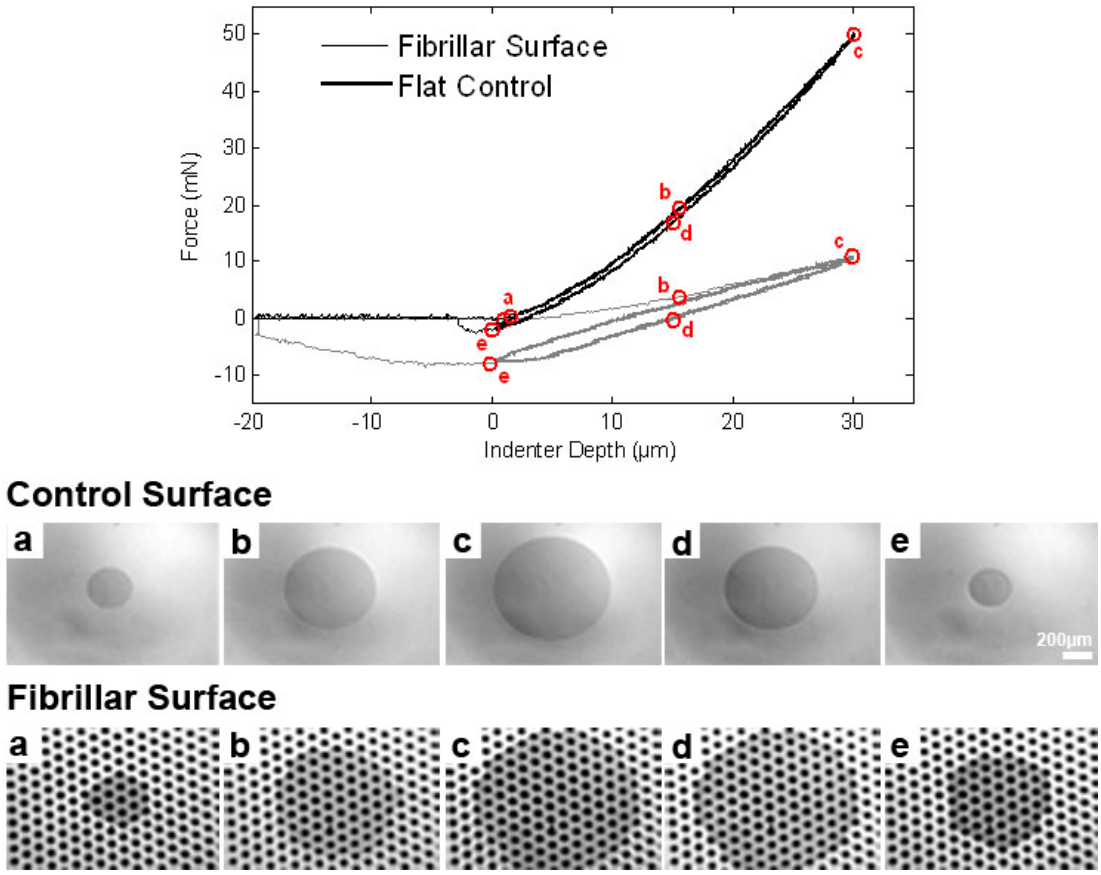

Figure 2.2 Typical force vs. indenter depth of a fibrillar surface (S87H60) and a flat surface. The micrographs show the contact area corresponding to various points on the graph.

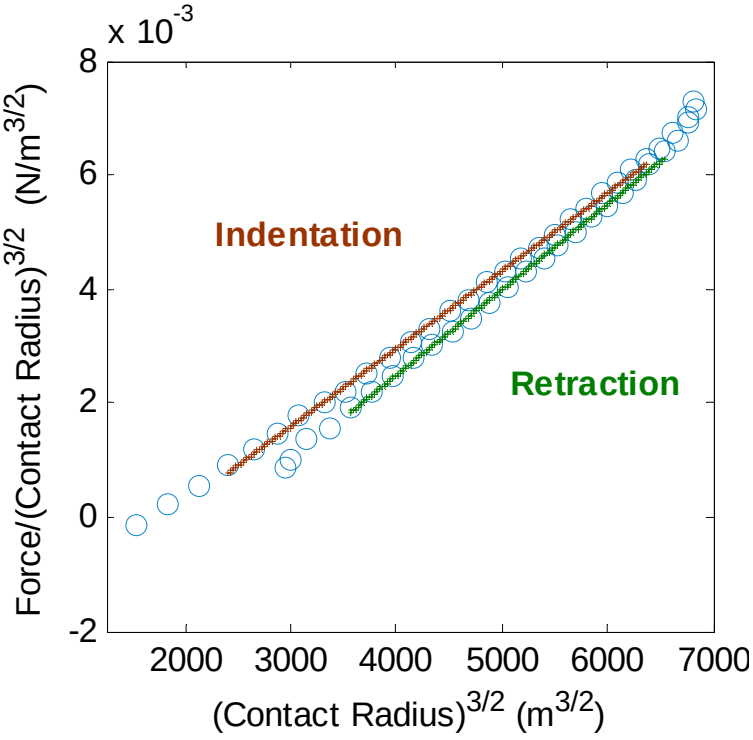

Figure 2.3 Typical JKR plot of a flat control surface.

0.0692 ±0.002 J/m^2 and $3.81 \cdot 10^6 \pm 4 \cdot 10^4$ N/m^2 respectively.

The JKR model, equation (2.1), cannot be applied to the fibrillar surfaces because the samples are neither isotropic nor homogenous. Therefore, two separate experiments were devised to extract adhesion hysteresis, the work of adhesion and compliance of the fibrillar surfaces.

The goal of the first set of experiments is to measure the sample compliance. It utilizes the fact that the contact area is pinned when the indenter begins to retract from the surface as seen in Figure 2.2 (points c and d). For a given fixed contact area, the compliance is the change in indenter displacement δ per unit force, $d\delta/dP$. A suitable normalization for the fibrillar compliance is by the flat punch (Boussinesq) value for a half space at the same contact area (Johnson (1985)), i.e.,

$$C_B = \frac{1}{2aE^*} \tag{2.2}$$

where $a = \sqrt{A/\pi}$ is the contact radius, and A is the measured contact area

The compliance experiments were carried out by starting the indenter away from the sample. The indenter was lowered at a displacement rate of 1μm/s to a specified depth and then completely retracted from the sample. The process was repeated for a series of depths and a linear fit was used to find the slope of the force versus displacement curve immediately after the indenter reached its specified depth, as shown in Figure 2.4. For the parts of the curves used to find compliance, the contact line was observed to be pinned between two rows of fibrils and the contact area was nearly fixed.

The interfacial hysteresis experiment is similar to the compliance experiment except that the glass sphere was indented to a depth of 30 μm and then retracted to a specified depth. The indenter was then cycled 10 times between the maximum and minimum indentation depth. Results presented in Norderer *et al* (2007) via repeating

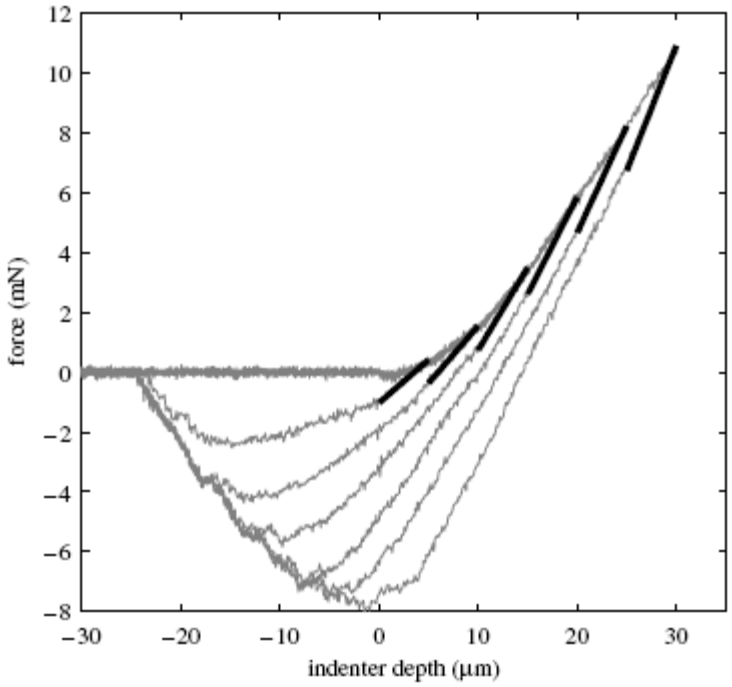

Figure 2.4 Typical plot of indenter depth versus force (S87H60). The contact area is pinned for a period of time after the indenter begins to retract. A linear line (red) is fit to the portion of data with constant area to extract the compliance of the fibrillar surface.

a series of varying minimum indentation depths is shown in Figure 2.5. The net area under the force-displacement curve during a cycle was measured along with the contact area at the maximum and minimum indentation depths. Interfacial hysteresis was then calculated by

$$\Delta W \equiv \left(\oint P\, d\delta\right) / \Delta A \tag{2.3}$$

where ΔA is the difference between maximum and minimum contact area in a loading cycle. The interfacial hysteresis was normalized by the work of adhesion of the flat control surface, $W_{ad}=2\gamma$ (equation (2.1)). This process was repeated for several (six to twelve) minimum indentation depths. Figure 2.5 shows an example with three different minimum depths. There is little hysteresis for smallest cycle (blue curves); it is observed that over this range of retraction the contact remains pinned. By contrast, once the contact area changes significantly over the course of a cycle (green and red curves), the adhesion hysteresis also increases significantly. This clearly indicates that hysteresis arises not from the bulk material properties but is due to the process of separation. Since the hysteresis is large compared to that measured in a flat control, we conclude that hysteresis arises due to the fibrillar structure.

The analyses of energy loss during cyclic indentation and compliance during unloading are attractive because they allow extraction of these properties of the interface in a model-independent manner. Unfortunately, this does not extend to the extraction of absolute work of separating the interface. However, for the samples where hysteresis dominates, we show how it is possible to estimate this value with one reasonable assumption.

Consider Figure 2.6 below in which the blue line represents a typical force-displacement measurement for a fibrillar sample. Suppose one is at a point A in the unloading cycle at which the displacement is δ and the contact area is known as well. To calculate the work of separating the interface one attempts to compute the

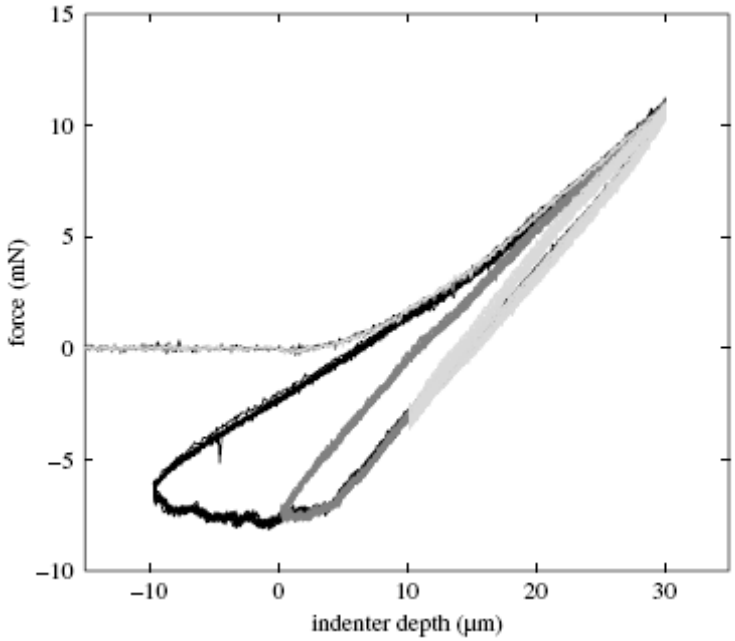

Figure 2.5 Typical plot of indenter depth versus force for a fibrillar surface (S87H60).

difference between stored strain energy in the fibrillar sample and external work done on it in reaching this point. Since the bulk sample is elastic, the strain energy depends only on the geometry of the final state. To calculate the strain energy stored in the sample at that point, one may follow a specific path (Shull 2002). First, it is assumed that the adhesive forces are turned off as in an adhesion-less 'Hertz' contact and indent the sample till one reaches a point, B, which has the same contact radius as A. Now assume the indentation depth is δ_H. The strain energy of the system at the end of this step is given by the area under the load-displacement curve till that point (δ_H).

$$U_{E1} = \int_0^{\delta_H} P\, d\delta \tag{2.4}$$

Then fix the contact area and retract the indenter until a displacement of δ. Because the contact is fixed in the second step, *and* the contact compliance is known, it is simple to compute the change in strain energy in the second step.

$$U_{E2} = \int_{\delta_H}^{\delta} P\, d\delta \tag{2.5}$$

The total strain energy is

$$U_E = U_{E1} + U_{E2} = \int_0^{\delta_H} P d\delta + \int_{\delta_H}^{\delta} P d\delta \tag{2.6}$$

The problem in computing U_E is that, without using a model, one does not know the Hertz curve for our material. However, for samples dominated by hysteresis, the adhesion during the loading phase can be neglected in comparison with its value during unloading so that the loading part of the force-displacement curve is taken as the Hertz curve. Then, the total strain energy at point A is shown in Figure 2.6 by the area shaded in light grey. The net external work done on the system is simply the area under the force-indentation curve; the difference between the two, a strain energy *deficit*, is shaded dark grey in Figure 2.6. This deficit we identify as the work required to separate the interface.

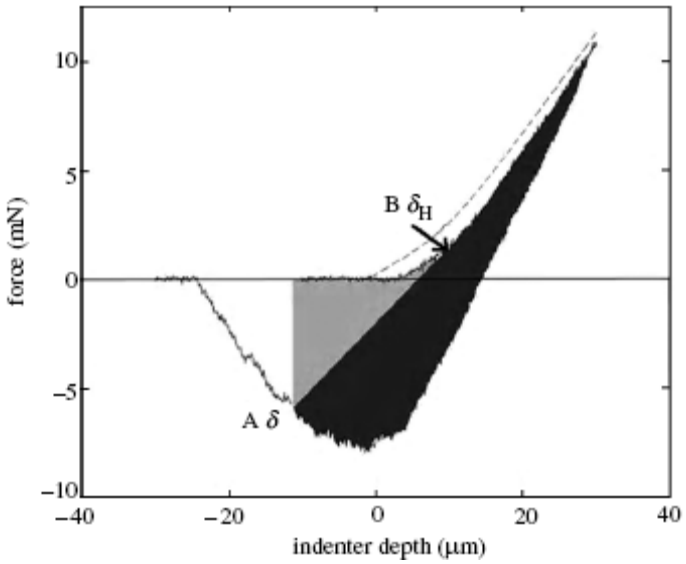

Figure 2.6 Typical load-displacement plot showing, for point A, strain energy (light gray area) and difference between external work done and strain energy (dark grey area) and the Hertz curve (dashed line).

To implement this strategy, a series of points are picked corresponding to 'B' in Figure 2.6 where the compliance is already known as described earlier. Using the known value of compliance, a straight line is extended from point 'B' until it intersects the experimental force-displacement curve on unloading (Figure 2.7, points 'A').

These intersections now represents points where one knows how to calculate strain energy and external work, and hence the deficit in energy. A typical plot of the deficit versus the area is shown in Figure 2.8; its slope is the estimate of absolute work of separation during unloading. As expected, this method works well and produces values consistent with the hysteresis experiment in cases where the latter dominates. An effective work of adhesion during loading was also extracted from the same experiments by making a JKR plot as in Figure 2.3.

The result in Figure 2.8 supports the following models of interfacial hysteresis. In the control samples there is little bulk dissipation, so the change in strain energy in a cycle is small. This means that the measured hysteresis energy approximately equals the work done on the interface over a cycle. If we assume that the work done in separating the interface takes a single constant value on opening, W^+, and a *different* but also a constant value on healing, W^-, we have

$$\oint P d\delta = \oint W dA = (W^+ - W^-)\Delta A \tag{2.7}$$

Equation (2.7) implies that the hysteresis per unit area vanishes if the work of opening the interface equals the work released on its closing. If the works on opening and closing are different, hysteresis is directly proportional to ΔA. The fact that W^+ is a constant is supported by the data in Figure 2.8; the slope of the line is $-W^+$. Note that, if $W^+ >> W^-$, then the hysteresis per unit area is well approximated by the work of separating the interface. As to be discussed in section 2.4, the model developed for this study shows consistency with this assumption.

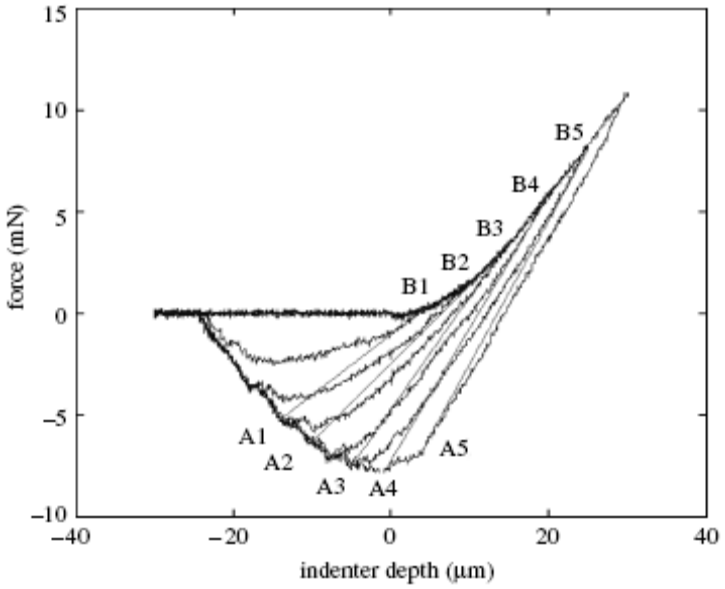

Figure 2.7 Raw force-deflection data with straight lines joining points where compliance is known with their corresponding point *A* on unloading. (Sample S87H60.)

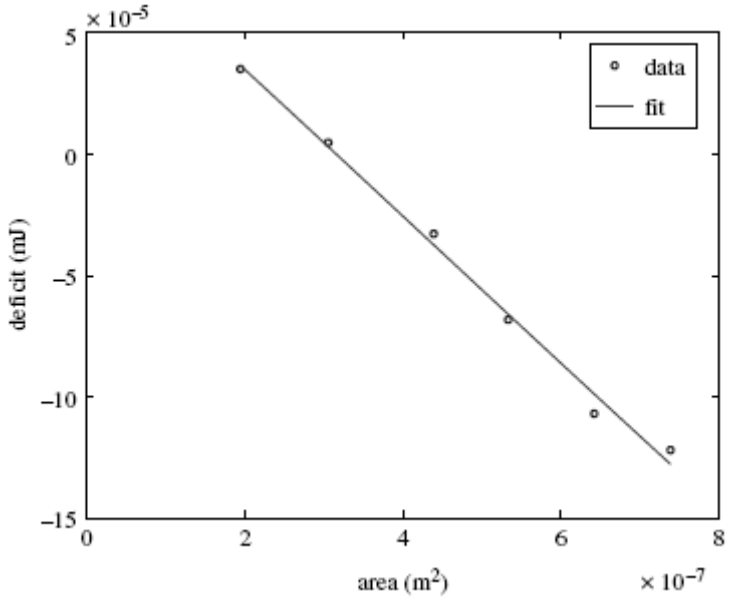

Figure 2.8 A typical plot of work deficit versus contact area for different points on the unloading curve; its slope is the work of adhesion.

2.3.3 Effect of Geometry

Figure 2.9 shows measured adhesion hysteresis (see equation (2.3)) normalized by the work of adhesion of the flat control for samples with 53 μm long fibrils and three different fibril spacing namely $\Delta W/W_{ad}$. Beyond a certain contact area, the normalized hysteresis approaches an asymptotic value, consistent with the picture of a well-defined work of adhesion for opening and another one for closing of the crack. Note that the hysteresis is greatest for the intermediate spacing of 62 μm. Figure 2.10 shows the aggregated data for normalized interfacial hysteresis for all nine samples. Note that some fibrillar samples have a value nearly five times the work of adhesion of a flat control. Interestingly, it appears that maximum hysteresis is achieved for intermediate spacing and fibril height. In section 2.4 we developed a model to interpret this observation. The maximum pull-off force for all nine samples, normalized by its measured value for the flat control is shown in Figure 2.11. It presents a picture consistent with that painted by the hysteresis data.

2.4 Theory

2.4.1 Crack trapping mechanism

To understand the origin of hysteresis in our experiments we have analyzed a two-dimensional plane stress model where the fibrillar structure consists of a single row of pillars as shown as Figure 2.12. Fibrils have width *b* and are spaced with a period *w.* The terminal film has thickness *t.* The material in infinite in extent in the 'x' direction and the interfacial crack between the strip and the substrate is assumed to be semi-infinite. A uniform vertical displacement δ is applied on the upper surface of the strip. We wish to analyze how the energy release rate available to propagate the interfacial crack, *G,* varies with spatial position of its tip. This problem has translational symmetry in the sense that relative to the crack tip all fields repeat with period equal

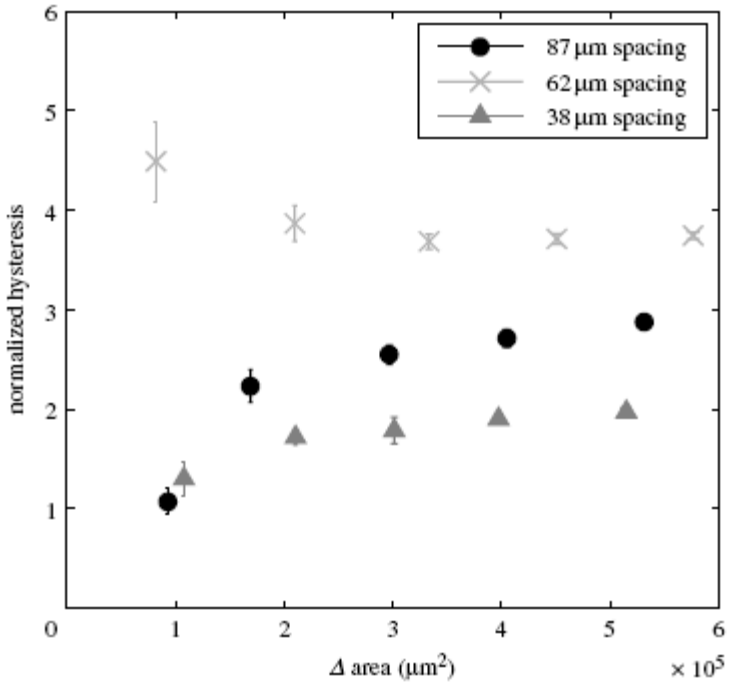

Figure 2.9 Normalized interfacial hysteresis for samples with 67 μm long fibrils as a function of change in contact area.

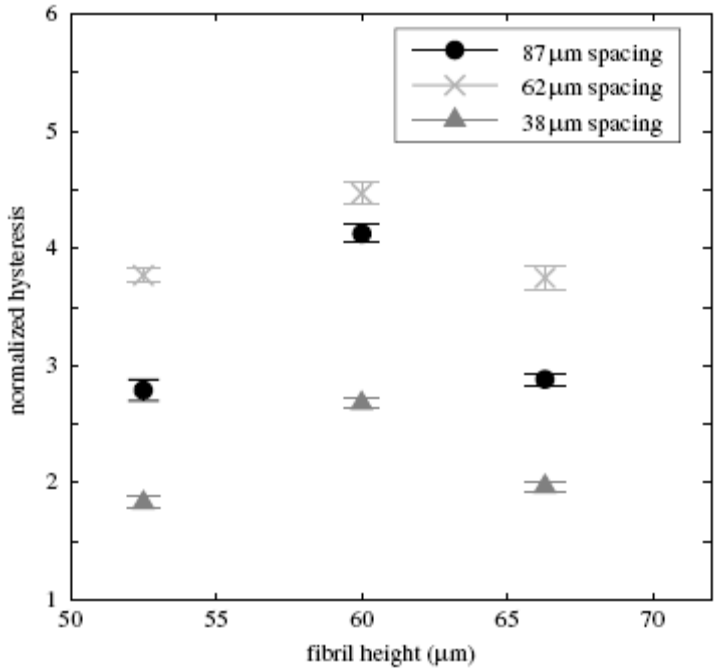

Figure 2.10 The fibril height versus normalized interfacial hysteresis at the maximum change in contact area.

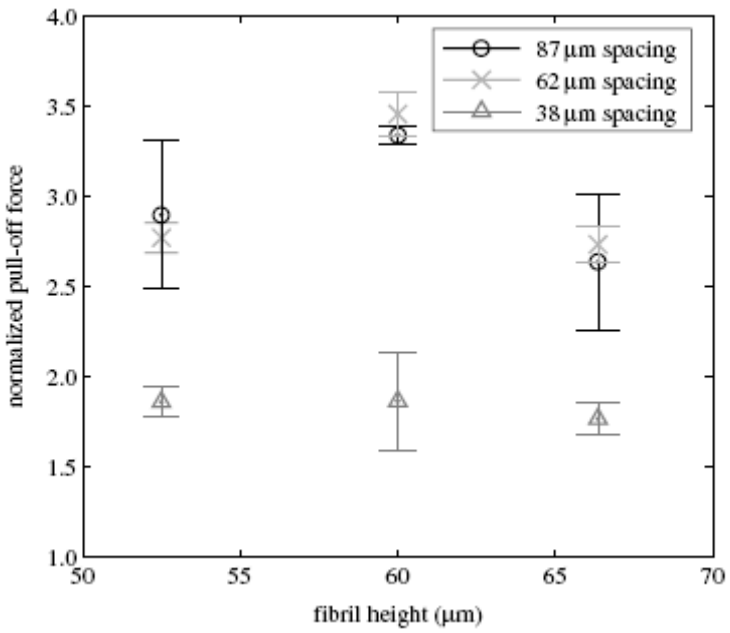

Figure 2.11 Maximum force needed to completely pull off the indenter from the fibrillar surface normalized by the maximum pull off force of the flat control surface.

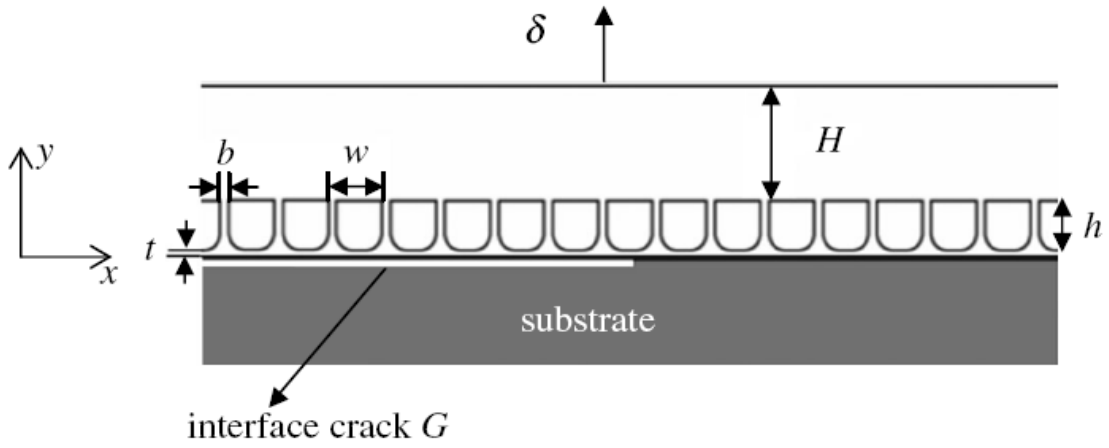

Figure 2.12 Geometry of strip with a semi-infinite crack on the film/substrate interface.

to spacing w. We thus need only to consider a unit cell starting at an arbitrary location c with x in the range $c<x<c+w$.

Dimensional analysis and linearity imply that the local energy release rate G can be written as

$$G = (2E\delta^2 / 3H)\phi(x/b, w/b, h/b, H/b, \nu) \tag{2.8}$$

where ϕ is a dimensionless function of crack tip position, geometry and Poisson's ratio, ν. We compute G as a function of crack-tip position in the periodic cell using a finite element method (details will be reported elsewhere). Its typical variation with crack position within the unit cell is shown in Figure 2.13 (w/b = 13/3, h/b= 20/3, t/b=2/3). The vertical dotted lines represent pillar edges. We have normalized G by

$$G_o = 2E\delta^2 / 3H\ , \tag{2.9}$$

which is the energy release rate of a flat control. The horizontal lines in Figure 2.10 represent the normalized work of adhesion of the interface, W_{ad}/G_0. Since G_0 increases with δ, this horizontal line shifts downwards monotonically with increasing applied displacement.

When the crack is between fibrils, the energy available for crack growth comes primarily from the thin film. Thus, the energy release rate is expected to be low and a decreasing function of crack length until the crack reaches the next fibril whereupon it starts to increase. This behavior is apparent in Figure 2.13; indeed the minimum in ϕ occurs just to the left of a fibril and the maximum at its right edge. Consider a situation in which the crack tip is initially located at some position to the left of the fibril as shown in Figure2.14. We study the growth of this crack as the remote applied displacement is increased. The condition for stable crack growth is

$$G = W_{ad}\,,\ \frac{dG}{dx} < 0. \tag{2.10}$$

i.e., to keep the crack in stable equilibrium the energy release rate at the crack tip must equal the work of adhesion and it should be a decreasing function of crack tip location.

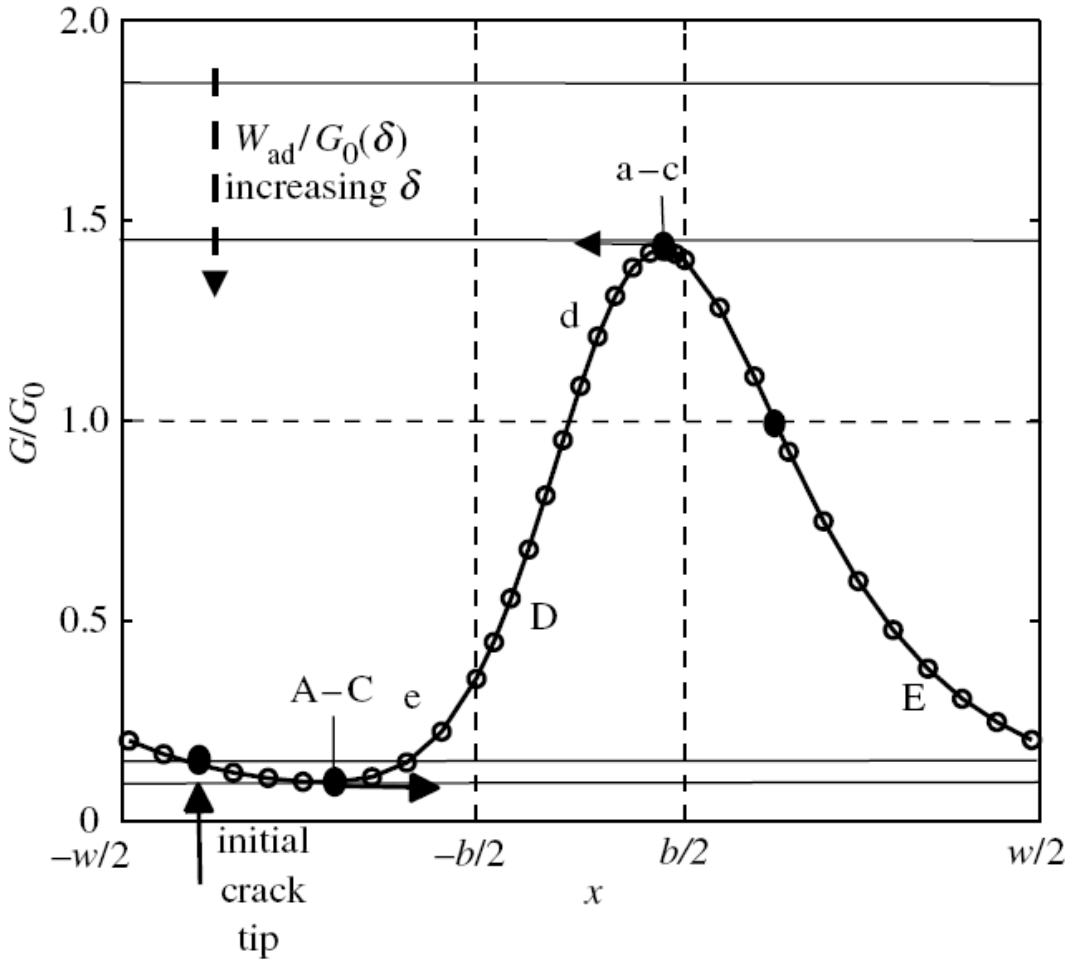

Figure 2.13 Variation of normalized energy release rate G/G_0 with respect to position of crack tip x. The lower-case and capital letters correspond to letters in Figure 2.11. Points A-C and a-c represent locations where the crack is trapped during opening and healing, respectively.

Equation (2.8) implies that with increasing applied displacement the G/G_o curve, the connected points, does not change while the normalized work of adhesion line moves downwards in Figure 2.13. It represents the dimensionless function, ϕ. The crack will remain at its initial position until the applied displacement increases sufficiently so that the intersection of the horizontal line and the function ϕ occurs at the crack tip location. With further increase in applied displacement, the crack tip moves stably to the right until it reaches the point where ϕ is minimum, in which circumstance the applied displacement is δ_{max}. Any slight increase in applied displacement will result in unstable crack growth since $dG/dx>0$ after the minimum. Thus, the crack will propagate at an applied displacement of δ_{max}. In contrast, for a flat control, crack propagation occurs when the normalized work of adhesion equals unity, $3HW_{ad} / 2E\delta_{flat}^2 = 1$. Since

$$\delta_{\max}^2 = 3HW_{ad} / 2E\phi_{\min} \tag{2.11}$$

the ratio of applied displacement needed to propagate the crack in a fibrillar sample versus a flat control is

$$\frac{\delta_{\max}^2}{\delta_{flat}^2} = 1/\phi_{\min} \tag{2.12}$$

An external observer unaware of the microstructure will find that it takes greater applied displacement to separate the interface. Since the fibril height is small compared to the layer thickness, $h<<H$, and the material modulus is the same, this observer will conclude by applying equation (2.9) that the effective work of adhesion of the interface has increased by a factor of $1/\phi_{\min}$. Moreover, the arrested crack would always be found at the position where ϕ is a minimum, x_{min}, *i.e.*, just to the left of a fibril.

Now, with the crack tip at x_{min}, consider what happens as the loading is reversed. As applied displacement is decreased, the crack will close stably until the

crack tip reaches the position, x_{max}, where ϕ achieves its maximum $\phi_{\max}$, and $\delta=\delta_{min}$. Any slight decrease in applied displacement results in unstable crack closure. The equivalent statement to equation (2.12) now becomes

$$\frac{\delta_{\min}^2}{\delta_{flat}^2} = 1/\phi_{\max} \tag{2.13}$$

and the external observer will conclude that the effective work of adhesion during crack closure is $1/\phi_{\max}$. The works of adhesion for crack opening and healing, W^+, W^-, respectively, introduced above can now be related to $\phi_{\min}$ and $\phi_{\max}$ as

$$\begin{aligned} W^+ &= W_{ad}/\phi_{\min} \\ W^- &= W_{ad}/\phi_{\max} \end{aligned} \tag{2.14}$$

During crack opening, our argument implies that the external loading apparatus will have to release energy at a rate in excess of that required by the interface itself. Where is this extra energy expended, one might ask, in a purely elastic system? In particular, if the crack had traversed the entire periodic cell stably, we must insist that the mean energy release rate should have equaled the intrinsic work of adhesion. This has been confirmed by our numerical simulations. During part of its traversal, some of the remotely supplied energy is stored by the fibrils. During the remaining part, this stored energy would be released. As we have shown, for realistic loading (i.e., monotonically increasing remotely), the part of the cycle where the energy is stored corresponds to stable crack growth. However, the part where the stored energy is released is unstable and the energy is not recoverable.

Figure 2.14 shows a sequence of images in which the crack closes (indentation) and then opens (retraction of indenter) over the same set of fibrils. These images are separated by equal time intervals of 1 second. Dark regions represent the contact; light regions are the crack. The arrow on the first indentation panel (a) points out that on closure, the crack is trapped on the right hand side of the fibril consistent with our model. Indentation panels (d,e) shows the unstable crack jumping across the

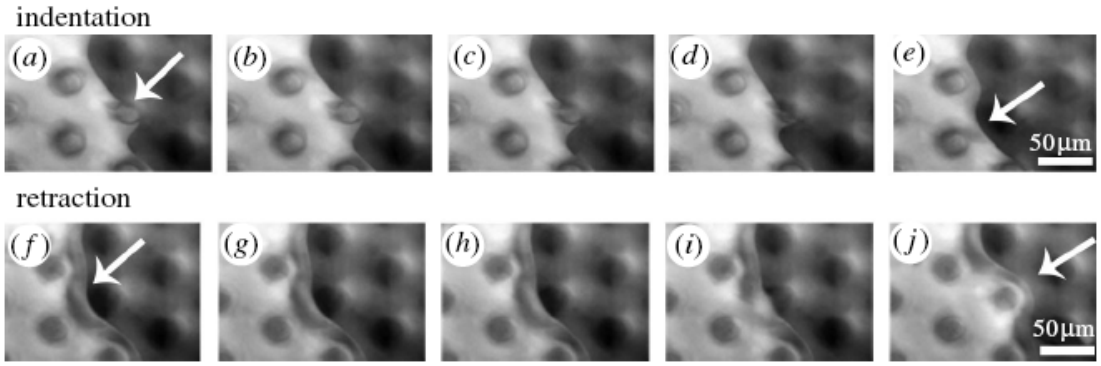

Figure 2.14 Micrographs of the crack trapping mechanism on a fibrillar surface (S60H67) for both indentation and retraction

trapping fibril. The first Retraction panel (A) shows trapping of the crack front by the left edge of the fibril. In panels (D,E), the crack jumps across this fibril. It is apparent that the crack trapping geometry in the experiments is three-dimensional and not all observations can be captured by our two-dimensional model. For example, our 2D model would predict that the crack location relative to the trapping fibril is the same before and after the jump. In the experiments the crack front is wavy and its location is evidently determined both by the next trapping fibril and by the position of the rest of the front.

2.4.2 Contact Compliance

In this section a contact mechanics model is developed to study the compliance of the fibrillar array. We assume that the contact compliance is dominated by the behavior of the fibrils themselves and of their connection with the backing material. That is, the role of the terminal thin film on the compliance of the fibrillar structure is assumed to be negligible. Prior to buckling, the fibrils are assumed to deform as bars so bending and buckling effects are ignored.

We assume that fibrils are identical, have circular cross-sections, and are arranged in a hexagonal array. The radius and height of the fibrils are denoted by a_f and L, respectively. Given the radius of contact R, the number of fibrils in contact, N, can be obtained by simple geometry,

$$N = 3m(m+1)+1 \approx 3m^2 \quad m>>1 \tag{2.15}$$

where $m \equiv \text{int}\left(\frac{R-a_f}{w}\right)$, w is the spacing between center lines of the nearest fibrils.

The displacement of the k^{th} fibrils $k=1,2...N$, relatively to the substrate, denoted by u_k^f is

$$u_k^f = \frac{F_k L}{E\pi a_f^2} \tag{2.16}$$

where F_k is the force acting on the k^{th} fibril and E is the modulus of the fibril.

Let the average vertical displacement of the area directly underneath the k^{th} fibril be denoted by u_k^s. This displacement can be estimated by assuming that the pressure is uniform in the circular region common to the k^{th} fibril and the substrate. Another possible approach is to assume uniform displacement in the circular region. These two methods give nearly the same prediction; we will present only the former. According to Johnson (1985), the vertical displacement due to a uniform pressure $F/\pi a_f^2$ applied on a circular region with center at the origin is:

$$u^s = \frac{4F}{\pi^2 E^* a_f}\mathbf{E}(\hat{\mathrm{r}}), \quad \hat{r} \equiv \frac{|\mathbf{r}|}{a_f} \le 1 \tag{2.17}$$

$$u^s = \frac{4F\hat{r}}{\pi^2 E^* a_f}\left[\mathbf{E}\left(\frac{1}{\hat{r}^2}\right) - \left(1-\frac{1}{\hat{r}^2}\right)\mathbf{K}\left(\frac{1}{\hat{r}^2}\right)\right], \quad \hat{r} > 1 \tag{2.18}$$

where ***r*** is a vector from the center of the fibril to any point on the interface. The functions $\mathbf{K}\left(\frac{1}{\hat{r}^2}\right)$ and $\mathbf{E}\left(\frac{1}{\hat{r}^2}\right)$ are the complete elliptic integrals of the first and second kind with character $\frac{1}{\hat{r}^2}$, respectively. Using (2.17) one can calculate the average displacement of the region underneath the fibril, i.e., $\hat{r} \le 1$ to be

$$u^s = \frac{224F}{45\pi^2 E^* a_f}, \tag{2.19}$$

Here we have assumed that the fibril layer is thin in comparison with the backing (PDMS) layer thickness ($\approx 650\mu m$), since the solution above assumes that the substrate is a half space. Because the material is linearly elastic, the displacement at any point is given by superposition of that due to the force applied at that very point and that due to forces at all other points:

$$u_k^s = \frac{224F_k}{45\pi^2 E^* a_f} + \sum_{i\neq k}^{N} \frac{4F_i\hat{\rho}_{ik}}{\pi^2 E^* a_f}\left[\mathbf{E}\left(\frac{1}{\hat{\rho}_{ik}^2}\right) - \left(1-\frac{1}{\hat{\rho}_{ik}^2}\right)\mathbf{K}\left(\frac{1}{\hat{\rho}_{ik}^2}\right)\right] \tag{2.20}$$

where F_i is the force acting on the i^{th} fibril, and $\hat{\rho}_{ik}$ is the normalized the distance between the center of i^{th} and k^{th} fibril, which can be expressed as $\hat{\rho}_{ik} \equiv \frac{|\mathbf{r}_k - \mathbf{r}_i|}{a_f}$. We

further add to this the displacement due to the fibril itself, given by (2.16), to find the total displacement of the k^{th} fibril, V_k.

Next, consider the unloading process of a rigid indenter which is initially compressed into the fibrillar array and subsequently has its contact area pinned. The incremental vertical displacement Δ on the fibrils is uniform. Therefore, for each fibril k, we have

$$V_k = u_k^f + u_k^s = \frac{F_k L}{E\pi a_f^2} + \sum_{j=1}^{N} b_{kj} \frac{4F_j}{E^* \pi^2 a_f} = \Delta \tag{2.21}$$

where

$$b_{kj} \equiv \begin{cases} \hat{\rho}_{kj}\left[\mathbf{E}\left(\frac{1}{\hat{\rho}_{kj}^2}\right) - \left(1-\frac{1}{\hat{\rho}_{kj}^2}\right)\mathbf{K}\left(\frac{1}{\hat{\rho}_{kj}^2}\right)\right] & j \neq k \\ 56/45 & j = k \end{cases}. \tag{2.22}$$

Equation (2.21) applies for each of the N fibrils. Together, this set of linear equations is solved numerically to determine the N unknown fibrillar forces F_j for given Δ. The compliance is then computed as $C_{eff} \equiv \Delta / F$ where F is the total force, $\sum_{k=1}^{N} F_k$.

Predictions of this model are compared with experimental measurements of compliance in Figure 2.15 for a sample with fibril height of 53 μm and three different fibril spacings. (Data and predictions for other samples are provided in Figure A2.1 in the appendix.) Fibrils are square in cross-section and have a designed width of 14 μm. Actual dimensions are somewhat higher and vary along the fibril height. For these reasons, we allow the fibril radius in the model to vary as a fitting parameter. Results shown in Figure 2.12 are with a width of 17 μm from which we calculate an effective radius for use in the model by equating the cross-sectional area so that $a_f = 9.6\mu m$. Compliance as a function of contact area is found by varying the number of fibrils N according to equation (2.15).

For moderate contact area, there is very good agreement between the model

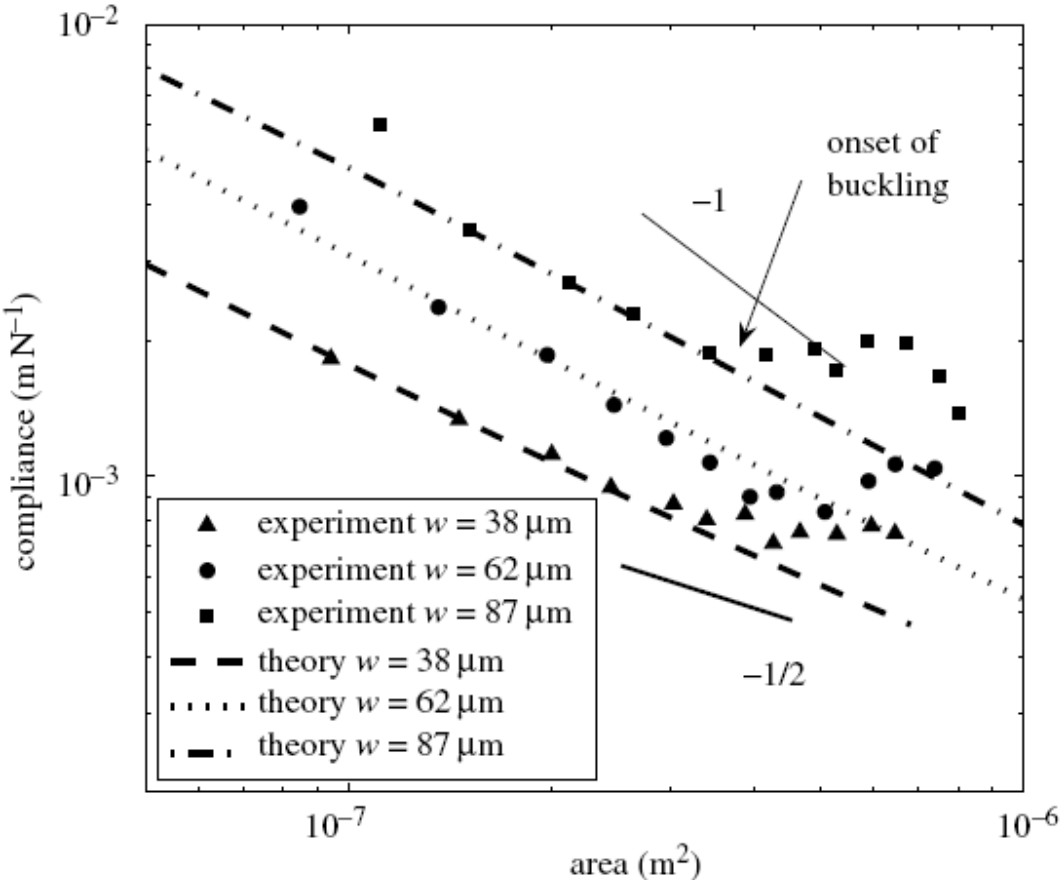

Figure 2.15 Theoretical and experimental results for compliance as a function of contact area for fixed fibril height and varying spacing. The solid lines represent the theoretical prediction and the points are experiment results.

experiment. (See also the data in the Figure A2.1.) However, at a certain area, there is a marked departure of the experimental trend from the theory. It is observed experimentally that this change occurs when compressive loads are sufficient to cause buckling of fibrils, as discussed later. Buckling significantly increases the contact compliance. A comparison of the fibril and substrate displacement components (given by equations (2.16) and (2.20), respectively) reveals that in most of the experimental cases examined here, compliance is dominated by the fibrillar layer. Thus, it is not surprising that buckling of the fibrils strongly influences the overall compliance.

Direct evidence of buckling and its effect on the material response is shown in Figure 2.16. We see an inflection in the load-displacement curve between points 'a' and 'b'. The micrographs corresponding to these points clearly show that this feature corresponds to buckling of compressively loaded fibrils. It is interesting to note that unlike in 1-level structures (Sharp *et al*. 2004, Glassmaker *et al*. 2004), this buckling is not detrimental to the adhesion. Note also that the terminal film plays a stiffening role keeping the fibrils apart and preventing lateral collapse, which is another common problem associated with 1-level structures.

It is instructive to examine two limiting cases in which fibrils are very short, $h \to 0$, or very long. In the first case, compliance is dominated by the substrate and one expects it to scale with the contact area according to the Boussinesq flat punch solution for a circular region on the surface of an elastic half-space with uniform applied vertical displacement, *i.e.,* as inverse square root of the contact area (equation (2.2)). This is indicated in Figure 2.15 by the line with a slope of -1/2. When the fibrils are long, they dominate the compliance and since their number increases linearly with the contact area, the compliance in this limit should scale inversely with contact area. This is indicated in Figure 2.12 by a slope of -1. Our model and the experiments fall between these two limits, somewhat closer to the latter.

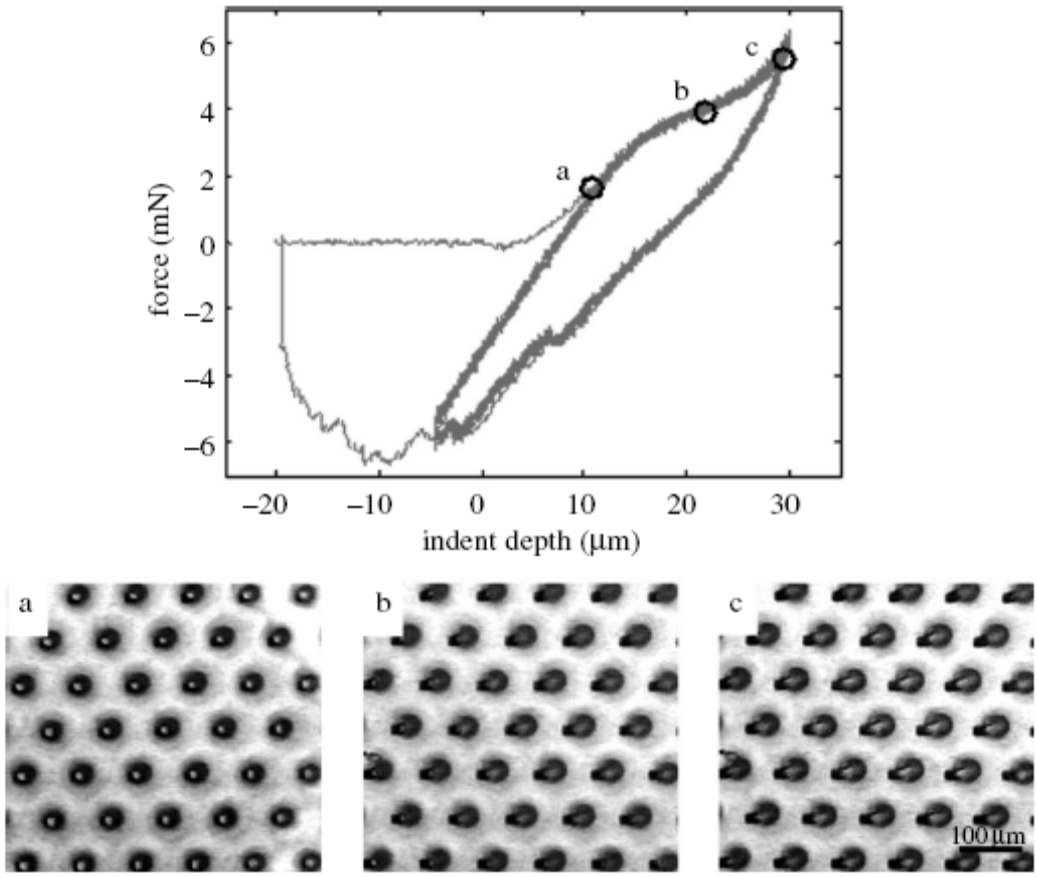

Figure 2.16 Indenter depth vs. force plot of the sample with the shortest fibrils (S87H53) with optical micrographs of fibrillar buckling at various indenter depths.

Figure 2.17 shows data for normalized compliance as a function of contact area for samples with a fibril length of 53 μm. Recall that the measured fibrillar compliance is normalized by the Boussinesq compliance, given in equation (2.2). Normalized compliance decreases towards an asymptotic value with increasing contact area. The increase in normalized compliance beyond an area of about 0.4 sq. microns is due to buckling of fibrils. Data from all nine samples at a fixed value of contact area $4 \cdot 10^5$ μm^2 are given in the Figure A2.2. They confirm that there is a systematic increase in compliance with spacing between fibrils, as expected. The effect of fibril height is less clear due to the narrow range tested experimentally.

2.5 Summary

We have fabricated and studied a new type of synthetic fibrillar adhesion surface, inspired by biological setal systems, which consists of an array of fibrils terminated by a continuous film. The film-terminated fibrillar interface studied in this paper has demonstrated enhanced contact compliance and adhesion as measured by hysteresis, pull-off force, and absolute works of adhesion. Adhesion and hysteresis enhancement in our system is due to a crack trapping mechanism, which we have explored theoretically using a two-dimensional model. The crack is trapped under the thin film between fibrils. Because the film is thin, pillars near the advancing crack front alternately absorb and release elastic energy. The absorption process is stable whereas the release is unstable, resulting in energy loss. The crack trapping mechanism predicts that the work of adhesion will be reduced and the work of separation increased relative to a flat control, which we have shown to occur in the experiments. For a crack propagating to the right, consistent with observations, the model also predicts that on opening the crack will be trapped at the left edge of a fibril while on closing (retraction to the left), the crack will be trapped at the right fibril edge.

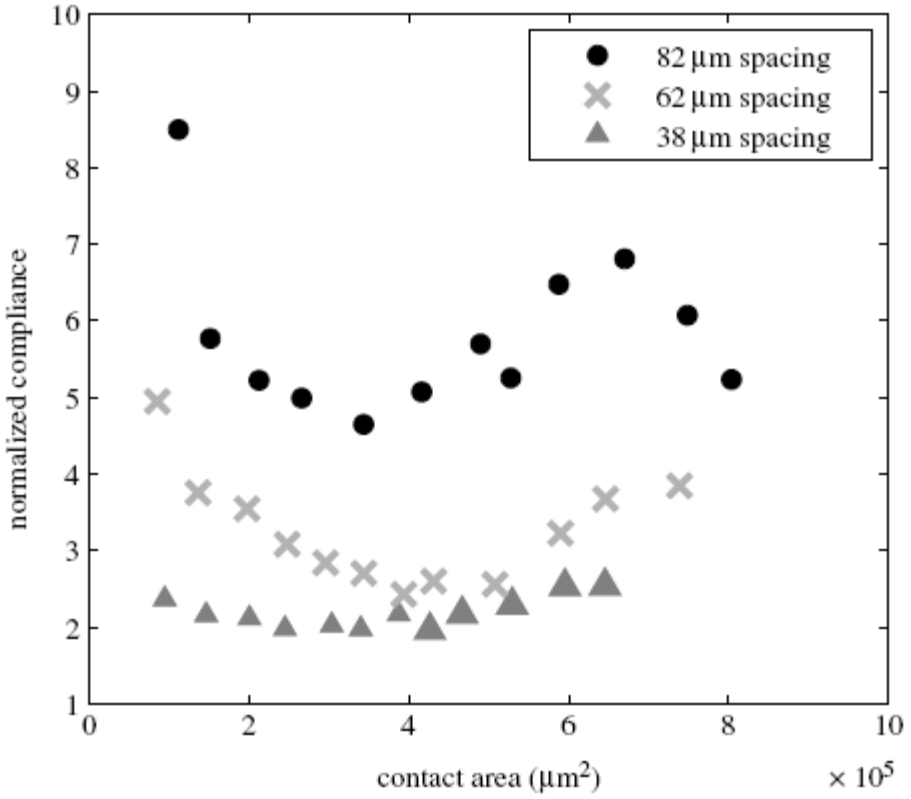

Figure 2.17 Indenter area versus the normalized compliance for samples with a fibrillar height of 53 μm.

It hops dynamically from one trapped location to the next.

While the two-dimensional model captures several features of interfacial separation and healing, there are important three-dimensional effects that render it quantitatively inaccurate. For example, for similar dimensions, the 2D predicted adhesion enhancement factor $1/\phi_{\min}$ is considerably larger than measured experimentally. Also, it increases without bound in the two-dimensional model as fibril separation is increased with other geometrical parameters held constant. In contrast, our experiments indicate that there is an optimal separation (and fibril height) corresponding to maximum adhesion enhancement. This is a three-dimensional effect that results from a competition between two tendencies: increased separation (a) increases the energy stored in each fibril at the point of instability, (b) decreases the number of fibrils available per unit area. This mechanism for energy enhancement is somewhat different from the one proposed previously for fibrillar interfaces (Jagota and Bennison 2002, Glassmaker *et al*. 2005) and similar to the lattice trapping argument for crystalline solids (Thomson *et al*. 1971, Rice 1978).

The samples we have discussed here were made entirely of PDMS and were indented with a sphere having a hydrophobic coating. While this has allowed us to study the adhesion enhancement process relatively cleanly, it also means that absolute values of adhesion energy remain modest. It is our expectation that the adhesion enhancement can be increased by coupling it to stronger and possibly dissipative adhesive processes. The process we have used could be applied to other materials. For materials that cannot be molded, direct etching techniques can be used to produce arrays of posts (Glassmaker *et al*. 2004).

REFERENCES

[1] Arzt, E., Gorb, S. & Spolenak, R. 2003, *Proc. Natl. Acad. Sci. USA* **100**, 10603-10606.

[2] Autumn, K., Liang, Y.A., Hsieh, T.S., Zesch, W., Chan, W.P., Kenny, T.W., Fearing, R. & Full, R.J. 2000, *Nature* **405,** 681-685. (DOI 10.1038/35015073)

[3] Eisner, T. & Aneshansley, D.J. 2000, *Proc. Natl. Acad. Sci. USA* **97** 6568-6573.

[4] Ghatak, A., Vorvolakos, K., She, H., Malotky, D.L. & Chaudhury, M.K. 2000, *J. Phys. Chem. B* **104,** 4018-4030.

[5] Glassmaker, N.J., Jagota, A., Hui, C-Y. & Kim, J. 2004, *J. R. Soc. Interface* **1,** 22-33.

[6] Glassmaker, N.J., Jagota, A., Hui, C-Y., Noderer W.L., & Chaudhury, M.K. 2007, *Proc. Natl. Acad. Sci.* USA **104**, 10 786-10 791.

[7] Glassmaker N.J., Jagota A. Hui C-Y., Chaudhury M.K., 2006, *Proceedings of the Annual Meeting of the Adhesion Society*.

[8] Glassmaker, N.J., Jagota, A. & Hui, C-Y. 2005, *Acta Biomaterialia* **1**, 367-375.

[9] Gorb S., Varenberg M., Peressadko A., & Tuma J., 2006, *J. R. Soc. Interface*: 1-6.

[10] Gorb, S. & Scherge, M. 2000 *Proc. R. Soc. London B* **267,** 1239-1244.

[11] Hiller, U. 1976, *J. Bombay Nat. Hist. Soc.* **73**, 278-282.

[12] Hiller, U. 1968, *Z. Morph. Tiere* **62**, 307-362.

[13] Hui, C-Y., Glassmaker, N.J., Tang, T. & Jagota, A. 2004, *J. R. Soc. Interface* **1**, 35-48.

[14] Hui, C-Y., Glassmaker, N.J. & Jagota, A. 2005, *J. Adhes.* **81**, 699-721.

[15] Hui, C-Y., Jagota, A., Lin, Y.Y. & Kramer, E.J. 2002,*Langmuir* **18**, 1394-1404.

[16] Jagota, A. & Bennison, S.J. 2002, *Integr. Comp. Biol.* **42**, 1140-1145.

[17] Jagota, A, Hui C-Y, Glassmaker N J & Tang T 2007 *MRS Bulletin* **32** 492-495.

[18] Johnson K.L., 1985 *Contact Mechanics*, Cambridge University Press.

[19] Johnson K.L., Kendall, K, & Roberts, A.D., 1971, *Proc. R. Soc.* **A324** 301.

[20] Kim S., Sitti M., 2006, *Appl. Phys. Lett.* **89** (26): 261911.

[21] Majidi, C., Groff, R.E., Maeno, Y., Schubert, B., Baek, S., Bush, B., Maboudian, R., Gravish, N., Wilkinson, M., Autumn, K. & Fearing, R.S. 2006, *Phys. Rev. Lett.* **97**, 076103.

[22] Noderer, W.L., Shen, L., Vajpayee, S. Glassmaker, N.J. Jagota, A. & Hui, C-Y. 2007, *Proc. R. Soc* A **463**, 2631-2654.

[23] Rizzo, N.W., Gardner, K.H., Walls, D.J., Keiper-Hrynko, N.M., Ganzke, T.S. & Hallahan, D.L. 2006, *J. R. Soc. Interface* **3**, 441-451.

[24] Peressadko A. & Gorb S.N. 2004, *J. Adhes.* **80**, 247-261.

[25] Persson, B.N.J. 2003, *J. Chem. Phys.* **118**, 7614-7621.

[26] Persson, B.N.J. & Gorb, S. 2003, *J. Chem. Phys.* **119**, 11437-11444.

[27] Rice, J. R. 1978, *J. Mech. Phys. Solids*. **26,** 61-78.

[28] Ruibal R. & Ernst, V. 1965, *J. Morphology* **117**, 271-294.

[29] Scherge, M., Gorb, S.N. 2001 *Biological Micro and Nanotribology: Nature's Solutions*. Springer-Verlag (Berlin).

[30] Sharp, K.G., Blackman, G.S., Glassmaker, N.J., Jagota, A. & Hui, C-Y. 2004, *Langmuir* **20**, 6430-6438.

[31] Shull, K.R. 2002, *Mat. Sci. and Eng. R. Rep.* **36**, 1.

[32] Sitti, M. & Fearing, R.S. 2003, *J. Adhes. Sci. Tech.* **17**, 1055-1073.

[33] Thomson, R., Hsieh, C., & Rana, V. 1971 *J. Appl. Phys.*, **42,** 3154-3160.

[34] Williams, E.E. & Peterson, J.A. 1982, *Science* **215**, 1509-1511.

[35] Yurdumakan, B., Raravikar, N.R., Ajayan, P.M. & Dhinojwala, A. 2005, *Chem. Comm.* **30**, 3799-3801.

APPENDIX 2

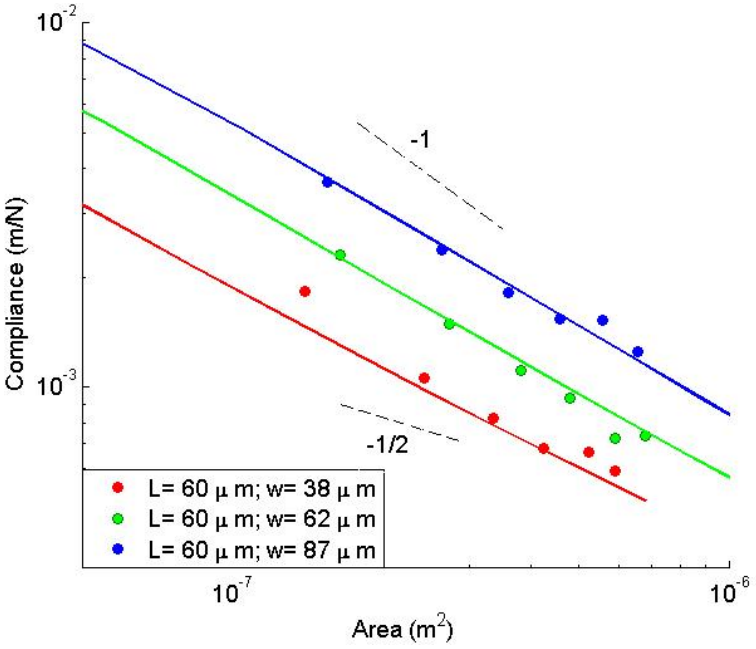

(a)

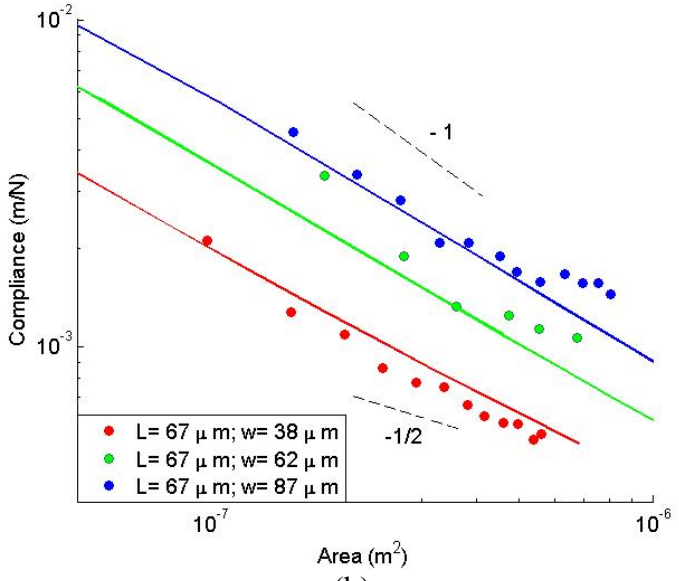

(b)

Figure A2.1 Predicted and measured contact compliance for samples with fibril height (a) 60 microns, and (b) 67 microns.

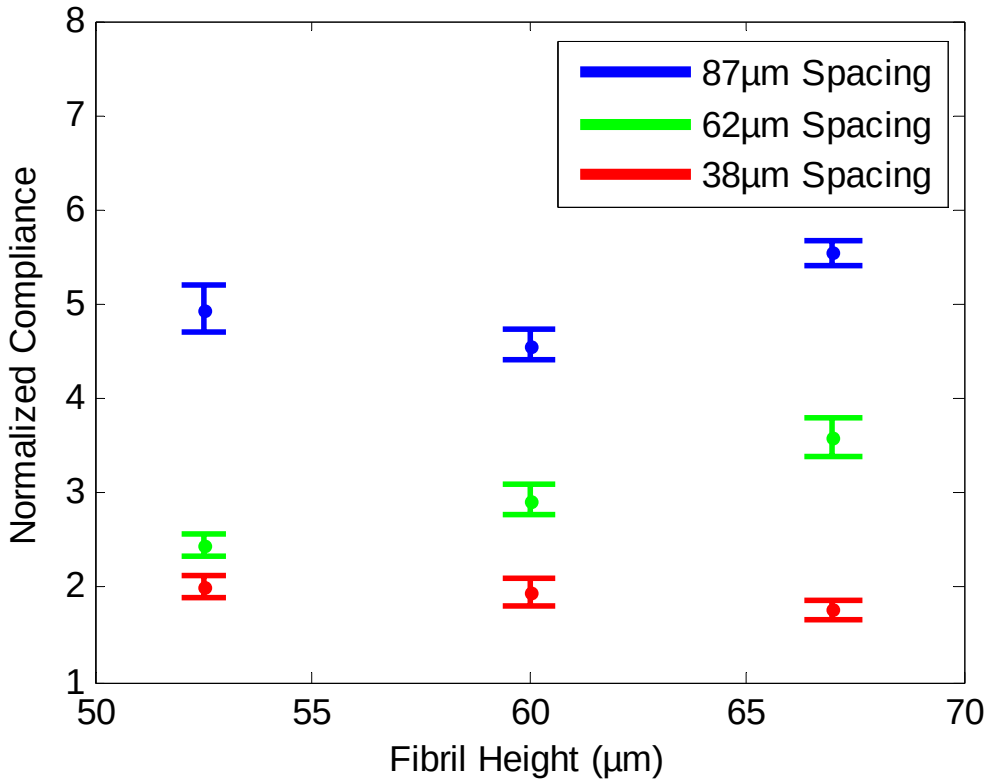

Figure A2.2 Normalized compliance as a funcntion of fibril height for different fibril spacing when the contact area is about $4 \cdot 10^5$ μm^2.

CHAPTER 3

A TWO-DIMENSIONAL MODEL FOR ENHANCED ADHESION OF FILM-TERMINATED FIBRILLAR INTERFACES BY CRACK TRAPPING

3.1 Abstract

Experiments on a recently developed bio-inspired film-terminated fibrillar array show significantly enhanced adhesion compared to a flat unstructured control sample. Adhesion is enhanced because the interfacial crack is trapped close to fibril edges. We analyze a two dimensional version of the fibrillar structure to understand the behavior observed in experiments. Several experimental observations are explained by model predictions: (1) the work to separate a unit area of the interface (W^+) is larger than the work of adhesion (W_{ad}) of the flat control sample; (2) the work to heal a unit area of the interface (W^-) is smaller than the work of adhesion of the flat control sample; (3) W^+ increases with fibril spacing; (4) W^+ decreases with film thickness; (5) W^+ decreases with fibril height.

3.2 Introduction

Many small animals and insects use a structured fibrillar interface on their feet to make contact and to adhere to surfaces [1-7]. The strength and toughness of these fibrillar structures are superior to those of unstructured interfaces made of the same material. This feature has motivated many researchers to fabricate synthetic fibrillar structures and to study their contact mechanics and adhesion [8-23]. Early attempts produced single level micro-fiber structures which have higher adhesion per unit area of actual contact compared to a flat control [8, 12]. However the overall actual

adhesion was still weaker than that of the flat control. Several groups have developed structures with significantly enhanced adhesion [13, 16-18, 21, 22].

In this chapter we examine the adhesion enhancement mechanism for the film-terminated fibrillar structure reported by Glassmaker *et al* [16]. This structure consists of a micro-fiber arrays topped by a thin film. The interfacial fracture toughness of this fibrillar structure is found to be up to 5 times greater than that of a flat control sample in a double cantilever beam (DCB) fracture test [16]. This result is consistent with the hysteresis measured in indentation tests [17]. At first glance it may seem counter-intuitive that a purely elastic system (our fibrillar material is PDMS, which is elastic) exhibits hysteresis. In the previous chapter we suggested enhanced adhesion caused by hysteresis is due to the trapping of the interface crack front in the thin film region between fibrils [16, 17]. Crack trapping is a consequence of the variation of local energy release rate with crack front location. For example, when the crack lies underneath the thin film between fibrils, the local energy available for crack propagation is small, as most of the energy supplied by the external load is absorbed by the fibrils. This absorbed energy can be much greater than the work needed to grow the interface crack and is released in an unstable manner when the crack front passes underneath the fibril.

The fact that a purely elastic system can be designed to exhibit hysteretic behavior has important consequence for adhesion, because most adhesives are not reusable as plastic deformation invariably changes the geometry of the adhesive making it less likely to stick to surfaces after a first few usages. As will be shown below, the amount of hysteresis (and hence adhesion) can be enhanced by changing the architecture of the structure such as inter-fibril spacing, height and film thickness. Our previous analysis did not study how the local energy release rate varies with geometric parameters such as film thickness, fibril height and fibril spacing [17]. The

goal of this paper is to study how these parameters control the crack trapping mechanism.

The plan of this chapter is as follows. In section 3.3, we summarize the crack trapping mechanism by reviewing observations from indentation experiments. In section 3.4, we introduce an idealized two-dimensional (2D) model for crack trapping in a periodic structure. The model is solved using the finite element method (FEM). In section 3.5 we use the model to study the effect of fibrillar geometry on adhesion. Limitations of the 2D model are discussed in section 3.6.

3.3 Experimental Observation of Crack Trapping

Figure 1.2 shows schematically a fibrillar interface indented by a glass sphere. The fibrillar structure is made by molding poly(dimethylsiloxane) (PDMS) into a silicon master [16,17]. The fibrils are part of a thick backing layer and they are arranged in a hexagonal pattern. A thin PDMS film is bonded to the top of the fibrils which are oriented vertically to the backing layer. Samples are prepared with different fibril spacing and height. Also, a flat unstructured sample is used as a control in our experiments. Details of experiment procedures and test results can be found in [17]. Briefly, indentation tests were carried out in a custom apparatus built on an inverted optical microscope. The indentation was carried out at a constant rate until its displacement reached a specified value, after which it was retracted at the same rate. Force and displacement, P, δ, were measured continuously and images of the contact plane were recorded. It was shown that the pull-off force and effective work of adhesion measured in indentation experiments are nearly four to five times greater than those for a flat control sample.

A useful way of thinking about the indentation test is to view the air gap between the indenter and the fibrillar surface as an external interfacial crack, with the

crack front being the contact line (see Figure 1.2a). During indentation, crack healing occurs as the contact area increases. During retraction, crack growth occurs as the contact area decreases. Figure 3.1 shows a sequence of micrographs of the contact plane as the indenter is indented then retracted. Images are separated by equal time intervals of 1 second. Dark regions represent contact; light regions the crack (air gap). While the contact line moves smoothly in the flat control samples, in the fibrillar specimens it is usually static, punctuated by sudden (unstable) motion across one or more fibrils. For example, the arrow on the first indentation panel (a) of Figure 3.1 shows that on closure, the crack is trapped on the left edge of fibrils. Indentation panels (c,d,) isolate a part of a trapped crack front and (e) shows the trapped crack front jumping across a fibril. The first retraction panel (A) shows part of the crack front trapped by the right edge of a fibril. In panel (E), the crack jumps across this fibril.

3.4. Crack trapping model

Analysis of crack trapping mechanism in the experimental geometry is difficult since it involves solving a three dimensional problem of crack propagation where the location and shape of the crack front are not known *a priori*. As shown in Figure 3.1, the crack front does not jump uniformly along the pinned contact line, indicating that the process is affected by local strength statistics. Fortunately, many of the salient features of the crack trapping mechanism can be studied using an idealized plane stress model with a simpler loading geometry, as shown in Figure 3.2. In this idealized model, the material is assumed to be isotropic are linearly elastic with Young's modulus E. The backing layer is a very long strip with width L, thickness T (out of plane) and height H. A single row of micro-fibers with width b is attached to the bottom of the backing layer as shown in Figure 3.2. The micro-fibers have height

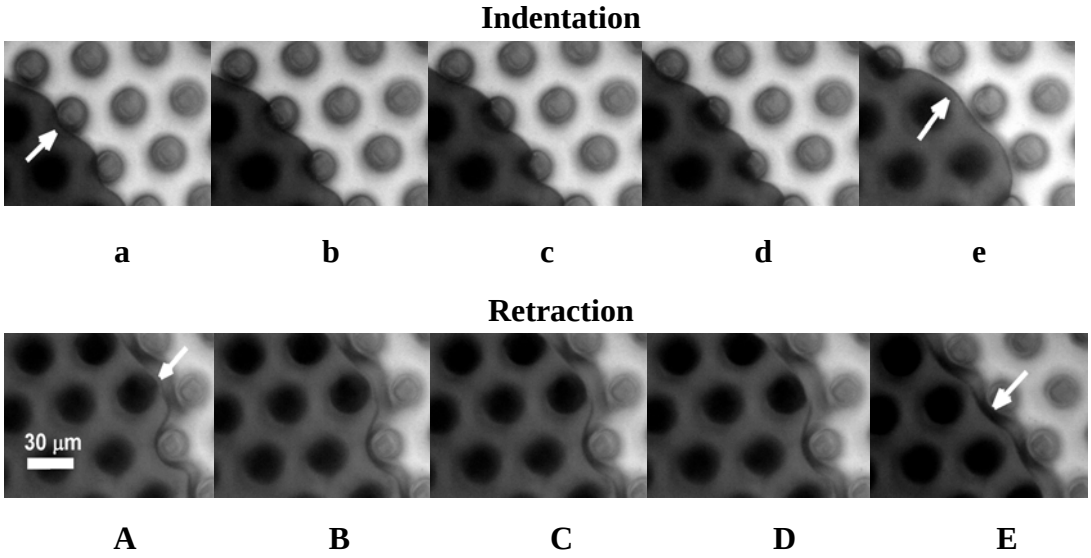

Figure 3.1 Micrographs of the contact plane. The indenter is in contact with the surface in the dark region; lighter regions is the air gap between the material and the indenter (indicate in figure).

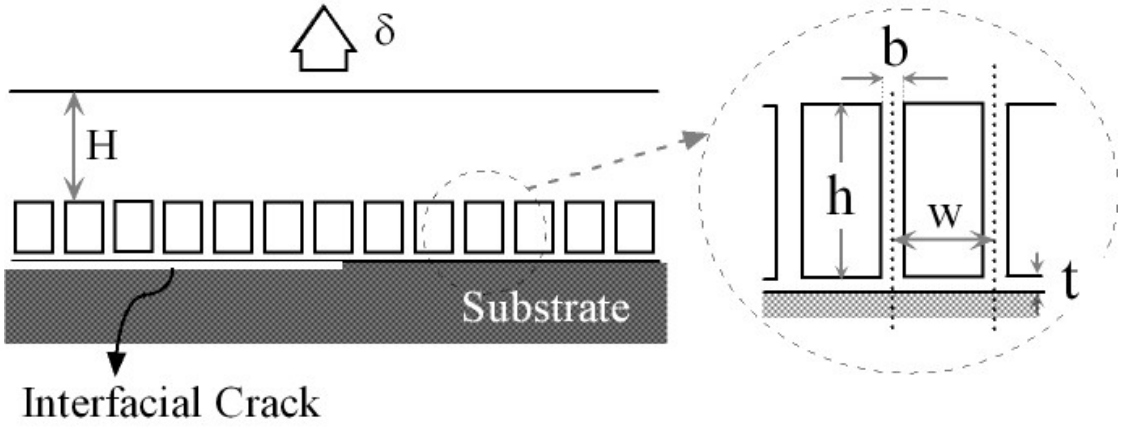

Figure. 3.2 Loading Geometry. The backing layer (strip) has thickness $H >> h$, the fibril height. The ends of the fibrils are bonded to a continuous thin film with thickness t. Half of the thin film is in adhesive contact with the substrate while the other half is not, thus forming an interface crack. The closest center to center distance between two fibrils is w and the width of a fibril is b. The displacement δ can be applied by bonding the top of the strip to a rigid plate.

h and with minimum distance between them denoted by *w*. The fibrils are terminated by a thin film of thickness *t*. We assume that *L* is much greater than *H, h* and *t*, so that the strip can be considered infinite in width. Half of the film is in adhesive contact with a rigid substrate; the remaining half is not in contact, forming a semi-infinite interface crack. A uniform vertical displacement, δ, is applied to the upper surface of the backing layer (strip).

Our goal is to determine how the local energy release rate of the interface crack, *G,* depends on the position of its tip. The periodicity of the fibrils implies that the deformation and stress fields are periodic function of location with period *w*. Specifically, $G(x)=G(x+w)$. The conditions required for stable crack growth are [26]:

$$G=W_{ad} \tag{3.1a}$$

and

$$dG/dx<0 \tag{3.1b}$$

The first condition states that crack growth can occur when the energy release rate is equal to the intrinsic work of adhesion W_{ad} between the thin film and the substrate. The second condition states the fact that crack advance is *stable* if the applied loading is such that the local energy release rate is a decreasing function of crack advance.

Dimensional analysis and linearity imply that *G* can be written as

$$G = G_0\phi(x/b, w/b, t/b, h/b, H/b), \tag{3.2}$$

where

$$G_0=2E\delta^2/3H \tag{3.3}$$

and ϕ is a dimensionless function of its dimensionless arguments. In (3.2), we have made the simplifying assumption that the Poisson's ratio is ½, that is, the material of the strip is incompressible, which is a good approximation for PDMS. Note that G_0 is the energy release rate of the same strip, except that the bottom surface is flat (that is, without the fibrils and thin film [26]). Since $h << H$, G_0 can be viewed as the

average applied energy release rate, *i.e.*, the quantity that an external observer (unaware of the fibrillar interface) would measure as the toughness of the interface. The variation of the normalized energy release rate $G/G_0 = \phi$ with the position of the crack tip, x, inside a unit cell is computed using the finite element method using ABAQUS 6.5; details are given in Appendix 3.) A typical plot of G versus x is shown in Figure 3.3. The parameters used to generate Figure 3.3 are w/b = 13/3, h/b= 20/3, t/b=2/3. The vertical dashed lines in Figure 3.3 show the position of the fibril edges relative to the crack tip. The normalized local energy release rate curve has two important features. It has a minimum at the point A-C and a maximum at the point a-c. The minimum, ϕ_{min}, occurs close to the left edge of the fibril whereas the maximum, ϕ_{max}, occurs near the right edge.

To understand the mechanics of crack trapping, assume that the crack tip is initially located between fibrils and is to the *left* of x_{min} as shown in Figure 3.1. To grow the crack, we gradually increase the applied displacement δ from zero. Equation (3.2) and (3.3) implies that $G \propto G_0 \propto \delta^2$. The condition (3.1a) can be written as:

$$G/G_0 = W_{ad}/G_0 \tag{3.4}$$

and is shown as the horizontal line in Figure 3.3. Equation (3.4) states that in order for the crack to grow, the normalized energy release rate versus crack position curve in Figure 3.3 must intersect the horizontal line (see Figure 3.3). From (3.2), the *normalized* energy release rate, G/G_0, versus crack position curve in Figure 3.3 does not change with δ. Since $G_0 \propto \delta^2$, the horizontal line defined by (3.4) moves vertically downwards as δ increases, eventually intersecting the normalized local energy release rate curve (see Figure 3.3). Note that the slope of the normalized local energy release rate at this intersection is negative, indicating that crack growth is stable, that is, the crack tip will stay in this position at fixed δ. With further increase

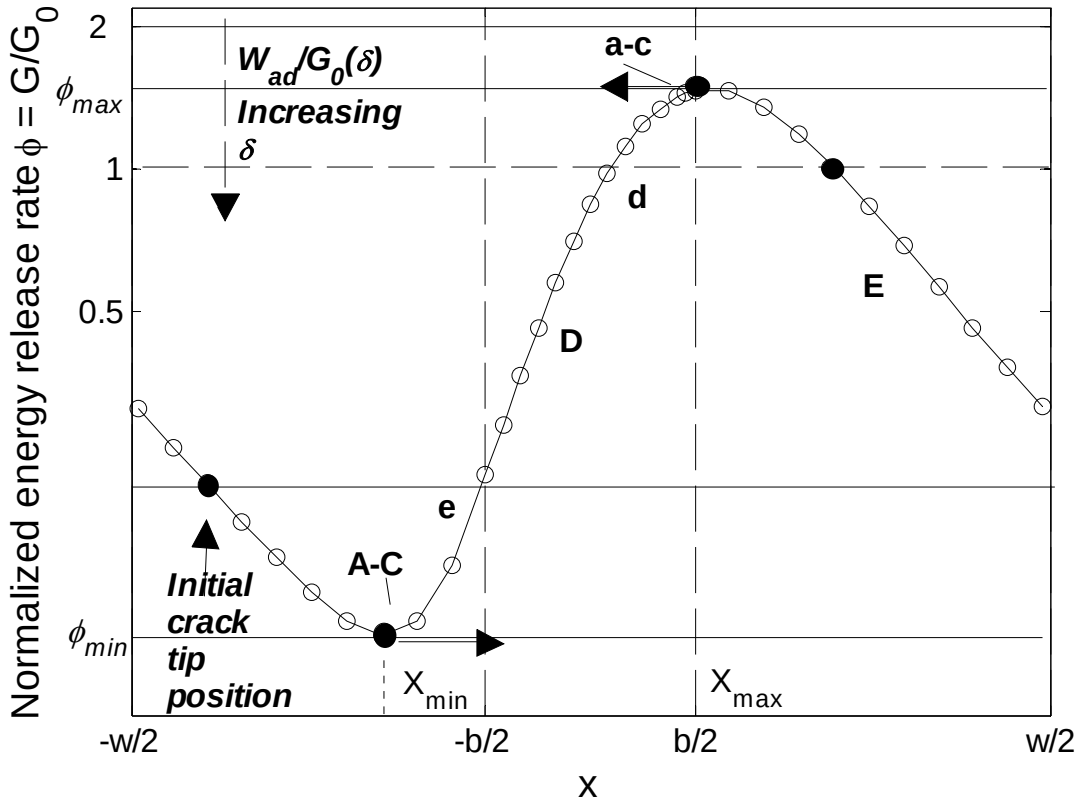

Figure 3.3. Variation of normalized energy release rate G/G_0 with respect to position of crack tip x. Points A-C and a-c represent locations where the crack is trapped during opening and healing, respectively. For example, point A in this figure corresponds roughly to the situation shown in panel A in Figure 3.1.

of δ, the crack tip moves stably to the right until it reaches the point where ϕ is minimum (i.e., $dG/dx = 0$). When the crack tip is in this position, i.e., when $x = x_{min}$, the applied displacement has reached its maximum, which we denoted by δ_{max}. Since $dG/dx>0$ when the crack tip goes beyond x_{min}, any slight increase in applied displacement will result in unstable crack growth. In other words, when δ reaches δ_{max}, the crack will jump from x_{min} to the next trapped position a distance w away. Physically, this jump occurs when the fibrils have absorbed the maximum amount of elastic energy.

A similar argument applies to crack healing. Suppose the crack tip is to the right of x_{max} in Figure 3.3. Reducing the applied displacement will move the horizontal line in Figure 3.3 upwards, and the crack will move stably to the left (i.e., it will heal) In this case, the minimum applied displacement needed for crack healing, δ_{min}, will depend on the crack position x_{max} where ϕ achieves its maximum $\phi_{\max}$. As shown in Figure 3.3, $\phi_{\max}$ is located at the right edge of the fibril. After the crack tip passes x_{max}, any slight decrease in the applied displacement results in unstable crack closure.

Note that, if the strip were flat, that is, there were no fibrils, the energy release rate is G_o and the displacement required for crack growth and closure (healing) would be identical, that is, $G_o = W_{ad}$. This condition and equation (3.3) imply that the critical applied displacement for crack growth to take place in a flat control is

$$\delta_{flat}^2 = 3HW_{ad}/2E\,. \tag{3.5a}$$

Equation (3.2) implies that

$$\delta_{\max}^2 = 3HW_{ad}/2E\phi_{\min}\,. \tag{3.5b}$$

Taking the ratio of (3.5a) and (3.5b) results in

$$\delta_{\max}^2/\delta_{flat}^2 = 1/\phi_{\min}\,. \tag{3.6}$$

According to (3.6), an external observer unaware of the microstructure will find that it takes a greater applied displacement to separate the interface. Since the fibril height is small compared to the layer thickness, $h << H$, and the material modulus is the same, this observer will conclude by applying equation (3.3) that the effective work of adhesion of the interface has increased by a factor of $1/\phi_{\min}$. Note that the arrested crack would always be found to the left of a fibril. For crack closure the equivalent statement to equation (3.6) is

$$\delta_{\min}^2 / \delta_{flat}^2 = 1/\phi_{\max} \tag{3.7}$$

and the external observer will conclude that the effective work of adhesion for crack closure is reduced by a factor of $1/\phi_{\max}$. Note that both $\phi_{\min}$ and $\phi_{\max}$ depend only on geometry. Since G_o can be interpreted as the applied energy release rate, equations (3.6) and (3.7) suggest defining two new quantities, W^+, the effective work of separating a unit area of the interface and W^-, the effective work of healing a unit area of the interface, W^-. They are related to $\phi_{\min}$ and $\phi_{\max}$ by

$$W^+ = W_{ad}/\phi_{\min};\quad W^- = W_{ad}/\phi_{\max} \tag{3.8 a, b}$$

Notice that since $\phi_{\min} \ll \phi_{\max}$ (see Figure 3.3), W^- is small compare to W^+.

According to (3.8a), the external loading device release energy at a rate in excess of that required by the interface itself. The second equation (3.8b) indicates that energy is given back to the loading device. Suppose we have a perfect loading device which can continuously adjust the applied displacement in such a way so as to allow the crack to traverse the entire periodic cell stably, then the average energy release rate must equal the intrinsic work of adhesion. Using (3.2) this condition is,

$$\frac{E\delta^2}{Hw}\int_0^w \phi(x/b,...)dx = W_{ad} \tag{3.9}$$

However, under realistic loading conditions (e.g. monotonically increasing displacement), the part of the loading cycle where the stored energy is released is

unstable and most of the released energy is not recoverable. This mechanism of energy dissipation is similar to that of lattice trapping discussed by Thomson *et al* in [27], where the periodicity and discreteness of the lattice structure caused the stress intensity factor for crack growth to be greater than that required for crack healing. Rice [28] has examined the connection between entropy production and irreversible quasi-static crack propagation, using lattice trapping as an example.

3.5 Effect of Geometrical Parameters on Adhesion Enhancement

The important geometrical parameters that control the adhesion enhancement are fibril width, fibril spacing, film thickness, and fibril height. Experiments [16, 17] have shown that adhesion enhancement increases with spacing and height up to a critical value after which adhesion eventually decreases. To understand how these parameters control adhesion, we use a finite element model (see appendix 3) to determine the normalized local energy release rate for fibrillar structures with different *w/b, t/b,* and *h/b*. The parameters are chosen so that they are similar to those in our experiments [16, 17] even though the model is two dimensional. The finite element results are summarized in Figures 3.4(a-c). As in Figure 3.3, the vertical dotted lines in these figures denote the location of the fibril edges. In Figure 3.4(a), the normalized fibril spacing *w/b* varies from 8/3 to 18/3 where *h /b* =20/3, *t/b* = 2/15. In Figure 3.4(b), the normalized film thickness *t/b* varies from 1/15 to 2/3 while *h/b* and *w/b* are fixed at 20/3 and 13/3 respectively. In Figure 3.4(c), the normalized fibril length varies from 10/3 to 10 with *w/b* = 13/3, t/*b* = 2/15.

The results in Figure 3.4 (a)-(c) show that $\phi_{\min}$ (the minimum value of normalized energy release rate *G*) decreases with increasing fibril spacing while $\phi_{\max}$ (the maximum value of *normalized G*) increases with it. On the other hand, $\phi_{\min}$ increases with both film thickness and fibril height while $\phi_{\max}$ decreases with them.

Figure 3.4 (a), (b), (c) Variation of normalized energy release rate G/G_0 with respect to position of crack tip x. The vertical dotted lines are fibril edges. In Figure 3.4 (a), h/b =20/3, t/b = 2/15, w/b varies from 8/3 to 18/3. In Figure 3.4 (b), w/b = 13/3, h/b = 20/3, t/b varies from 1/15 to 2/3. In Figure 3.4 (c), t/b = 2/15, w/b = 13/3 and h/b varies from 10/3 to 10.

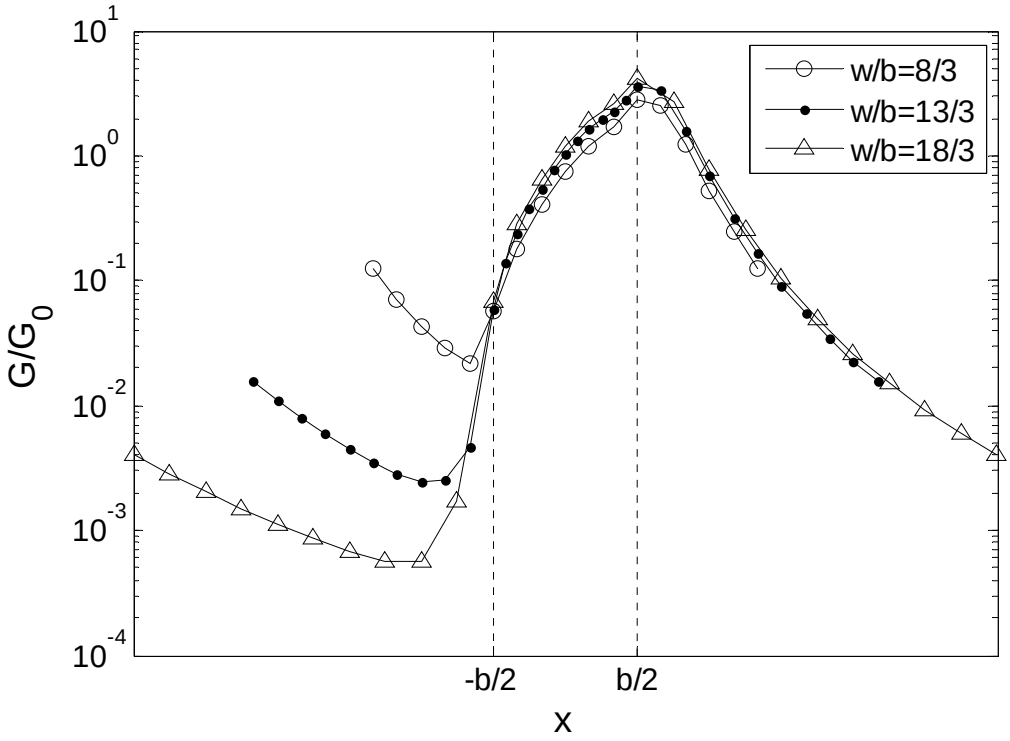
10^{1}
10^{0}
10^{-1}
10^{-2}
10^{-3}
10^{-4}
G/G$_0$
w/b=8/3
w/b=13/3
w/b=18/3
-b/2
b/2
x

(a)

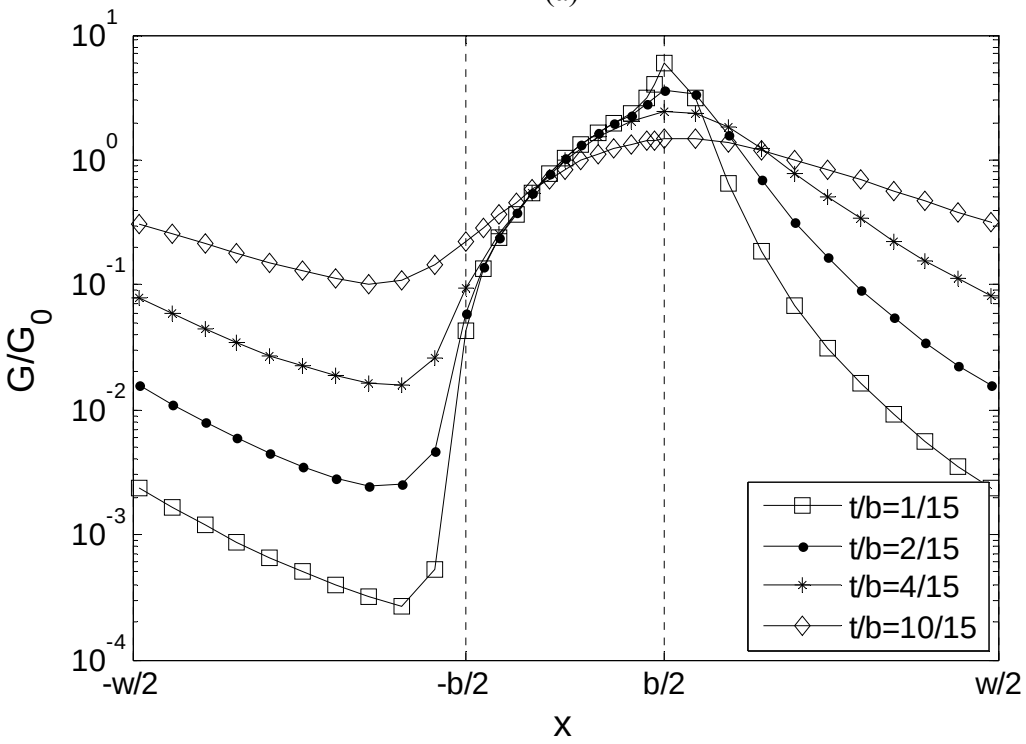
10^{1}
10^{0}
10^{-1}
10^{-2}
10^{-3}
10^{-4}
G/G$_0$
t/b=1/15
t/b=2/15
t/b=4/15
t/b=10/15
-w/2
-b/2
b/2
w/2
x

(b)

Figure 3.4 (Continued)

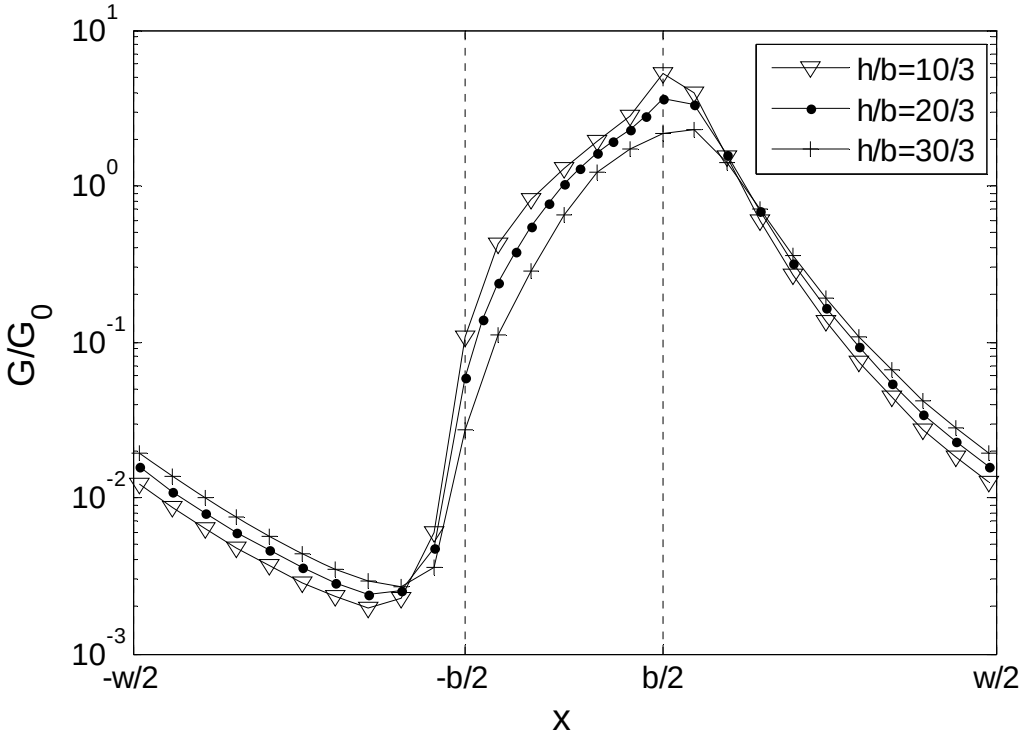

(c)

These results are not unexpected. When the crack tip is between two fibrils, the energy available to drive the crack comes primarily from the strain energy stored in the bent film. One can roughly estimate the stored energy in the film by modeling it as an elastic cantilever beam of length w on a rigid substrate (see Figure 3.5). Our finite element results show that $\phi_{\min}$ occurs near the left edge of a fibril. Therefore in Figure 3.5, the crack tip is close to the left edge of fibril (1) (dotted line). Let Δ denote the displacement of the beam at the location of fibril (0) (see Figure 3.5). The elastic energy is $\Gamma = (E\Delta^2 Bt^3)/(8w^3)$, where B is out of plane width of the film and for the same Δ, a longer and thinner beam store less energy than a shorter and thicker one. The energy release rate $G^* = -d\Gamma/dw = (3E\Delta^2 Bt^3)/(8w^4)$. Therefore, the normalized local energy release rate and in particular $\phi_{\min}$ is expected to be proportional to w^{-4} and t^3. These scaling is consistent with our numerical simulations as shown in Figures 3.6(a) and (b). Displacement of the beam Δ increases slightly with fibril height and spacing. This is because increasing fibril height and spacing increase the compliance. Therefore $\phi_{\min}$ increases slightly with fibril height as seen in Figure 3.6 (c).

The effect of geometry on $\phi_{\max}$ can also be rationalized. Recall that $\phi_{\max}$ is reached when the crack tip is close to the right edge of a fibril. For the crack to heal by a length of w, it is reasonable to assume that most of the energy release to the system is due to the unloading of this fibril. Increasing the inter-fibril spacing reduces the number of fibril per unit length. As a result, each fibril bears more load and stores more elastic energy before it can unload. Specifically, a rough estimate indicates that stress on every fibril is proportional to w^2, hence the increase of elastic energy stored in each fibril is proportional to w^4. Therefore more energy will be released after the crack tip passes the right edge. As for the fact that lowering the film thickness tends to increase $\phi_{\max}$, we note that the stress field near the crack tip would be higher if the film thickness were zero, since there will be no load bearing ligament to the right of the tip

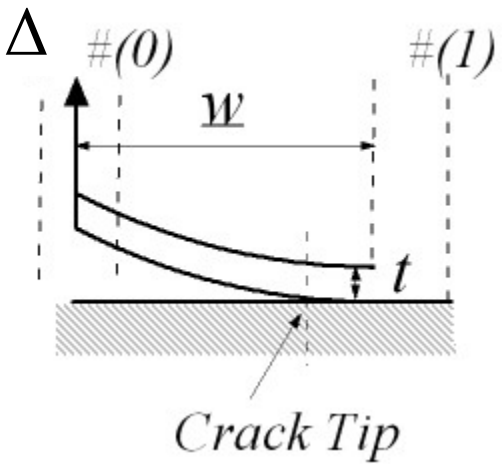

Figure 3.5 Modeling of thin film under deformation using linear elastic beam theory. Dotted line shows the location of a fibril (1, 0).

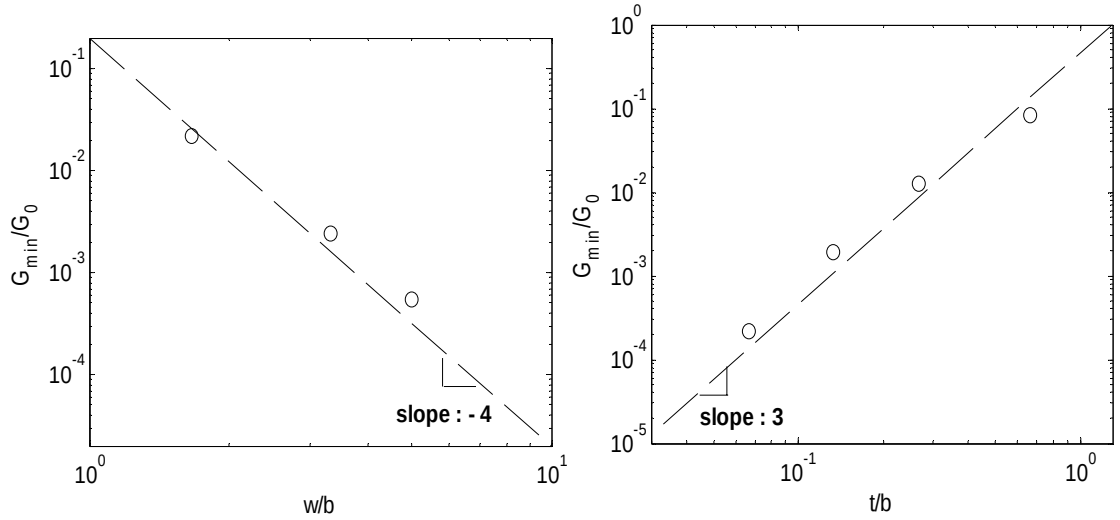

(a)

(b)

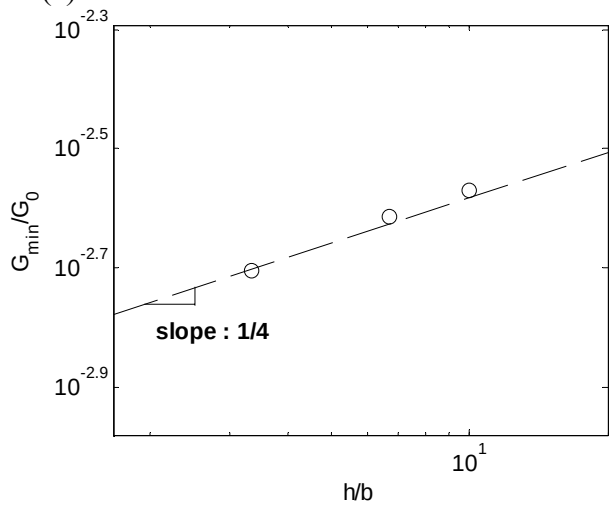

(c)

Figure 3.6 (a), (b), (c) symbols are finite element results $\phi_{\min} = G_{min}/G_0$ versus geometry parameters. (a) $\phi_{\min} = G_{min}/G_0$ versus fibril spacing, the dashed-line has a slope of -4; (b) $\phi_{\min} = G_{min}/G_0$ versus film thickness, the dashed-line has a slope of 3; and (c) $\phi_{\min} = G_{min}/G_0$ versus fibril height, the dashed-line has a slope of ¼.

as it arrives at the right edge of the fibril (see Figure 3.4(b)). The decrease of $\phi_{\max}$ with fibril height can also be accounted for by noting that the strip test is displacement controlled. For the same applied displacement, the compliance of the fibrillar interface increases with fibril height, which reduces the strain stored in the fibrils behind the crack tip and hence the energy release rate.

3.6. Discussion and Conclusion

In section 3.4, we have shown that high $\phi_{\max}$ and, more importantly, low $\phi_{\min}$ imply high pull-off strength (in this case measured by δ_{max}) and hysteresis (measured by W^{+}-W^{-}). Our results in Figure 3.4(a)-(c) indicate that large inter-fibril spacing and thin film promote the crack trapping mechanism and enhance adhesion. However, our model shows that $\phi_{\min}$ slightly increases with fibril height, which implies that hysteresis should be smaller for longer fibril. This result is supported by experiments [17]. However, an important effect is not included in the fracture model. As pointed out by Jagota and Bennison [29], when a crack passes underneath a fibril, the fibrils unloads and releases its strain energy. In a perfect elastic system, this strain energy is completely recovered. However, in real systems, only part of this energy is recovered and the rest is dissipated by vibration damping and heat. Since the stored energy in a fibril is proportional to its height it is likely that more energy is dissipated in micro arrays with longer fibrils. This is indeed observed in our system.

There are obvious limitations to our simple model where only a single row of fibrils is considered. For example, the maximum pull-off force in our model increases monotonically with fibril spacing. This is not the case in our 3D experiments where the maximum pull-off force is achieved at intermediate fibril spacing. The fact that there is an optimal effective work of adhesion in our experiments can be explained by noting that for sufficiently large spacing, the crack front can grow by sneaking through

the space between fibrils. Indeed, if the spacing is very large, most of the sneak through crack front will not sense the crack pinning effect. Furthermore, our crack trapping theory will break down for very large spacing, because when the load on the fibrils is sufficiently high, a crack-like cavity will nucleate underneath a fibril and the interface fails by the growth of this defect and this has been observed in some of our experiments [17]. Our experiments show that the effective work of adhesion is about 4 to 5 times greater than that of the flat control, whereas the plane stress model predicts an enhancement factor of $1/\phi_{\min} \cong 40$. The discrepancy can be rationalized by the fact that, the crack front in our experiments is wavy and has no translation invariance. In fact, crack growth is not even axis-symmetric; instead, the crack goes through one fibril at a time - a process which is presumably governed by local strength statistics of the interface. The location of the crack front after the jump is determined by the position of the rest of the front. Given all these limitations, it is not surprising that we overestimate the toughness. A model that will capture all the features of our indentation test will require a complicated 3D model which also takes into account the stochastic nature of crack growth.

REFERENCES

[1] Scherge M and Gorb S N 2001 *Biological Micro and Nanotribology: Nature's Solutions* (Springer-Verlag, Berlin)

[2] Rizzo N W, Gardner K H, Walls D J, Keiper-Hrynko N M, Ganzke T S and Hallahan D L 2006 *J. R. Soc. Interface* **3** 441-451

[3] Autumn K, Liang, Y A, Hsieh T S, Zesch W, Chan W PT, Kenny W, Fearing R and Full R J 2000 *Nature* **405** 681-685

[4] Eisner T and Aneshansley D J 2000 *Proc. Natl. Acad. Sci. USA* **97** 6568-6573

[5] Ruibal R and Ernst V 1965 *J. Morphology* **117** 271-294

[6] Hiller U and Morph Z 1968 *Tiere* **62** 307-362

[7] Hiller U 1976 *J. Bombay Nat. Hist. Soc.* **73** 278-282

[8] Glassmaker N J, Jagota A, Hui C-Y and Kim J 2004 *J. R. Soc. Interface* **1** 22-33

[9] Hui C-Y, Glassmaker N J, Tang T and Jagota A 2004 *J. R. Soc. Interface* **1** 35-48

[10] Yurdumakan B, Raravikar N R, Ajayan P M and Dhinojwala A 2005 *Chem. Comm* **30** 3799-3801

[11] Majidi C, Groff R E, Maeno Y, Schubert B, Baek S, Bush B, Maboudian R, Gravish, N, Wilkinson M, Autumn K and Fearing R S 2006 *Phys. Rev. Lett.* **97** 076103

[12] Peressadko A and Gorb S N 2004 *J. Adhes.* **80** 247-261

[13] Sitti M and Fearing R S 2003 *J. Adhes. Sci. Technol.* **17** 1055-1073

[14] Kim S and Sitti M 2006 *Appl. Phy. Lett.* **89** 26 261911

[15] Gorb S, Varenberg M, Peressadko A and Tuma J 2007 *J. R. Soc. Interface* **4** 271-275

[16] Glassmaker N J, Jagota A, Hui C-Y, Noderer W L and Chaudhury M K 2007 *Proc. Natl. Acad. Sci. USA* **104** 26 10786-10791.

[17] Noderer W L, Shen L, Vajpayee S, Glassmaker N J, Jagota A and Hui C-Y 2007 *Proc. R. Soc. London A* **463** 2631-2654

[18] Ge L, Sethi S, Ci L, Ajayan P M and Dhinojwala A, 2007 *Proc. Natl. Acad. Sci. USA* **104** 26 10792-10795

[19] Jagota A, Hui C-Y, Glassmaker N J and Tang T 2007 *MRS Bulletin* **32** 492-495.

[20] B. Aksak, M. Sitti, A. Casell, J. Li, M. Meyyappan, and P. Callen, 2007 Applied Physics Letters, vol. **91**, no. 061906

[21] L. Ge, S. Sethi, L. Ci, P.M., and A. Dhinojwala, 2007, *Proc. Natl. Acad. Sci.* USA **104,** 10 792-10 795. (doi:10.1073/pnas.0703505104).

[22] Y. Zhao, T. Tong, L. Dezeit, A. Kashani, M. Meyyapan, and A. Majumdar, 2006, *J. of Vacuum Science B*, **24** 331-335, no. 1, 2006.

[23] Crosby A J, Hageman M and Duncan A 2005 *Langmuir* **21** 11738-11743

[24] Arzt E, Gorb S and Spolenak R 2003 *Proc. Nat. Acad. Sci* **100** 19 10603-10606

[25] Yurdumakan B, Raravikar N R, Ajayan P M and Dhinojwala A 2005 *Chem. Commun*. 3799-3801

[26] Anderson T L 1995 *Fracture Mechanics: Fundamentals and Applications* (CRC Pr I Llc)

[27] Thomson R, Hsieh C and Rana V 1971 *J. Appl. Phys.* **42** 8 3154-3160

[28] Rice J 1978 *J. Mech. Phys. Solids* **26** 61-78

[29] Jagota, A and Bennison, S.J. 2002 *Integr. Comp. Biol.* **42,** 1140-1145.

[30] ABAQUS *Users Manual: Theory Manual Version 6.5*

[31] Parks D M 1977 *Comput. Methods Appl. Mech. Eng,* **12** 353–364

[32] Shih C F, Moran B and Nakamura T 1986 *Int J. Fract.* **30** 79–102

APPENDIX 3

The FEM model is implemented using ABQAUS 6.5. To simulate the infinite strip, we use a finite strip with width to height ratio = 65:1. A schematic of the geometry is shown in figure A1. To reduce simulation time, we only put a finite number of fibrils 2*N* centered at the crack tip (see figure A3.1). To determine the appropriate number of fibrils *2N* for this simplification, we carried out a convergence study with *2N* = 10, 20, 40 and 80. Simulation shows that the solution converges at *N* = 20.

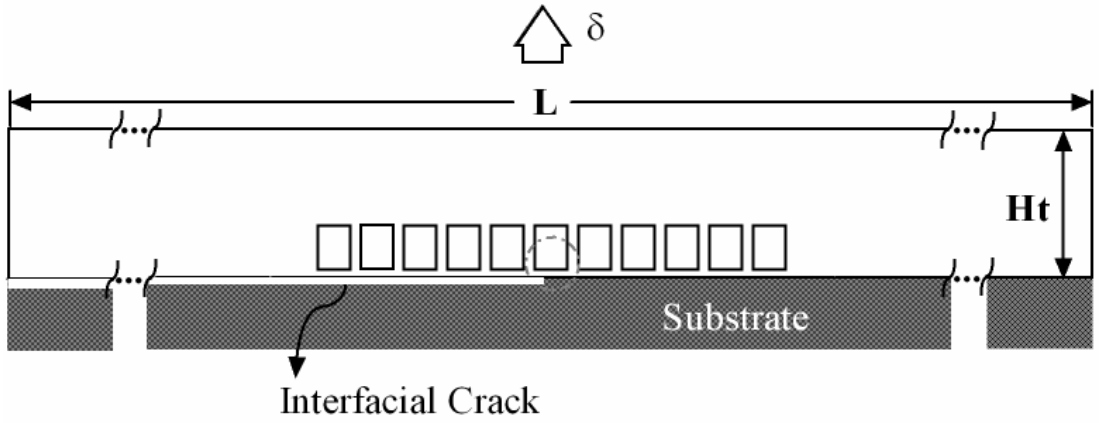

Figure A3.1 schematic geometry of FEM model. H_t/L = 1/65. There are *2N* fibrils. Half of them are left of the crack tip. These fibrils are free to be lifted under load. The rest of the fibrils are on the right of the crack tip. These fibrils are constrained since the thin film underneath is assumed to be perfectly bonded to the substrate.

Eight node plane stress element with reduced integration (CPS8R) is chosen for this analysis. The mesh is highly non-uniform. Specifically, the domain is divided into 6 regions. Each region has different mesh density. For the regions far away from the crack tip, the results are not sensitive to mesh density. Therefore rough mesh is used in these regions. The most refined mesh is assigned to the region closest to the

crack front since the energy release rate is strongly affected by mesh density in this region. The number of elements used to mesh the thin plate in the crack tip region is determined by a convergence study. Specifically, we increase the number of elements in the thickness direction until the energy release rate converges. We found that 8 elements are sufficient to guarantee convergence. In the simulations, 10 elements are used to mesh the plate in the thickness direction. The simulation is carried out with Young's modulus E=3MPa and Poisson's ratio v=0.499.

A uniform vertical displacement is assigned to all nodes on the top surface of the strip. The crack is simulated by freeing all the surface nodes to the left of the crack tip. The surface nodes to the right of the crack tip are fixed; no movement is allowed in any direction. Crack advance was carried out by releasing the node ahead of the crack tip.

For each crack position, one analysis is carried out to evaluate the energy release rate at the crack tip. In ABAQUS [30], the energy release rate is evaluated by J-integral using virtual crack extension/domain integral methods. Details of this method can be found in (Parks [31] and Shih *et al* [32]).

CHAPTER 4

STRONGLY ENHANCED STATIC FRICTION USING A FILM-TERMINATED FIBRILLAR INTERFACE[2]

4.1 Abstract

We examine the behavior under shear of a bio-inspired fibrillar interface that consists of poly(dimethlysiloxane) micro-posts terminated by a thin film. These structures demonstrate significantly enhanced adhesion due to a crack trapping mechanism. We study the response of this structure to shear displacement relative to a spherical indenter placed on its surface under fixed normal force. The shear force required to initiate sliding between the indenter and the sample, its static friction, is strongly enhanced compared to a flat control, and increases with inter-fibril spacing. Examination of the contact region reveals that its area changes with applied shear and that static friction is controlled by a mechanical instability. The shear force resisting steady sliding, surprisingly, is independent of fibril spacing and is nearly the same as for the flat unstructured control samples. We interpret dynamic friction to result from the action of Schallamach-like waves. Our results show that the film-terminated architecture can be used to design an interface with significantly enhanced static friction without altering its sliding frictional resistance.

4.2 Introduction

Fibrillar surfaces are commonly found on the contact surfaces of the feet of many lizards and insects [1-7]. These surfaces provide desirable adhesion and friction

[2] Reproduced from L. Shen, N. Glassmaker, A. Jagota, C-Y. Hui, Soft Matter, **4** (2008) 618-625, with permission from Royal Society of Chemistry (RSC).

properties so that the animal can cling and climb. Recent studies have shown that fibrillar surfaces are more compliant than flat surfaces of the same material, which allows better adhesion against rough surfaces [8-10]. Moreover, due to the small size and compliant nature of the contacting tips or 'spatulas' of biological setae, fibrillar surfaces are able to attain stronger adhesion than flat surfaces of the same material [3,11]. Fibrillar surfaces can also reduce adhesion between liquid droplets and solid surfaces and promotes "superhydrophobicity" [12, 13]. With these biological systems as motivation, several groups have attempted to mimic the biological architecture in order to attain enhanced adhesion [10, 14-20]. Several groups have recently demonstrated significant enhancements in adhesion using fibrillar structures [19-24].

Most of the reported work on bio-inspired fibrillar surfaces has focused on how such surfaces make contact with smooth substrates and separate under normal loads. On the other hand, experiments on the gecko have demonstrated that the maximum shear force a seta can support is about six times greater than the normal pull-off force [3] and other studies of relative performance of species have also been conducted under shear [25]. For this reason, and because performance under shear of any new material should be established, it is important to study how these interfaces respond to shear. However, there are very few studies on this problem [16, 23, 26, 27].

In this paper we study the response under shear loading of a two-level structure consisting of an array of micro-posts connected at the terminal end by a thin, flexible film. This structure has been shown to significantly improve adhesion compared to a flat unstructured control [28, 21]. Adhesion enhancement is due to crack trapping because of spatial variation of energy available to drive an interface crack as it moves between fibrils [22]. A schematic illustrating the crack trapping mechanism is shown in Figure 4.1 Since fibrillar structures are designed to be good adhesives, it is natural to ask whether there is a connection between adhesion and friction. For smooth

interfaces between a soft elastic solid and a hard spherical surface, one of the first attempts to relate static friction to adhesion is due to Savkoor and Briggs [29]. Using a contact mechanics solution due to Mindlin [30, 31], they extended the Johnson-Kendall-Roberts (JKR) theory [32, 33] by taking into account the effect of shear force on the adhesive contact of a smooth rubber sphere on a flat glass plate. Treating the air gap outside the contact region as an external crack, they computed the energy release rate due to a monotonically increasing shear load assuming that no microslip occurs on the interface. For a fixed normal load, they found that increasing the applied shear force decreases the contact area. In addition, they predicted that at a critical shear force the system experiences a mechanical instability after which sliding commences. Later, Johnson [34] extended this result by including the contribution due to friction in the critical energy release rate. His solution allows for microslip on the interface.

As pointed out by Savkoor and Briggs [29], the interface does not necessarily fail by the propagation of a shear crack at the critical shear load. They pointed out that, for a soft material in contact with a hard substrate, sliding can be caused by surface instability in the soft material in the form of Schallamach waves [35]. It is well known that [36, 37] a sudden drop of shear force occurs when a Schallamach waves begins to appear in the contact region. These waves allow relative motion between the two adhered contact surfaces without relative slip in the region between two successive waves.

The goal of this work is to study the adhesion and friction behavior of our film-terminated fibrillar structure. We begin by presenting experimental methods in Section 4.3. In Section 4.4 we report measurements of the effective work of adhesion using a cantilever beam fracture test. Using this test, we determine how the effective work of

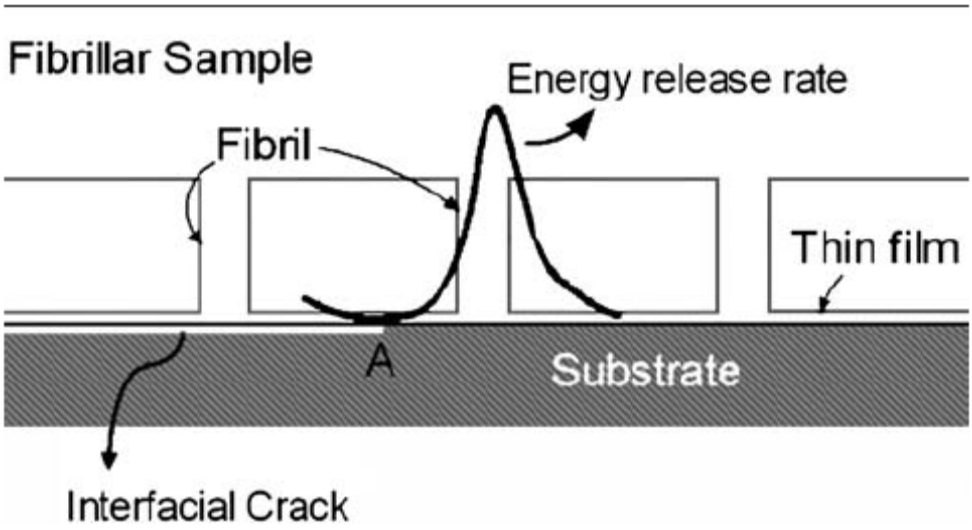

Figure 4.1 Illustration of crack trapping in our film terminated fibrillar structure. The energy release rate depends on the crack tip position and is typically small when the tip is between fibrils. Numerical simulations [22] have shown that the minimum energy release rate occurs when the crack is just at the left of the edge of a fibril, as indicated by (A) in the Figure. Thus, the crack tip will be trapped in this position (A) until a sufficiently large load is applied. Since the energy release rate is increasing rapidly after the trapped position, unstable crack growth will occur once the crack tip moves, leading to dissipation.

adhesion varies with spacing between fibrils. In section 4.5 we present experimental results of shear experiments, and their interpretation. This is followed by discussion and summary of results in section 4.6.

4.3 Experimental Methods

We present results on a series of film-terminated fibrillar samples. Figure 4.2 shows a scanning electron micrograph of the cross-section of a typical sample. The samples were fabricated using poly(dimethylsiloxane) (PDMS, Sylgard 184, Dow Corning) following the procedure of [21, 22]. Briefly, a fibrillar array is created by molding the PDMS precursor into a silicon master containing an array of square holes. Holes were created by photolithography and a deep reactive ion etching process and were arranged in a square pattern. The liquid polymer precursor is cured after being poured into the holes, and subsequently peeled off. A terminal film is attached to the ends of the posts by first spinning liquid PDMS onto a hydrophobic substrate. The array of posts is placed on the liquid film and the assembly is cured in place. A glass cover slip is attached to the backing and the entire sample is removed manually from the substrate. We also fabricate flat control samples; the thin film is adhered onto them in the same fashion as for the fibrillar samples. For the results reported in this paper, all samples had square fibrils with cross-section area 10 x 10 μm^2, height 30 μm, backing thickness 650μm, and film thickness of about 4 μm. The inter-fibril spacing, denoted by w, was varied from 20 to 135μm.

A cantilever beam (CB) experiment is used to obtain the effective work of adhesion of the fibrillar interface (see Figure 4.3) as described previously [21]. The cantilever beam consists of the fibrillar sample bonded to a glass cover slip. The fibrillar surface is brought into contact with a Si wafer whose surface is covered by a

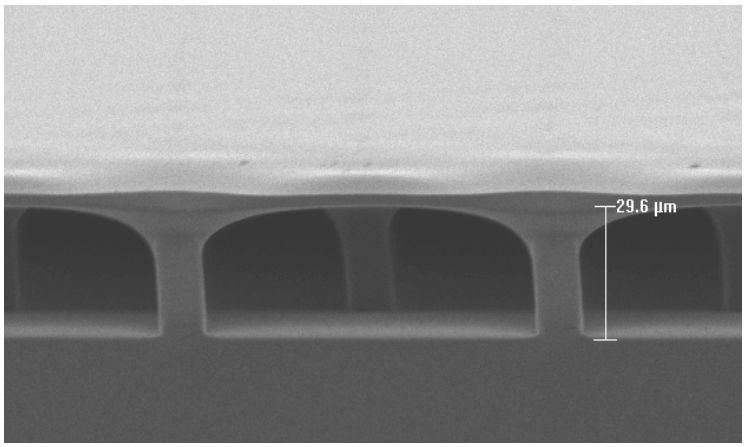

Figure 4.2 Scanning electron micrograph of a synthetic fibrillar array with a terminal thin film. Fibrils are arranged in a square pattern. Their height is about 30 μm. The nearest neighbor distance between fibrils is about 65 μm. Each fibril is square in cross-section with sides nominally 10 μm wide. The terminal film is about 4 μm thick.

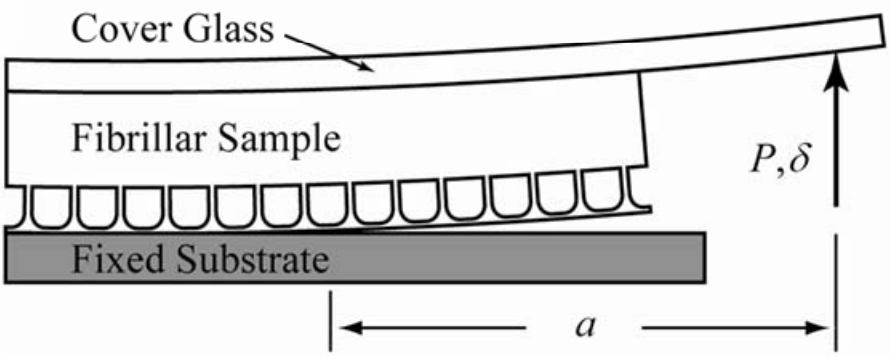

Figure 4.3 Schematic drawing of the cantilever beam (CB) experiment for measurement of the effective work of adhesion.

hydrophobic self assembled monolayer. To obtain consistent adhesion measurements and to reduce interfacial rate effects, a self-assembled monolayer (SAM) of the molecule n-hexadecyltrichlorosilane was deposited on the silicon or glass surface following the procedure given in [21, 22]. The Si wafer is fixed in place and the glass slide is pushed upward at a point near its edge at a constant rate of 5 $\mu m/s$. The load at this point is recorded. The position of the crack front is recorded using a video camera above the sample. By recording the load and displacement as well as the crack length, the energy release rate of the specimen during crack advance can be determined following the procedure given in [21]. The effective work of adhesion is the energy release rate during crack advance.

The experimental set-up used to study the behavior of the interface under shear is shown schematically in Figure 4.4. The sample is placed on an inverted optical microscope and a spherical glass indenter with a 2mm radius is placed on the fibrillar surface. As described later, the static friction force was often large enough to damage our samples significantly. To avoid these conditions, the indenter is coated with a monolayer using the procedure described in [21]. This surface treatment significantly lowers the shear force between the indenter and the PDMS sample. The fixed normal force, P, is applied by means of a mechanical balance. As an independent check of the normal load setting, we indent a flat control sample before every experiment on a fibrillar sample and adjust the balance, if needed, to provide a fixed contact area. The actual value of normal force corresponding to this contact area is obtained by performing an independent indentation experiment as described in [22]. Specifically, we use the recorded force and contact area in this indentation test to set the normal force in the shear experiments. The shear force is applied by translating the glass slide at a constant rate of 30 μm/s. The translation is implemented by a motor (Newport ESP MFA-CC) and motion controller (Newport ESP300). All results

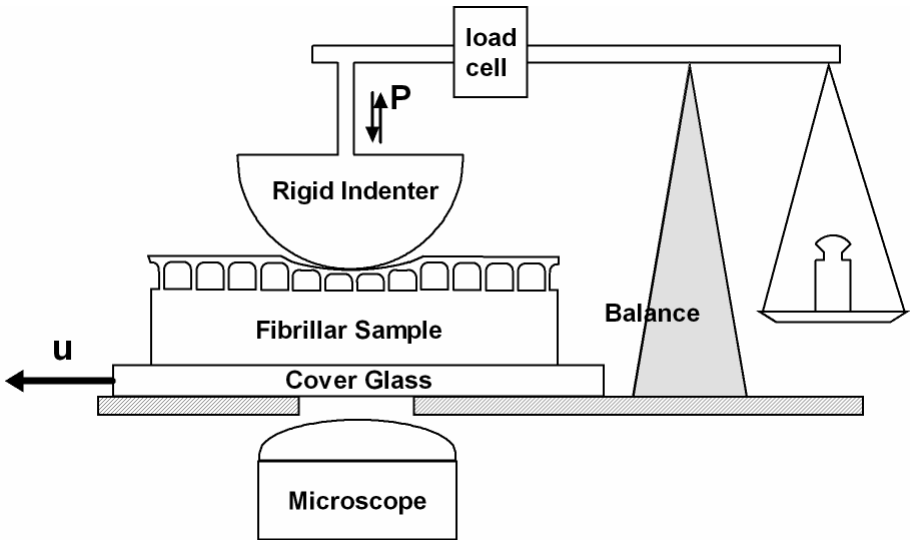

Figure 4.4 A glass indenter is placed on the fibrillar surface under fixed normal force (*P*) (applied via a mechanical balance). The sample is translated at a fixed velocity and the shear force is measured by the load cell. Deformation near the contact region is recorded by means of an inverted optical microscope.

in this paper, except those presented in Figures 4.10 and 4.11, where a lower rate (du/dt = 1μm/s) is used to obtain better images, are obtained using this rate. The shear force is measured by a strain gauge-based load cell (Honeywell Precision Miniature Load Cell Model 31-50) in line with the balance arm. Deformation of the contact region is recorded by means of an optical microscope.

4.4 Effective works of adhesion

Figure 4.5 shows the effective work of adhesion of the fibrillar interface measured in the CB experiment for different values of minimum inter-fibril spacing. Also shown are the effective works of adhesion for the flat control samples. In the fibrillar samples, there is a systematic increase in effective work of adhesion with increasing fibril spacing. In our previous indentation experiments on a different set of samples, we found that adhesion hysteresis reaches a maximum at an intermediate value of inter-fibril spacing [22]. Results shown in Figure 4.5, however, indicate that, over a wider range of inter-fibril spacing, the work of adhesion increases monotonically. Data on the sample with the largest inter-fibril spacing should be viewed with caution since the effective work of adhesion of its corresponding control is anomalously high. We will later use these results to help interpret measurements of the contact under shear.

4.5 Static and Dynamic Friction

Figure 4.6 shows typical measurements of shear force as a function of shear displacement for three different fibril spacing and a flat control sample. The normal compressive load applied on these samples is nominally zero (*i.e.,* much smaller than other relevant forces and measured to be approximately $0.22mN$). With increasing relative shear between the indenter and the sample, the shear force first increases to a

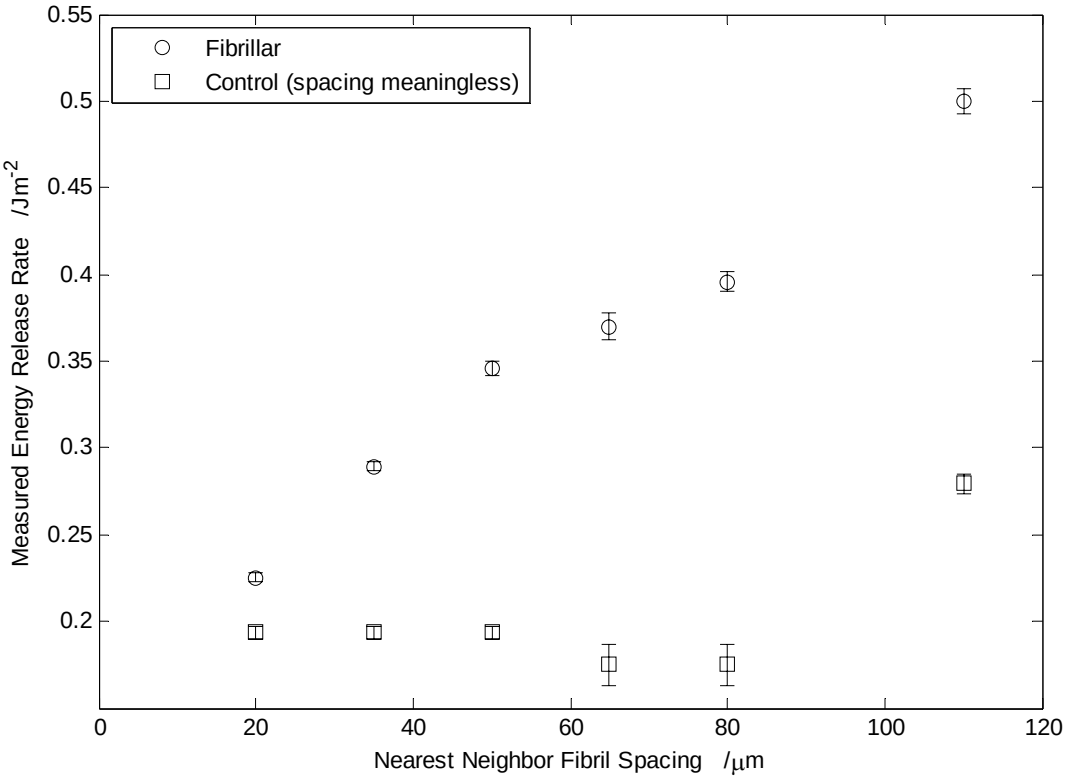

Figure 4.5 Measured effective work of adhesion of film-terminated fibrillar samples as a function of inter-fibril spacing.

peak value (stage 1). Beyond the peak, it decreases rapidly (stage 2), and then remains nearly constant (stage 3). Visual inspection of the contact region in stage 1 (discussed in more detail later) reveals that it changes in shape and size, but there is no macroscopic sliding between the indenter and the sample. In stage 3, the indenter slides steadily on the sample. As will be seen later, the peak in shear force coincides with an unstable release of the shear strain in the contact region between the indenter and the sample. For the flat control sample, when a peak occurs, its value is only slightly larger than the steady sliding friction force. In other instances, for flat control samples, the transition to sliding is not accompanied by a peak in shear force. In contrast, the peak force is much larger than the steady sliding force for the fibrillar samples. Like the effective work of adhesion measured in the CB experiments (Figure 4.5), the peak force increases with increasing inter-fibril spacing, suggesting a connection between static friction and adhesion.

In Figure 4.6 we plot the peak shear force as a function of fibril spacing. The shear force has been normalized by the average peak force for the corresponding flat control samples. Five separate tests were run on each sample to obtain the average shear force; error-bars indicate the standard deviation of the tests. These data show that there is a strong enhancement of the static friction force in fibrillar samples compared to the flat controls (nearly an order of magnitude in this set of experiments). In other data at higher compressive loads and loading rates we have measured enhancement well in excess of a factor of ten (data not shown here because large shear forces resulted in damage to those samples). The maximum static friction force is for the samples with nominal inter-fibril spacing of 80 μm. In the experiments on samples with larger inter-fibril spacing we observed copious sub-surface damage associated with fracture of the fibrils. This suggests that it may be possible to increase the range of fibril spacing over which static friction increases by strengthening the fibrils.

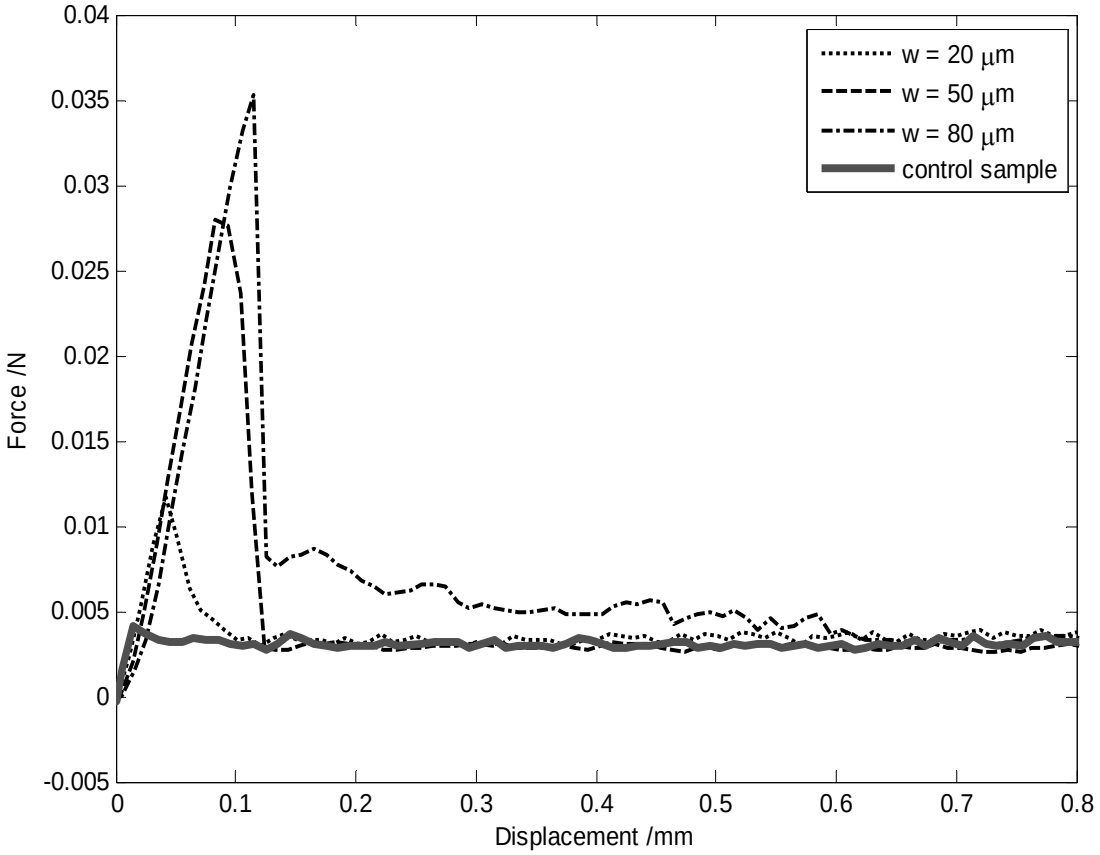

Figure 4.6 Shear force as a function of shear displacement for fibrillar samples with spacing of 20, 50 and 80 μm, and for a flat control sample. Samples are indented by a glass sphere with a radius of 2mm.

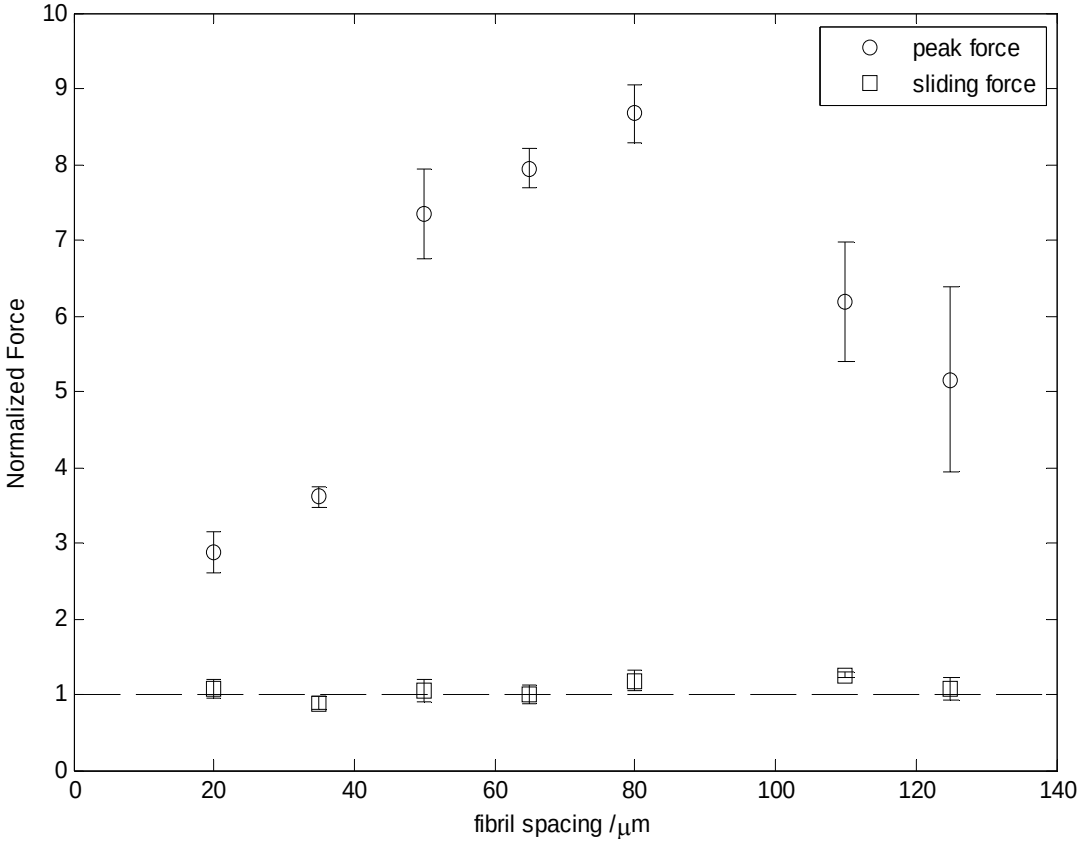

Figure 4.7 Static and sliding friction force normalized by its value for a flat control for samples with different inter-fibril spacing.

The data on dynamic friction forces is strikingly different. Surprisingly, the sliding friction force is found to be substantially unaffected by fibril spacing *and* is identical to that for the flat control sample, within experimental error. Therefore, our architecture provides a method by which one may significantly enhance the static friction of an interface without altering its sliding frictional resistance.

To understand the mechanisms underlying the static and sliding response of our material, we examine micrographs of the contact region. Figure 4.8 shows a typical force-displacement curve for a flat control sample. A sequence of points (a, b, c, etc.) is marked on this curve. Images of the contact region corresponding to these points are shown in Figure 4.9. For this flat control sample, we observe a small initial peak in the shear force. Micrographs in Figure 4.8 show the effect of shear loading on the contact region. A comparison of Figure 4.9(a) & (b) reveals that the effect of shear load is to reduce the contact area. This can be explained using the theory of Savkoor and Briggs [29], as described in the Introduction. We will examine this more quantitatively in the discussion section. In the sliding regime, Figure 4.9(c-l) the contact area fluctuates between two states. In the first state, the shape appears to be approximately elliptical, with the long axis perpendicular to the shear direction. In the second state, the shape is approximately circular. The contact area in the second state is always larger than in the first state. Both contact areas are smaller than the contact area at zero shear (t =0, Figure 4.9(a)) by 25~46%. The transformation from the first stage to the second stage is accomplished by an apparent "addition" of more contact area at the trailing edge. Details of shape fluctuation can be observed in a video available as supplementary material.[2] This shape fluctuation is similar to that reported by Rand and Crosby [38]. In experiments where they slid a spherical indenter on a PDMS substrate they reported a similar phenomenon, except in their case the transformation occurs at the leading edge of contact. Their interpretation is that sliding

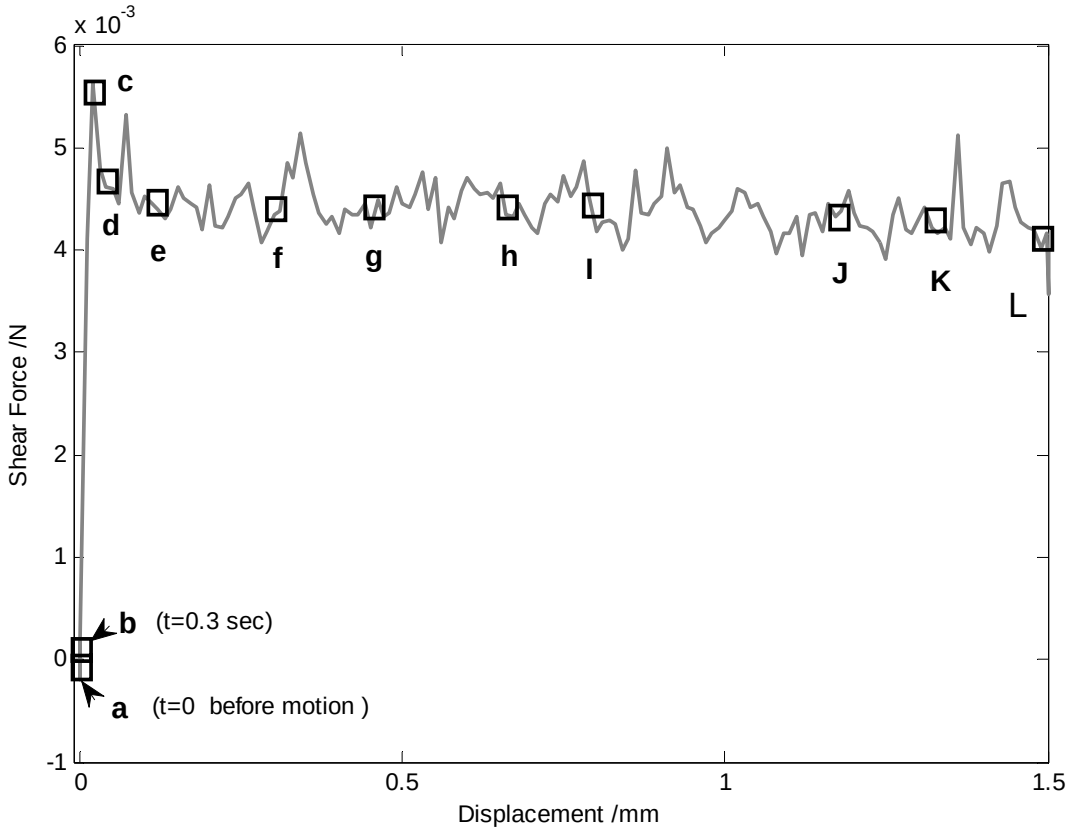

Figure 4.8 A typical force-displacement trace for flat control samples. Labels (a,b,c, etc.) mark points for which we present micrographs of the contact region in Figure 4.9.

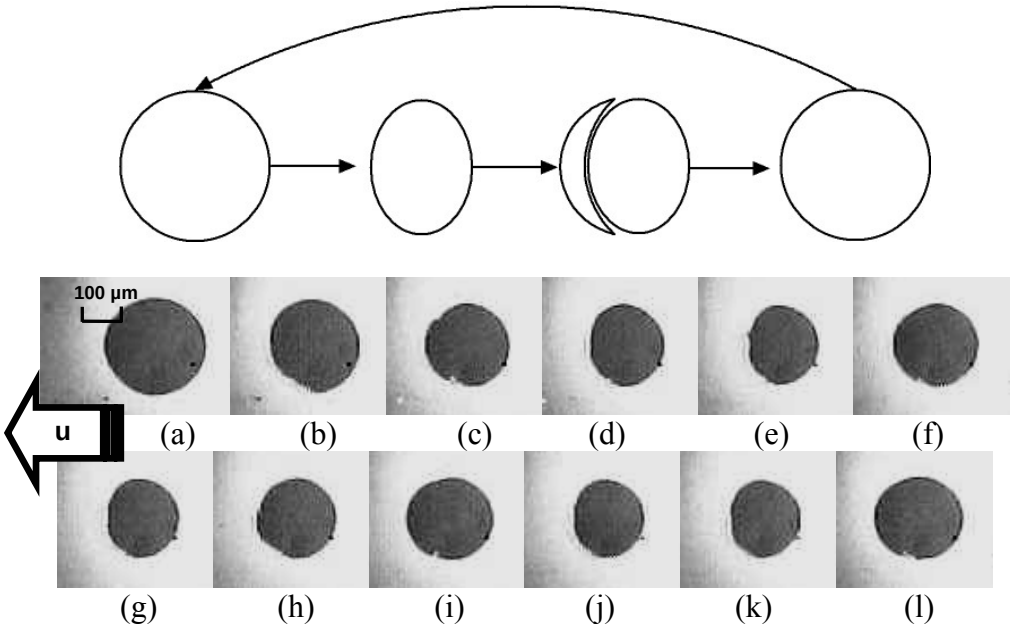

Figure 4.9 Series of images of the contact region for a flat control sample under shear (Figure 4.8). (a) Initial contact (b) reduction in contact area on application of shear, (c-l) under sliding conditions there are significant fluctuations in force that are accompanied by shape fluctuations. (Fluctuations in the shear force are significantly larger than background noise.)

is accommodated by the propagation of a Schallamach wave [35]-[26]. More recently, Chaudhury and Kim [39] have observed the propagation of bubbles at the interface while sliding a rectangular glass block on the surface of PDMS. They reported that sliding is accommodated by the propagation of bubbles formed at the *trailing* edge, as in our experiments. Although in our flat control samples such bubbles are not directly observed, the shape fluctuation suggested that sliding is accommodated by shear-relaxing waves that initiate at the trailing edge and propagate towards the leading edge.

The force-displacement curve for a fibrillar sample at a shear displacement rate of $du/dt = 1\mu$m/s is shown in Figure 4.10. As in the cases shown in Figure 4.6, the shear force increases with shear displacement until it reaches a critical value (at the point marked 'E'), after which it decreases rapidly to a nearly constant value. A set of images corresponding to different points on the force-displacement curve is shown in Figure 4.11; the direction of motion of the substrate (with the indenter held fixed) is indicated by the arrow. The initial contact at zero shear is approximately circular, slightly facetted due to the square pattern of the fibrils. Because these fibrillar samples exhibit significant adhesion hysteresis, one must take care to establish the initial state of the contact reproducibly. During loading, the applied force is first made to exceed the desired preload before being reduced to achieve the final contact. This procedure ensures that the initial state of the contact is always governed by the effective work of adhesion of the interface on crack opening.

Immediately on application of the shear load, the contact shape changes (see Figure 4.11 (b)). Due to applied shear, the top of a typical fibril is displaced relative to the bottom, in the direction of the applied shear. The top ends of the fibrils, where the joint between fibrils and the film is rounded (see Figure 4.2), appear as fuzzy gray circles in these images, whereas the bottom ends of the fibrils appear as smaller dark squares. This difference allows us to determine the relative deflection of each fibril.

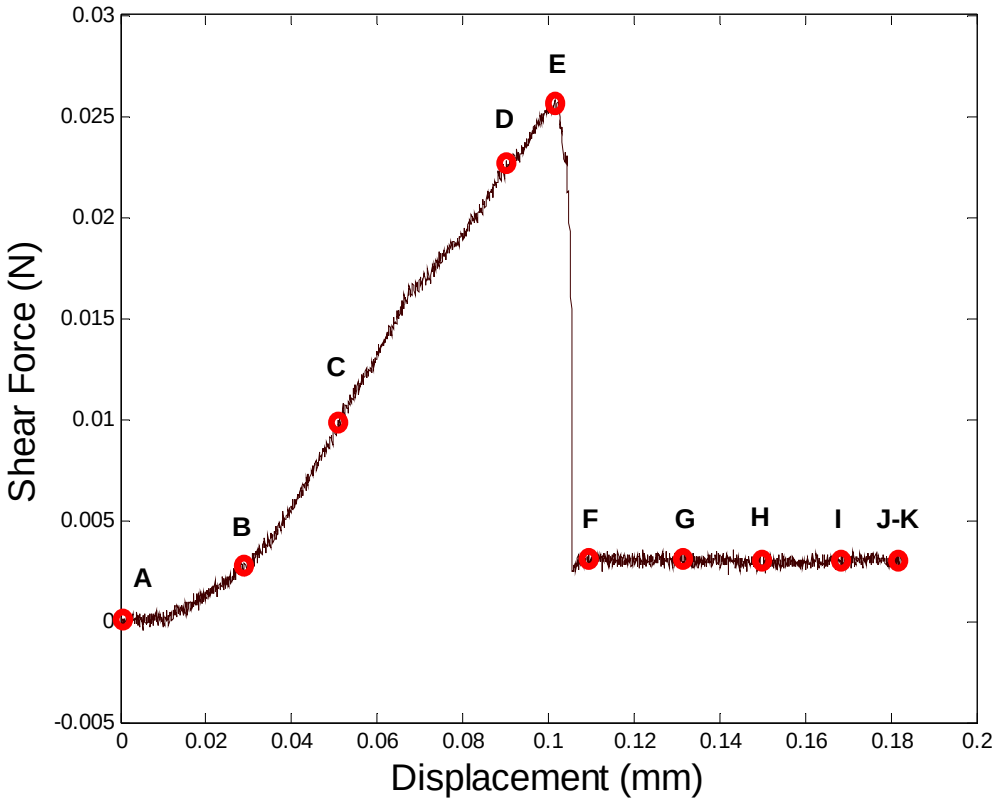

Figure 4.10 Force-displacement trace for a fibrillar sample.

Figure 4.11 Series of images for the fibrillar sample under shear. Figure labels correspond to points on the plot shown in Figure 4.10. Also shown are contour plots of shear displacement across the fibrillar layer.

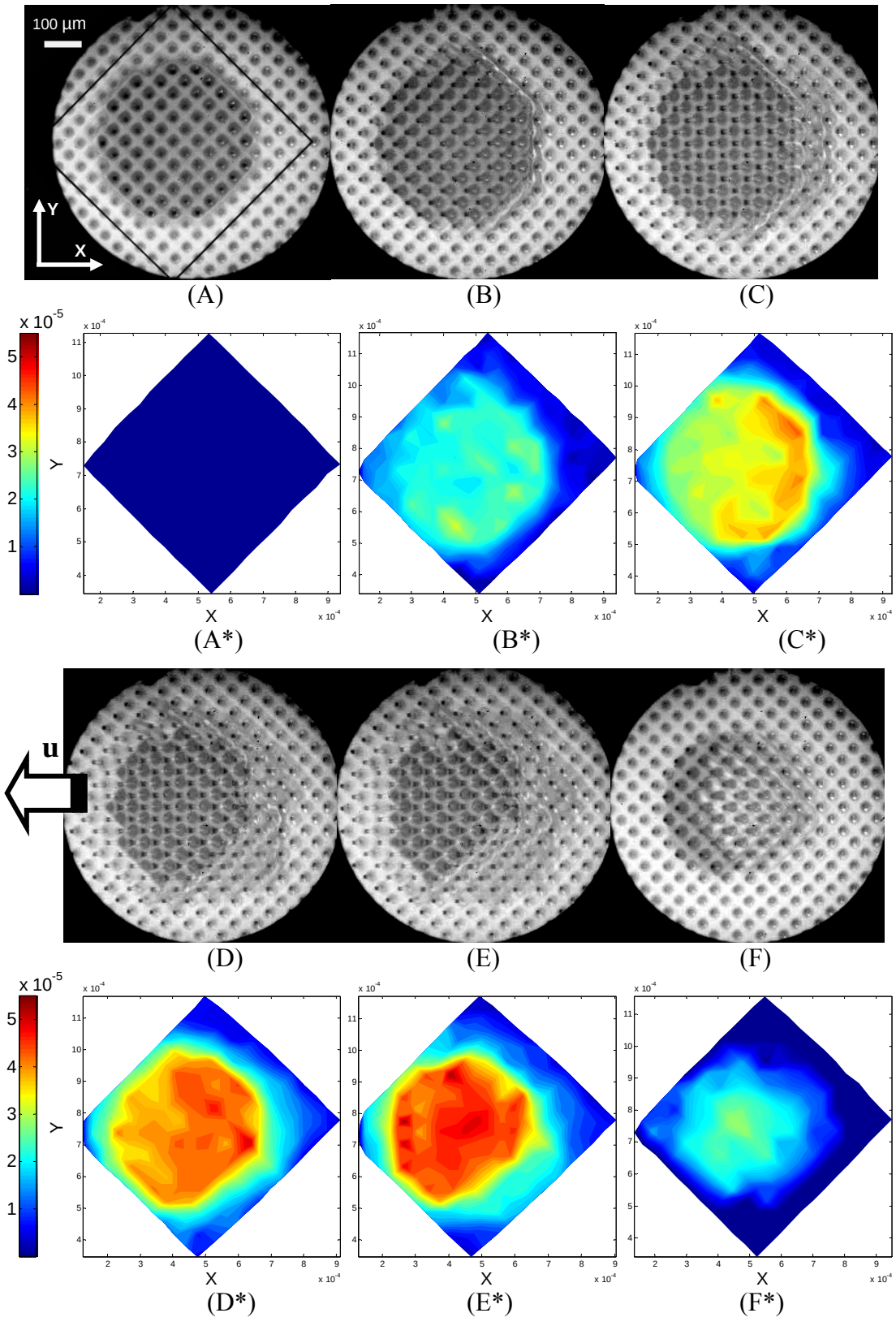
100 µm
Y
X
(A)
(B)
(C)
x 10-5
5
4
3
2
1
Y
X
(A*)
(B*)
(C*)
u
(D)
(E)
(F)
(D*)
(E*)
(F*)

Figure 4.11 Continued

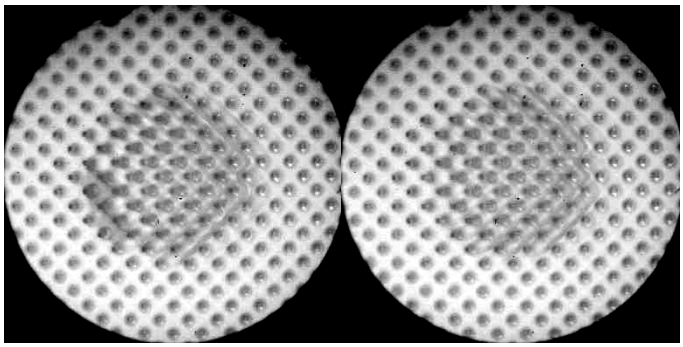

(G) (H)

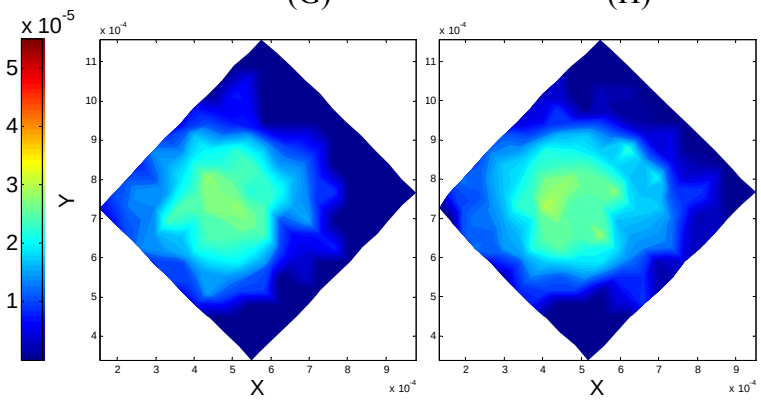

(G*) (H*)

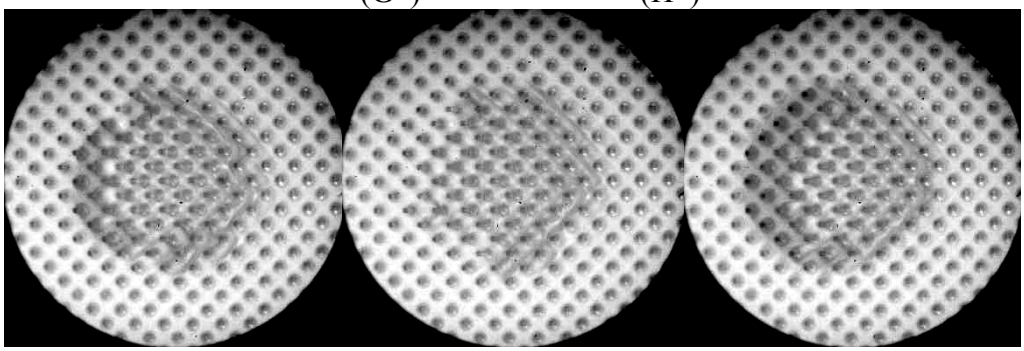

(I) (J) (K)

For example, in the first image (A) the fuzzy regions symmetrically overlap their respective dark squares, since there is no applied shear. We have measured shear deformation of each fibril inside the square region marked by lines in Figure 4.11(A). The deformation of the fibrils within this region that circumscribes the contact is shown in contour plots below the corresponding micrographs (A-H). Shear displacement is plotted in Figure 4.12 as a function of distance along the horizontal diagonal of the square for cases (A,B,E, and F).

To interpret the images before sliding ensues (Figure 4.11 A-E), consider a schematic drawing of the contact region in Figure 4.13. Three regions can be identified. In region I there is intimate and complete contact. In this region, the fibrils deform more or less uniformly and, prior to the onset of sliding, can be subjected to large deformation (in some cases the relative shear displacement can exceed the height of a fibril). In micrograph Figure 4.11A, the entire contact comprises Region I. With increasing shear, this region (darker shading in Figure 4.11 B-E) appears first to expand and then to reduce in size. The approximate uniformity of the fibril deformation in this region can be observed by examining the contour plots (B* to E*). (This is shown more explicitly in Figure 4.12.) We define Region II to be the material to the left of the trailing edge of the contact. The boundary between Regions II and I, the trailing edge of the contact, can be viewed as the front of an interface crack. Here, the crack is intermittently trapped by the fibrils (see Figure 4.12 D, E). Thus, we expect that the increase in effective work of adhesion operates by the same crack trapping mechanism as found under normal separation of the interface. Region II can be interpret as the wake of the crack. In this region the film is in tension, and this tension is transferred to the substrate over some characteristic distance (see also Figure 4.12). (A simple shear-lag model would predict exponential decay of shear displacement with distance from the contact edge.) Note that in region II, there is no

contact between the indenter and the film. Region III lies ahead of the leading edge of Region I. Here the film is under compression but retains at least partial contact with the indenter. Partial contact can be identified in the micrographs as regions with a shade of gray intermediate between Region I and II. As seen by Figure 4.11 (E) & (F), the transition from a static to a sliding contact corresponds to transformation of the contact from region I into region III, supporting our suggestion that in region III there is always at least partial contact with the indenter. We interpret the undulating white lines between fibrils in this region to be local regions that have lost contact due to local buckling of the film. (See Figure 4.11 (B) and (C) for the inception of buckling). This geometry comprising of partial contact is reminiscent of the bubbles and Schallamach waves seen in previous experiments [35-39].

The transition from the peak shear load to steady sliding occurs between states (E) and (F). The change in near-surface shear can be seen in the corresponding contour plots (E* and F*) and in Figure 4.11. Note that the shear displacement in the contact drops dramatically from E* to F*. This suggests strongly that the static friction peak is associated with a mechanical instability. In the sliding mode, although the top of the fibrils are still under shear, the interfacial regions between them exhibit the same contrast as the non-contact regions, indicating that these regions are detached from the indenter. This observation suggests that the crack trapping mechanism that enhances adhesion when contact is intimate can no longer operate in the sliding regime. Images F-J show that the shear displacement in the contact region does not change substantially during sliding. There is some oscillation in the shape of the contact as new buckles form ahead of it. Images K shows that once motion of the sample is halted, the contact gradually recover to partial intimate contact at the trailing half of the contact. Along with this, we see a time-dependent return of the static friction peak. This feature of the response of our material remains to be studied in detail. A

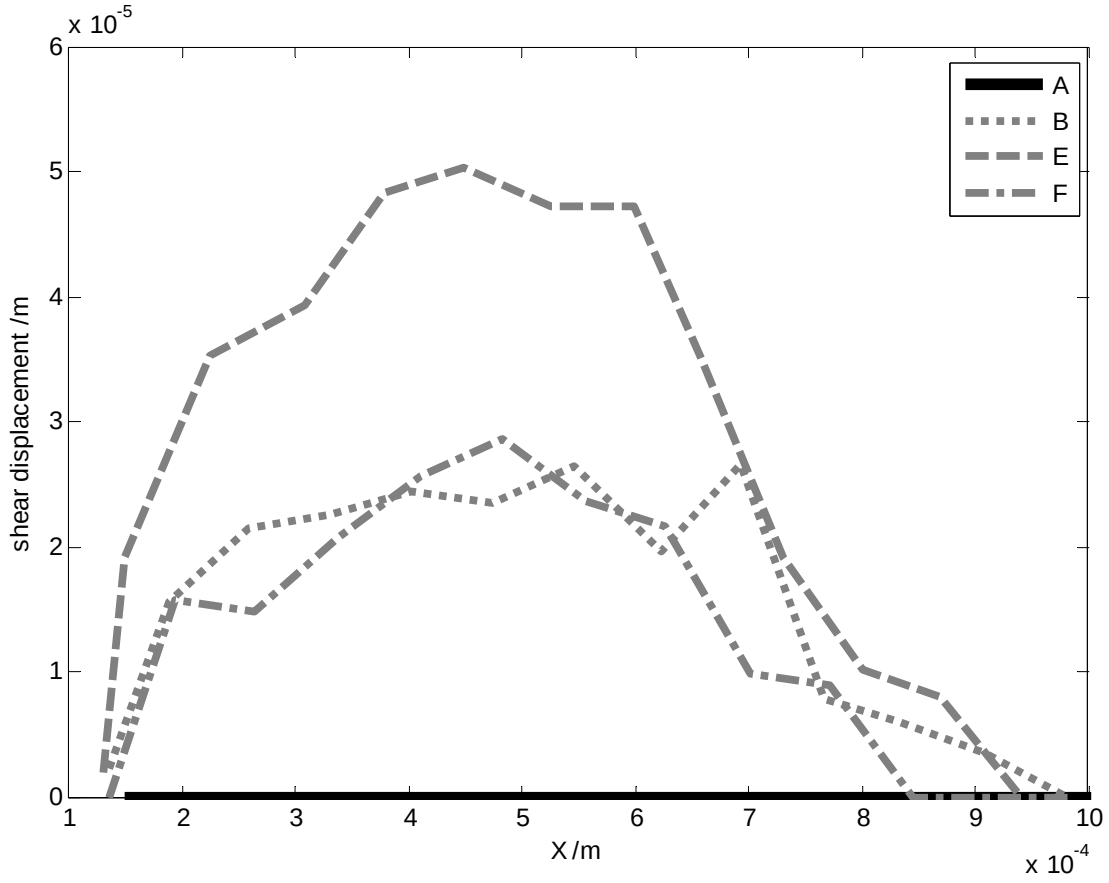

Figure 4.12 Shear displacement as a function of distance along the horizontal diagonal of the square drawn in Figure 4.11(A).

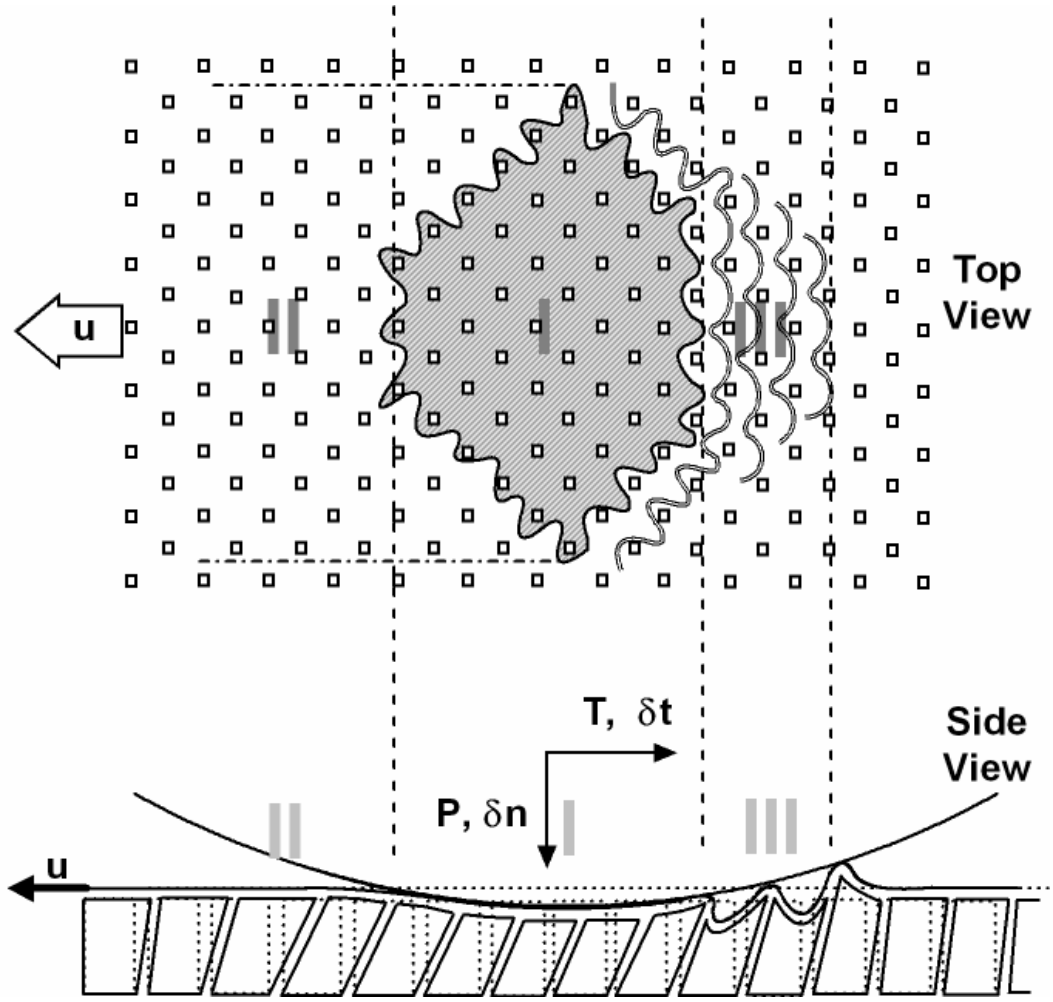

Figure 4.13 Schematic drawing of the contact region before the instability. The trailing edge is the boundary between II and I. The direction of motion of the sample relative to the indenter is to the left.

video of the sliding experiment (fibril spacing = 50μm) is included as supplementary material.[2]

4.6 Discussion and Summary

Two main characteristics of the shear response of our fibrillar samples have emerged. The first is the strong enhancement of the static friction force and the second is the fact that the dynamic friction force remains unchanged with change in geometry. To develop a better understanding of the mechanisms underlying these observations, it is useful first to consider the behavior of the flat control samples. Our results for the flat control samples reveal that the contact area is largest when the shear force is zero, consistent with the theory of Savkoor & Briggs (SB) [29]. It should be noted that the analysis of SB assumes that there is no sliding. According to SB, as long as the indenter does not slide, the shear force T is related to the shear displacement of the indenter, δ, by

$$\delta = \frac{9T}{16Ea} \tag{4.1}$$

where a is the contact radius and E is the Young's modulus of PDMS, which is assumed to be incompressible. Thus, the shear compliance of our flat control sample before sliding occurs is *9/(16Ea)*. The Young's modulus of PDMS was determined to be 2.9 MPa independently using a normal indentation test. Figure 4.14 plots the quantity 16*Eδa/9T measured* in stage 1. According to (4.1), this should be a constant with value of unity, independent of the amount of applied shear displacement. After an initial transient, this quantity in our experiment does indeed attain a constant value (≈ 1.5), showing that contact radius is inversely related to increasing shear displacement, as predicted by SB.

For the fibrillar samples, in contrast, the contact area initially increases with shear load. Since increasing the shear load increases the energy available for contact

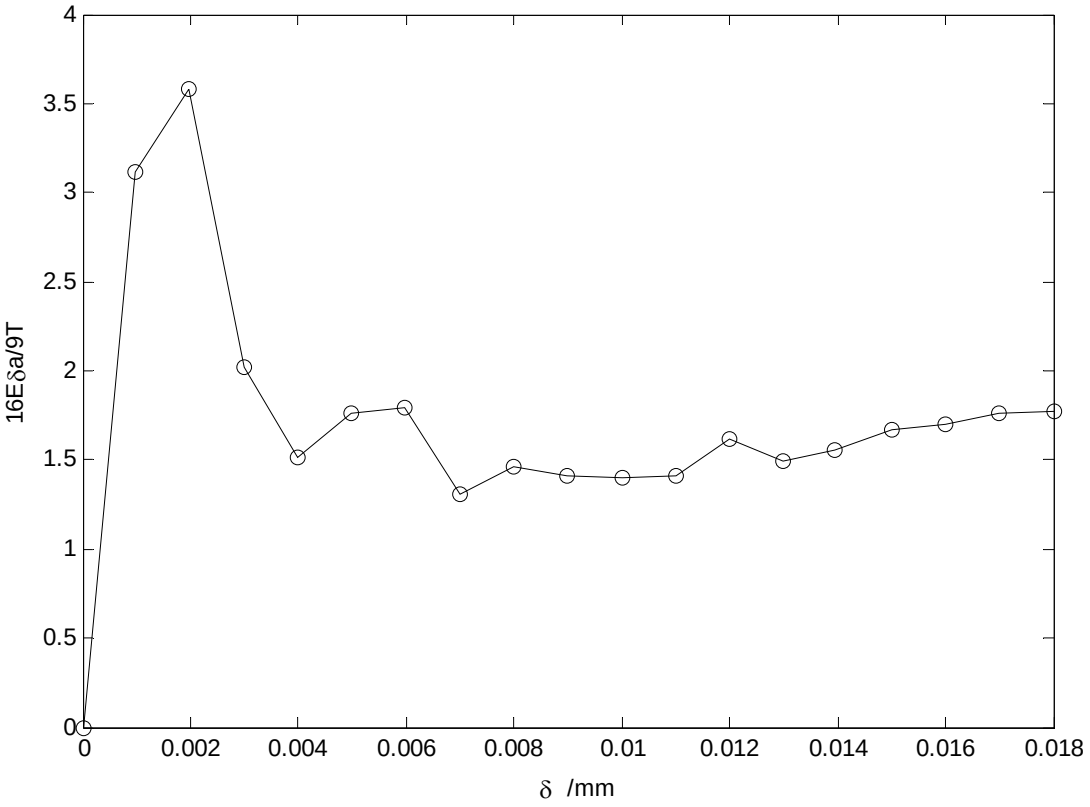

Figure 4.14 Plot of $16E\delta a/9T$ against δ for control sample under shear at displacement rate 0.001 mm/s. This plot is obtained from data in stage 1.

reduction, one might expect the contact area to decrease with increasing shear – as predicted by the theory of SB. However, as pointed out by Yao *et al* [26], in a fibrillar sample bending of the fibrils due to shear can significantly reduce normal stiffness of the sample. Since the normal load is fixed in our experiments, increase in compliance of the fibrils will cause the contact area to increase. Apparently, the increase in normal compliance initially more than compensates for the increase in energy release rate, so the net result is that the contact area first increases with increasing shear. Eventually, the shear displacement increases strain energy sufficiently to reduce the contact area.

Our experiments suggest that there is a connection between adhesion and friction as both the effective work of adhesion in the CB test and the critical shear force in the sliding experiments increase with fibril separation. In addition, our experiments show that the transition from no sliding to steady sliding is an unstable process. For an isotropic half-space, the peak friction force T_c can be estimated using the theory of SB, i.e.,

$$T_c = \sqrt{4W_f \pi RP + 6\pi^2 R^2 W_f^2} \tag{4.2}$$

where P is the applied normal load, R is the radius of the indenter, and W_f is the critical energy release rate associated with the transition from no sliding to sliding. For a fibrillar surface, equation (4.2) is not valid if W_f is the true work of adhesion. Here, we apply it to extract a phenomenological, effective interfacial toughness, *as if* the substrate were a half-space. Since the variation of T_c with fibril separation is known from our experiments, we can use (4.2) to study how W_f varies with fibril spacing. The result is shown in Figure 4.15, where W_f is plotted against fibril spacing. Because the normal load is negligibly small in our experiments, W_f is directly proportional to T_c. (Compare Figures 4.15 and 4.7.) A comparison of Figure 4.5 and Figure 3.7 shows that in these samples, the enhancement of static friction over the control is considerably greater than the enhancement of CB-measured work of

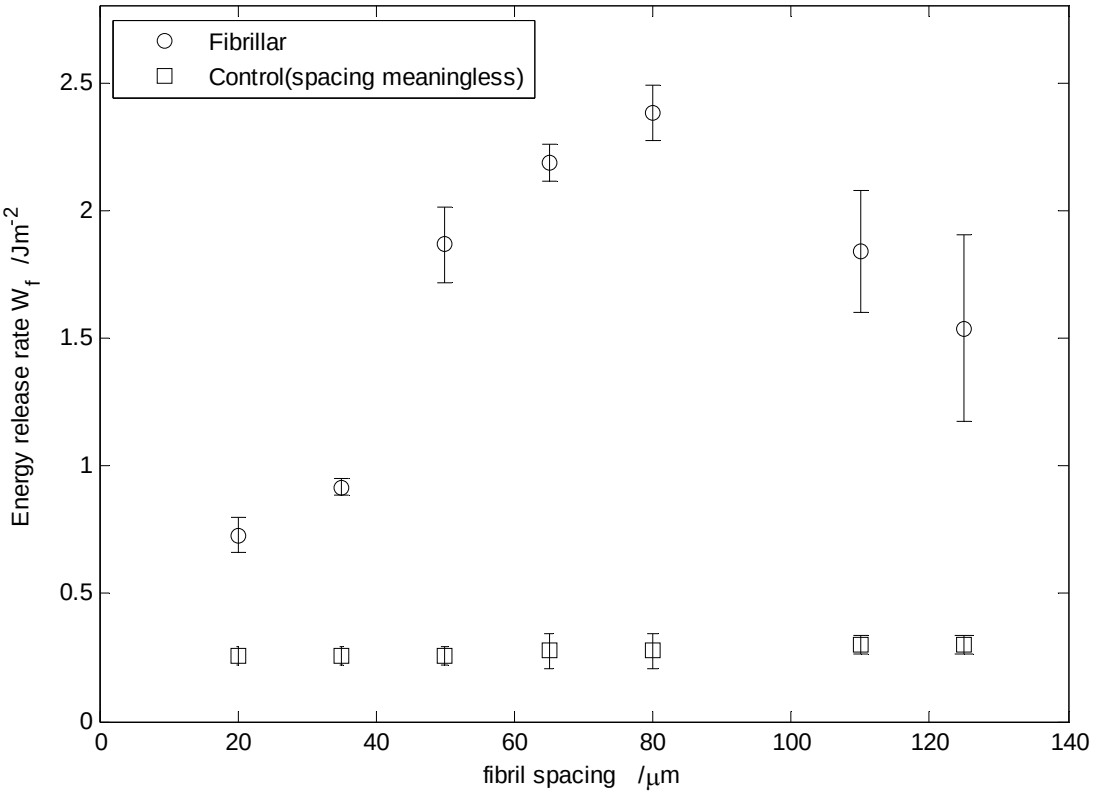

Figure 4.15 Effective interfacial toughness, W_f, of film-terminated fibrillar samples and control samples as a function of inter-fibril spacing.

adhesion. For the fibril spacing of 80 μm, W_f is about six times greater than the corresponding CB-measured effective work of adhesion. It should be noted that the samples with fibril spacing of 110 and 125 μm are damaged during the test. That is, for large inter-fibrillar spacing, maximum shear force is limited by fibril damage. Since, load bearing area of the fibrils decreases with increasing spacing, so does the maximum shear force in this regime.

Finally, we speculate the mechanism of steady sliding. Our results show that under steady sliding conditions the fibrils in the contact zone are subjected to much less shear compared to conditions just before the static friction peak. In particular, the contrast in our video images shows that the thin film inside the contact region is partially detached from the indenter. This detachment, we propose, annihilates the crack pinning mechanism, which is the primary cause of the large adhesion hysteresis observed in our previous indentation tests [21]. Due to the applied shear displacement, the film buckles at the leading edge of contact, and a bubble is trapped inside this buckled film. Like a Schallamach wave on a flat elastic substrate, steady sliding is accommodated by the propagation of this bubble from the leading to the trailing edge. The remaining question is why kinetic friction is independent of the fibrillar structure. This question can be addressed using an observation of Briggs and Briscoe [40]. They realized that the passing of a wave corresponds to the peeling and re-adhering of the contact area. This means that the friction energy dissipated must be the same as the difference in the work to open and close an interface crack moving through the same nominal area as the indenter. Since the crack pinning mechanism is no longer operative, this energy difference is small and, in particular, it does not depend on the fibrillar spacing.

In summary, the key results of this paper are:

1. The static friction force for fibrillar samples can be an order of magnitude larger than for a flat control. It increases with inter-fibril spacing and represents a mechanical instability driven by energy release rate and resisted by an effective work of adhesion. This effective work of adhesion operates by the same crack trapping mechanism as found under normal separation of the interface.

2. In shear tests on flat control samples, the contact area decreases with increasing shear before the onset of sliding. In some cases the onset of sliding is preceded by a small peak in the shear force - shear displacement plot. Sliding is accommodated by the propagation of trapped bubbles from the trailing to the leading edge.

3. In shear tests on film-terminated fibrillar samples, the contact area initially increases with increasing shear. Buckling of the thin film ahead of the leading edge is observed. This supports the idea that sliding is accommodated by the propagation of a Schallamach-like wave. During steady sliding, the film inside the contact zone is partially detached from the indenter.

4. The kinetic friction is independent of fibril separation. Furthermore, the kinetic friction of fibrillar samples is the same as the flat control samples.

Many important issues are not addressed in this work. For example, we have not presented results on the effect of shear displacement rate and normal load on static and dynamic friction. Since the focus of this work is on experimental observations, we have not presented a quantitative micromechanical model of the observed phenomenon. These issues will be addressed in future works.

REFERENCES

[1] M. Scherge and S.N. Gorb, *Biological Micro and Nanotribology: Nature's Solutions*. Springer-Verlag, Berlin, 2001.

[2] N.W. Rizzo, K.H. Gardner, D.J. Walls, N.M. Keiper-Hrynko, T.S. Ganzke and D.L. Hallahan, *J. R. Soc. Interface,* 2006*,* **3**, 441-451.

[3] K. Autumn, Y.A. Liang, T.S. Hsieh, W. Zesch, W.P. Chan, T.W. Kenny, R. Fearing and R.J. Full, *Nature*, 2000, **405,** 681-685.

[4] T. Eisner and D.J. Aneshansley, *Proc. Natl. Acad. Sci. USA,* 2000, **97,** 6568-6573.

[5] R. Ruibal and V. Ernst, *J. Morphology*, 1965, **117**, 271-294.

[6] U. Hiller and *Z. Morph. Tiere*, 1968, **62**, 307-362.

[7] U. Hiller and *J. Bombay Nat. Hist. Soc.*, 1976, **73**, 278-282.

[8] B.N. Persson, *J. Chem. Phys*., 2003, **118,** 7614-7621.

[9] B.N.J. Persson and S. Gorb, S. *J. Chem. Phys.*, 2003, **119**, 11437-11444.

[10] C.-Y. Hui, N.J. Glassmaker, T. Tang and A. Jagota, *J. R. Soc. Interface,* 2004*,* **1**, 35-48.

[11] E. Arzt, S. Gorb and R. Spolenak, *Proc. Natl. Acad. Sci. USA,* 2003*,* **100**, 10603-10606.

[12] W. Li, A. Amirfazli, *Adv. Colloid Interface Sci.*, 2007, **132**, 51.

[13] W. Li, A. Amirfazli, *J. Colloid Interface Sci.*, 2005, **292**, 195.

[14] N.J. Glassmaker, A. Jagota, C.-Y. Hui and J. Kim, *J. R. Soc. Interface*, 2004, **1,** 22-33.

[15] B. Yurdumakan, N. R. Raravikar, P. M. Ajayan and A. Dhinojwala, *Chem. Comm.*, 2005, **30**, 3799-3801.

[16] C. Majidi, R.E. Groff, Y. Maeno, B. Schubert, S. Baek, B. Bush, R. Maboudian, N. Gravish, M. Wilkinson, K. Autumn and R.S. Fearing, *Phys. Rev. Lett.*, 2006, **97**, 076103.

[17] A. Peressadko and S.N. Gorb *J. Adhes.*, 2004*,* **80**, 247-261.

[18] M. Sitti and R.S. Fearing, *J. Adhes. Sci. Technol.,* 2003, **17,** 1055-1073.

[19] S. Kim and M. Sitti, *Appl. Phy. Lett.*, 2006, **89**, 26, 261911.

[20] S. Gorb, M. Varenberg, A. Peressadko and J. Tuma. *J. R. Soc. Interface*, 2006, 1-6.

[21] N. J. Glassmaker, A. Jagota, C.-Y. Hui, W. L. Noderer and M. K. Chaudhury, *Proc. Natl. Acad. Sci. USA*, 2007, **104,** 26, 10786-10791.

[22] W.L. Noderer, L. Shen, S. Vajpayee, N.J. Glassmaker, A. Jagota and C.-Y. Hui, *Proc. R. Soc. London, A*, 2007, **463,** 2631-2654.

[23] L. Ge, S. Sethi, L. Ci, P. M. Ajayan and A. Dhinojwala, *Proc. Natl. Acad. Sci. USA*, 2007, **104,** 26, 10792-10795.

[24] A. Jagota, C.-Y. Hui, N.J. Glassmaker and T. Tang, *MRS Bulletin*, 2007, **32** 492-495.

[25] D.J. Irschick, C.C. Austin, K. Petren, R. Fisher, J.B. Losos and O. Ellers, *Biol. J. Linn. Soc*., 1996, **59,** 21-35.

[26] H. Yao, G. Della Rocca, P.R. Guduru and H. Gao,J. R. Soc. Interface, 2007, DOI: 10.1098/rsif.2007.1225.

[27] M. Sitti, personal communication.

[28] N.J. Glassmaker, A. Jagota, C.-Y. Hui and M.K. Chaudhury, *Proc. Annual Meeting of the Adhesion*, Blacksburg, VA: Adhesion Society, 2006, pp. 93–95.

[29] A.R. Savkoor and G.A.D. Briggs, *Proc. R. Soc. London, A,* 1977, **356,** 1684, 103-114.

[30] R.D. Mindlin, *Trans. A.S.M.E.*, 1949, 71.

[31] R.D. Mindlin, *J. Appl. Mech.*, 1949, **16**, 259.

[32] K.L. Johnson, K. Kendall and A.D. Roberts, *Proc. R. Soc. London,* A, 1971, **324,** 301.

[33] K.L. Johnson, *Contact Mechanics*, Cambridge University Press, 1985.

[34] K.L. Johnson, *Proc. R. Soc. London, A*, 1997, **453**, 163-179.

[35] A. Schallamach, *Wear*, 1971, **17**, 301-312.

[36] A.A Koudine and M. Barquins, *J. Adhesion Sci. Technol.*, 1996, **10**, 951-961.

[37] A.A Koudine and M. Barquins, *Int. J. Adhesion and Adhesives,* 1997, **17**, 107-110.

[38] C.J. Rand and A. Crosby, *Appl. Phys. Lett.*, 2006, **89**, 261907.

[39] M.K. Chaudhury and K.H. Kim, *Eur. Phys. J. E*, 2007, **23**, 175–183.

[40] G.A.D. Briggs and B.J. Briscoe, *Wear,* 1975, **35**, 357-364.

CHAPTER 5

ADHESION OF A FILM-TERMINATED FIBRILLAR INTERFACE: STUDY OF FRICTIONAL MECHANISM AND EFFECT OF RATE

5.1 Abstract

We further study the shear response of a bio-inspired fibrillar interface that consists of poly(dimethlysiloxane) (PDMS) micro-posts terminated by a thin film using different indenters . The static friction is found to be significantly enhanced compared to a flat control. This enhancement increases with inter-fibril spacing. The dynamic friction is surprisingly independent of inter-fibril spacing. We also investigate the mechanisms that govern kinetic and static friction and study the effect of displacement rate on the frictional properties of our structure. Our experiments show that the fibrils in the contact zone undergo stick-slip despite the fact that sliding is macroscopic steady. The presence of the thin film contributes significantly to the friction force as well as maintaining a constant contact area that is independent of the fibril spacing. Our preliminary results show that dynamic friction is approximately independent of loading rates, whereas static friction increases with it. Finally our data seems to support the simple idea that the dynamic frictional stress is a constant independent of fibrillar spacing and loading displacement rate.

5.2 Introduction

Studies have shown that a thin layer of micro-scale fibrillar structures on the skin of small animals such as insects and lizards play an essential role in their adhering ability to various surfaces [1-7]. This ability can be attributed to the following: (1) fibrillar structures enhance compliance which facilitates good contact [8, 9]; (2) they

are less sensitive to flaws and stress concentrations [10]; (3) smaller scale spatula-like contacting end further increase contact compliance resulting in stronger adhesion [11].

Motivated by these natural systems, several groups have fabricated synthetic mimics with various polymer [10, 12-19] and carbon nano tubes [20-22] that have demonstrated enhanced adhesion and interesting friction behavior [12-27]. Among these, Glassmaker *et al* [19] developed a two-level fibrillar interface consisting of a micro-array of fibrils which are connected at their top by a continuous thin film (see Figure 5.1). The adhesion of these micro-fibril arrays was studied by an indentation test [19, 29]. It was found that the adhesion strength of this interface was enhanced up to 5 fold over an unstructured sample (flat surface) of the same material. The adhesion enhancement was attributed to a crack trapping mechanism [19, 29]. Briefly it is caused by the spatial variation of energy which is available to drive the interfacial crack between the film and the indenter. When the crack front is located between fibrils, the available energy for crack growth is low, since the film carries very little strain energy. Therefore, the crack front is trapped behind the edges of fibrils, which are positions where the local energy release rate is the minimum. This means that once crack growth occurs, it becomes unstable, since the local energy release rate will increase and the intrinsic work of adhesion is a material constant. It is this instability that leads to the hysteresis and the large effective work of adhesion. (Figure 5.2).

The friction behavior of our film terminated micro-fibril arrays were also studied using the apparatus shown in Figure 5.3. Two main characteristics were reported for behavior under shear [30]. The first was that the force required to initiate sliding, the static friction, is up to 9 times higher in fibrillar samples than in an unstructured sample. Secondly, the force required to maintain sliding remains substantially unchanged for samples with different center to center distance between neighboring fibrils. Based on experimental observations it was argued that static

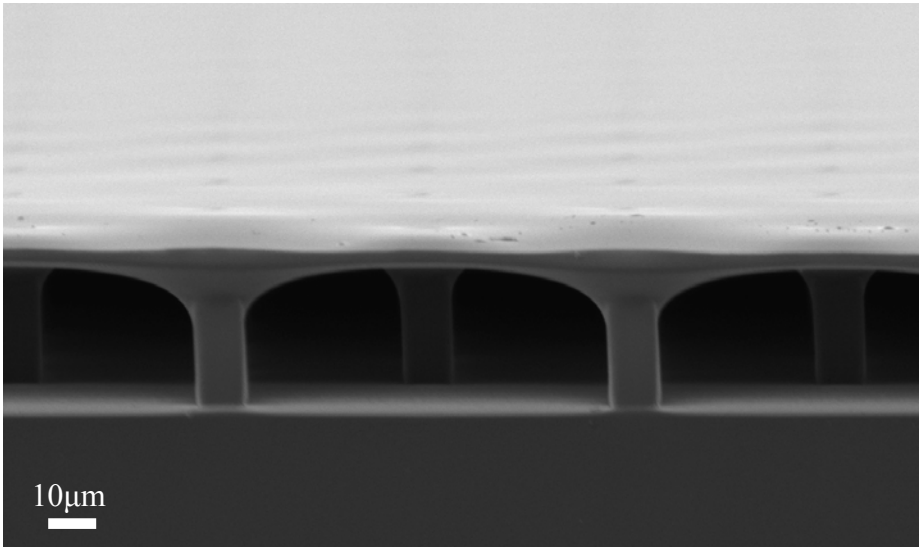

Figure 5.1 Scanning electron micrograph of the synthetic fibrillar interface with thin film terminated fibril array. Fibrils with a square cross-section 10 μm in width and about 30 μm in length are arranged in a square pattern. The nearest neighbor distance between fibrils in this case is around 65 μm. The terminal film is about 4μm in thickness.

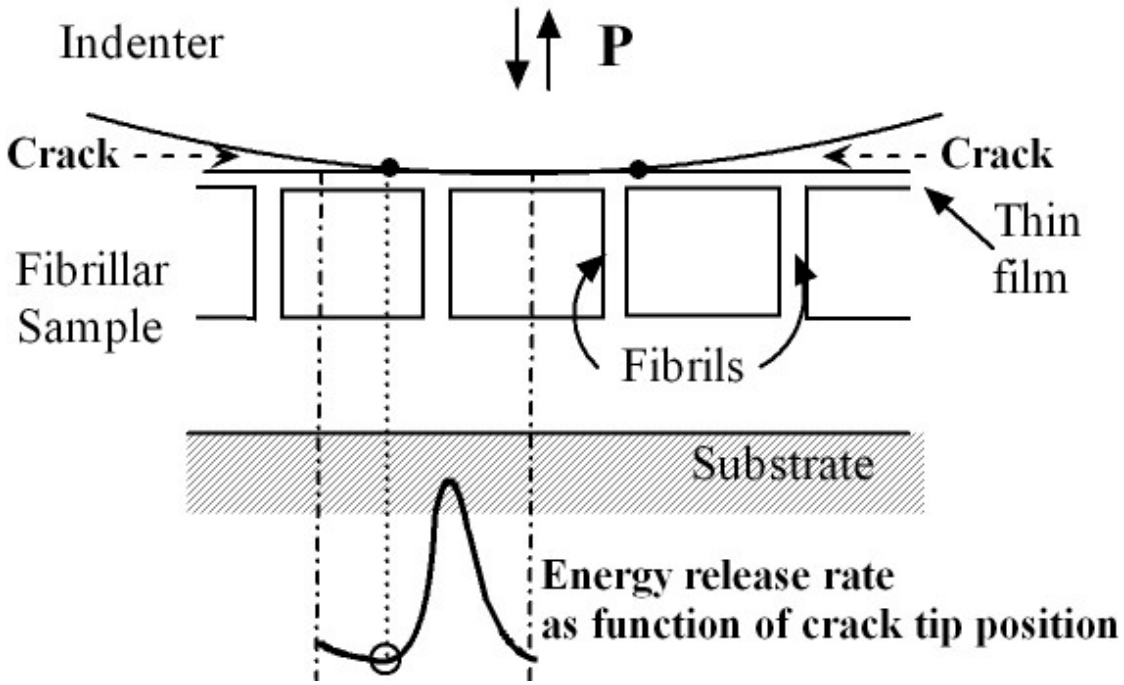

Figure 5.2 Illustration of crack trapping in our film-terminated fibrillar structure. The energy release rate depends on the crack tip position and is typically small when the tip is between fibrils. Numerical simulations have shown that the minimum energy release rate occurs when the crack is just at the left of the edge of a fibril, as highlighted by a circle in the figure. Thus, the crack tip will be trapped in this position until a sufficiently large load is applied. Since the energy release rate is increasing rapidly after the trapped position, unstable crack growth will occur once the crack tip moves, leading to dissipation.

friction enhancement, although quantitatively different from enhancement under normal indentation, is essentially due to the same crack-trapping mechanism.

There are other studies on friction of micro-fibril arrays. Kim *et al* [23] studied the friction of a micro-fibril array consists of polyurethane fibers with a spatulated tip. The static friction of their fibrillar samples is three times higher than their unstructured flat control sample whereas the kinetic friction is about 50% lower. Similar to our finding, their fibrillar sample exhibits a pronounced static friction peak. Bhushan and Sayer [24] conducted friction tests on polyvinylsiloxane spatula terminated micro-pillar arrays using a reciprocating friction tester. The static friction of their fibrillar samples is slighter higher than their unstructured flat control sample whereas the kinetic friction is about 3 times higher. Yao *et al* [25] used a film-terminated fiber array similar to ours but with tilted and larger fibers. They found that under pure friction there is a static friction peak. During sliding, stick-slip behavior was observed. And the average kinetic friction is lower than the static friction. They also found that detachment forces increases with tilt angle. On the other hand, Murphy *et al* [26] found that the static friction of tilted polyurethane fibers (20º with respect to vertical) with three different tip geometries is lower than the static friction of their flat control sample. Lee *et al* [27] slid an array of very stiff polypropylene fibers on a flat substrate at a fixed speed and found very large friction enhancement. They did not observe a static friction peak; instead, the friction force continues to increase during sliding and reaches a plateau value.

A difficulty in the interpretation of friction experiments is the absence of experimental data on the local deformation of fibrils during sliding. For example, just because a constant velocity is imposed on a micro-fibril array does not mean that fibrils in the array are undergoing steady sliding. The purpose of this chapter is to provide this information and to study in greater depth the mechanisms that govern

kinetic and static friction in our structure. In particular, we examine in detail the deformation history of fibrils as they pass through the contact region during sliding. We also explore the role of the terminal film on friction by comparing friction behavior of roof and roofless samples. We show how a combination of film buckling and fiber deformation both inside and outside the contact zone can lead to a dynamic friction that is independent of fibril spacing. We also investigate the dependence of static friction on shear rate.

The remainder of the paper is organized as follows. Experimental methods are described in Section 5.3. In section 5.4.1, we study the mechanism of sliding friction using a cylindrical indenter on samples with terminal films. In addition, we carried out sliding experiments using a spherical indenter on micro-fiber arrays without terminal films. Results of shear experiments at different rates of displacement are presented and discussed in section 5.4.2. We conclude with a summary in Section 5.5.

5.3 Experimental Methods

5.3.1. Fabrication of Specimens

Figure 5.1 is a scanning electron micrograph of a typical sample. The fibril array is part of a Poly(dimethylsiloxane) (PDMS, Sylgard 184, Dow Corning) block which has a thickness of 650 μm. The fibrils have square cross-section 10 μm in width and about 30 μm in length and are arranged in a square pattern. The thickness of the terminal film was about 4μm. With all other dimensions fixed as described above, a series of such fibrillar samples, with varying nearest center to center distance between fibrils, $20\mu m \leq w \leq 110\mu m$ were used for this study. We also studied control samples that either lacked both the fibril layer and the terminal film (flat unstructured controls) or that had the fibrils but no terminal film. This fibrillar interface was first introduced in Glassmaker *et al* [19]. The fibrils, terminal thin film, and backing are all of the

same material, PDMS. PDMS is a highly elastic incompressible solid with a Young's modulus $\approx$ 3MPa. Fabrication procedures are described in detail in [19, 28, 29].

5.3.2 Friction measurements

The behaviors of micro-fibril arrays under shear are studied using the same apparatus first described in [30] (see Figure 5.3). Briefly, a sample is placed on an inverted optical microscope. The sample is brought into contact with a glass spherical indenter by applying a compressive normal load *P which is* fixed by attaching the indenter to a mechanical balance (Ohaus 310D). In this work, we use a spherical indenter with a radius of 4mm to study the roofless samples and to study rate effects on static friction on film-terminated (roof) samples. Sliding experiments are performed using a cylindrical indenter with a circular cross-section (radius 1mm). The length of the cylinder is longer than the sample width. Since high adhesion between indenter and sample damages our fibrillar samples, indenters were pre-coated with a self-assembled monolayer (SAM) of *n*-hexadecyltrichlorosilane to reduce interfacial adhesion. Details of this surface treatment can be found in [19]. Samples were driven by a variable speed motor (Newport ESP MFA-CC) and motion controller (Newport ESP300) at a fixed velocity. The imposed sample velocity varied from 0.05μm/s to 0.3mm/s. The frictional force was measured by a load cell (Honeywell Precision Miniature Load Cell Model 31-50) attached on the balance arm in the direction parallel to the sliding motion.

5.4 Results

5.4.1 Static and Sliding/Dynamic friction

Shear experiments conducted using cylindrical and spherical indenter have similar force-displacement response. Shear force (see Figure 5.4 and Figure 5.14) first

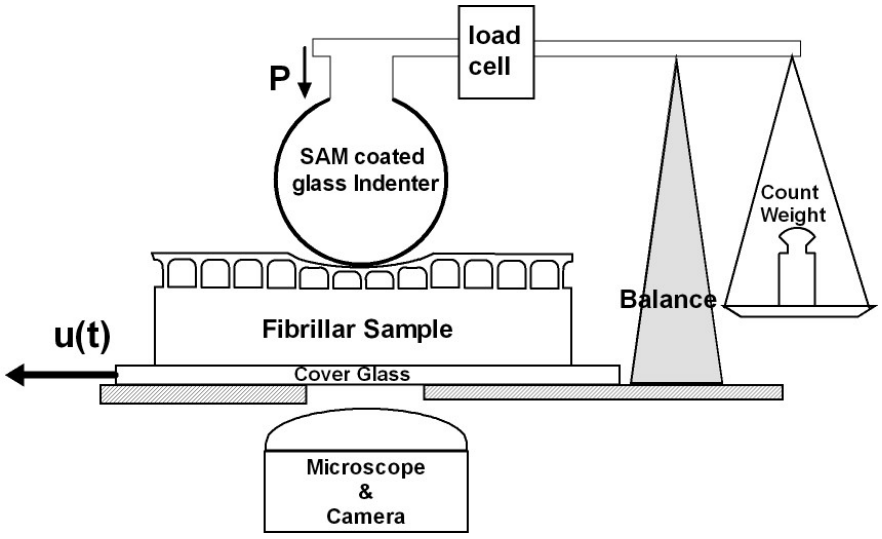

Figure 5.3 Schematic of the apparatus used for the shear experiment (side view). A fixed load P is applied to the sample via a SAM coated glass indenter attached to a mechanical balance. The sample lies above an inverted optical microscope and is driven by a motor with velocities varying from 0.05μm/s to 0.3mm/s. Force is measured by a strain-gauge-based load cell fixed parallel to the motion. Indenters can be spherical or cylindrical.

rises up to a peak, then drops abruptly to a nearly constant value. These results are consistent with our previous data [30]. Visual examination of optical micrographs indicates that, before the force drop, there is no overall sliding between the indenter and top surface of the sample; therefore, the peak value is defined as the static friction force. After the load-drop, there is a transition to a steady sliding process, during which the force remains nearly constant. This constant value is taken as kinetic or sliding friction. From Figure 5.4 (see also Figure 5.18(b)), one can see that for fibrillar samples the static friction is significantly larger than that of the flat control, and increases with increasing rate of loading. Dynamic friction is lower and is substantially independent of shear rate. (We have previously shown that dynamic friction in the fibrillar samples is independent of fibril spacing, w, whereas static friction increases significantly with increasing w [30].) Unlike dynamic friction, static friction depends on both fibril spacing and displacement velocity in a significant way.

5.4.1.1 Shear experiments via cylindrical indenter

The contact line underneath a spherical indenter during sliding has a complicated shape. To minimize this effect, we used a long glass circular cylinder indenter. The SAM coated cylinder indenter has a circular cross-section with a radius of 1mm. The center line of the cylinder is perpendicular to the direction of sliding. In this geometry, the contact line is parallel to the center line of the indenter and undulates periodically along it. Our experiments consisted of one flat control sample and 3 fibrillar samples with spacing 50, 65 and 80μm. These samples were pulled at a rate of 5$\mu m/s$. Force versus displacement curves for 3 different spacings and the flat control are plotted in Figure 5.4.

This figure shows that static friction increases with spacing up to w = 65 μm. For the sample with w = 80 μm, the shear force is sufficiently large to tear fibrils from

the backing. This damage reduces the static friction. However, the dynamic friction is not affected since sliding takes place at much lower force and at a different part of the sample. Figure 5.4 also shows that dynamic friction is much lower than static friction and is practically independent of spacing, similar to our observation for spherical indenter.

Using a synchronized video, pictures of the contact zone of all fibrillar samples were taken with frequency of one frame per 2/3 second. To illustrate how we measure deformation of fibrils in the contact zone, we present several snapshots of a sample with $w = 80\ \mu m$. Figure 5.5(a) is the 1st still frame of the contact region. The top ends of the fibrils appear as fuzzy grey circles since the joint between fibrils and the film is rounded (see Figure 5.2). The small darker squares indicate the joints between the bottom of fibrils and the thick backing layer. In Figure 5.5(a) no shear was applied so the squares and circles overlap each other. When sheared, they are mutually offset (see Figure 5.5(b) and (c)); by measuring the distance between them, one can determine the relative deflection of each fibril.

5.4.1.1.1 Static friction

To capture the micromechanics of fibril deformation before sliding, we analyzed a sequence of snap shots for a micro-fibril array with $w = 65\ \mu m$ to determine the deflections of one particular row of fibrils as function of time. (The side-view of the deformation can be referred to the bottom part of Figure 4.13) This spacing is used for understanding static friction and since the $w = 80\ \mu m$ sample was damaged by shear. These time dependent deflections are shown as contours in Figure 5.6. The horizontal axis of Figure 5.6 indicates the location of the bottoms of the fibrils with respect to a fixed point in the sample which is translated horizontally at a fixed rate with respect to the fixed indenter. The slanted line in Figure 5.6 indicates the position

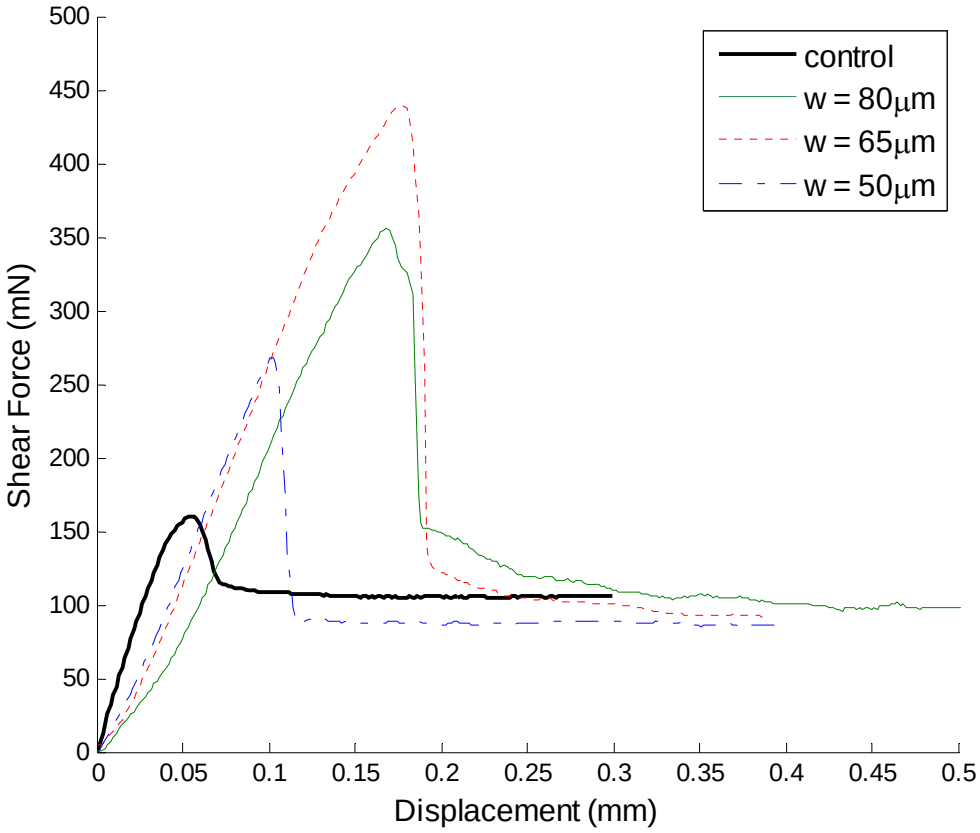

Figure 5.4 Typical force-displacement plots of the sample under shear.

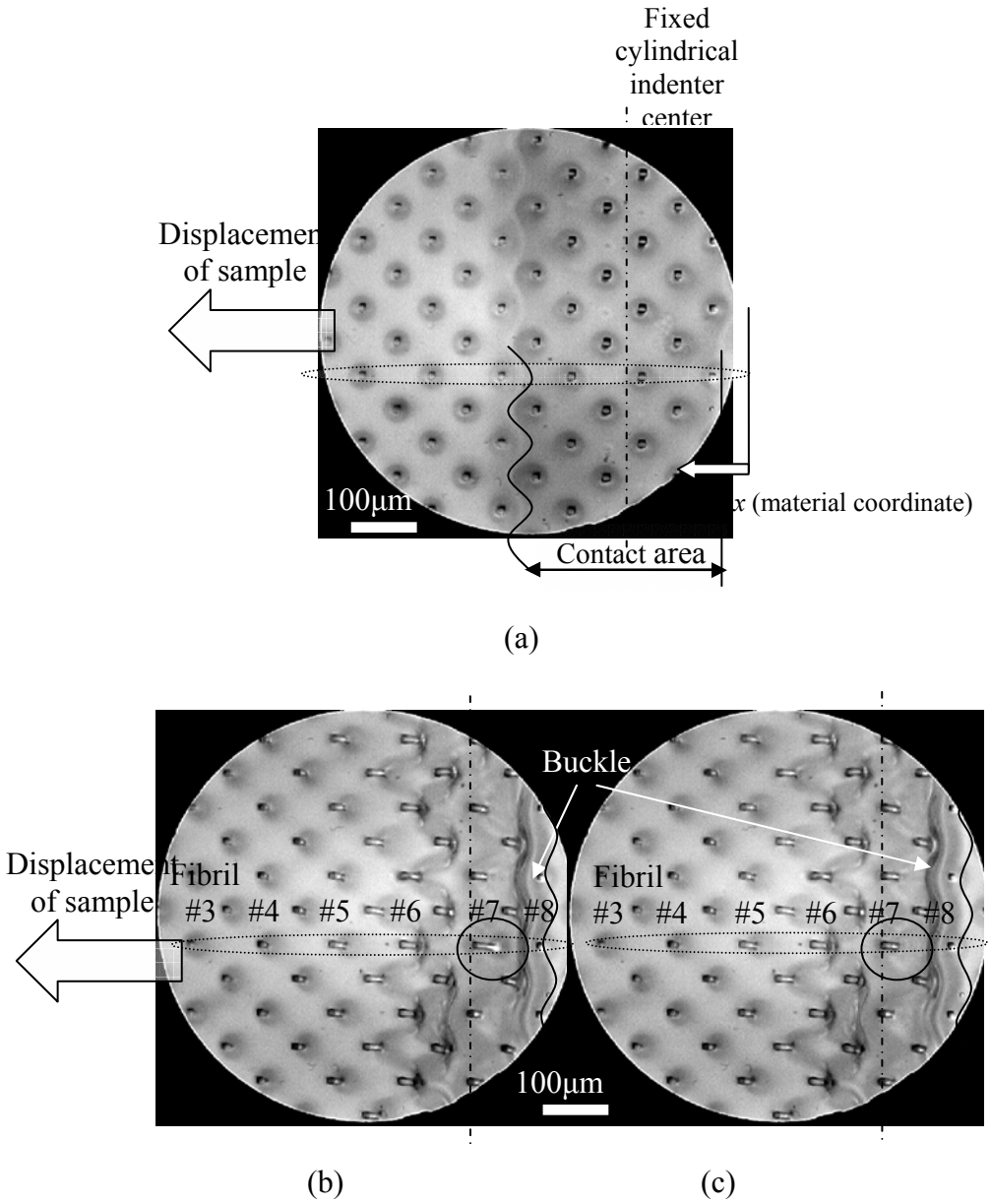

Figure 5.5. Images for the fibrillar sample of $w = 80\mu m$ sliding at $5\mu m$/s under a SAM coated cylindrical indenter with a 1mm radius. (a) Initial contact (b) &(c) two consecutive still frames illustrate the sudden recovery of one fibril located near the leading front.

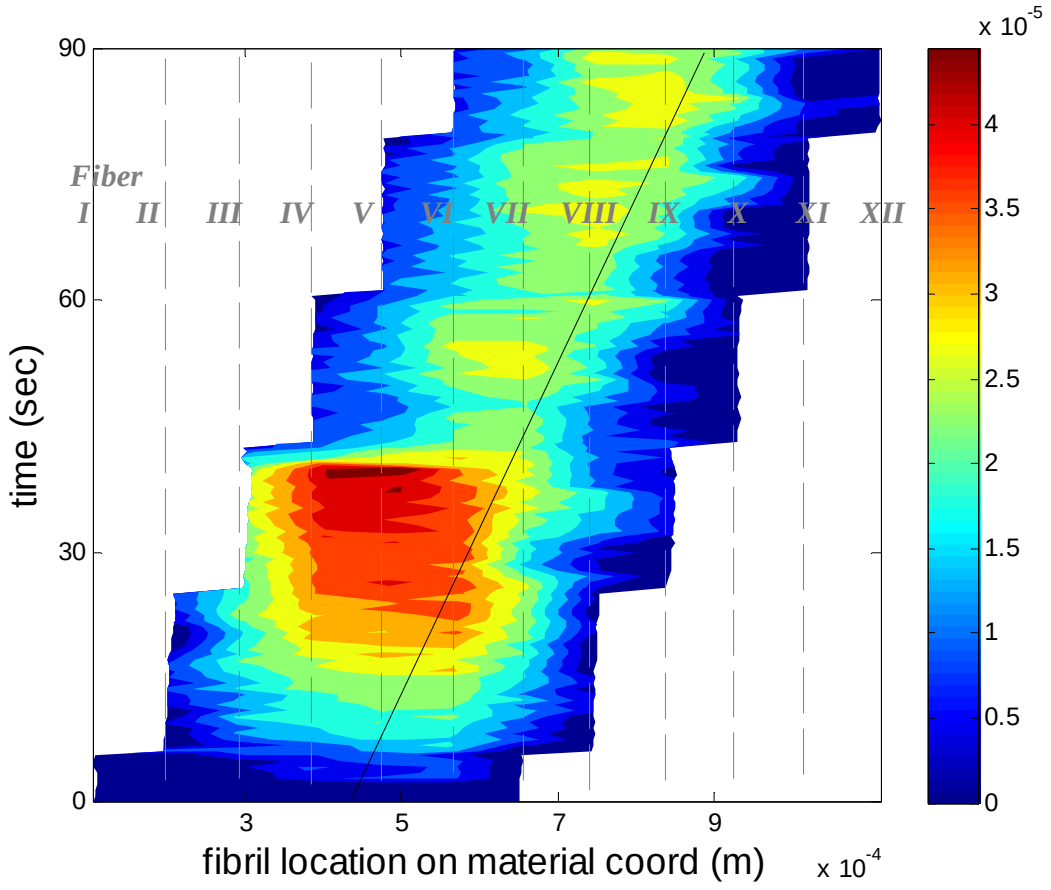

Figure 5.6. Deflection development of one particular row of fibers in fiber array with $w = 65\ \mu m$. Solid slanted line indicates the location of indenter center with respect to one material point.

of the center of the indenter. The slope of this line is the speed of the indenter relative to the sample. Before the static friction peak($t \leq 40$ sec), fibrils *III,IV, V* and *VI* are in contact with the indenter. Fibril *V* lies slightly to the left of the center line of the indenter. This figure shows that the fibrils in the leading edge (*V* and *VI*) have much larger deflection than those in the trailing edge (*III*) - a phenomenon that we have not reported in our previous paper [30]. A careful reexamination of our previous data which was obtained using a spherical indenter also confirms this observation for fibril arrays without damage. The fact that fibrils near the trailing edge of the contact zone have lower deflections means that there must be micro-slip occurring in this region. We attribute this to the fact that the film in this region is under tension and is peeled at a low angle. Micro-slip of the film is unlikely inside the leading edge of contact since the film there is under compression. As the shear displacement increases, fibril 6 snaps back and partially release its stored energy before the static friction peak.

5.4.1.1.2 Dynamic friction

Now we return to the study on dynamic friction. Figures 5.5(b) and (c) are two consecutive frames capturing a sudden partial recovery of shear in one fibril (highlighted by a circle) near the leading edge of the contact during sliding. Because the sample is moved at a constant rate, the deformation history of each fibril entering the contact zone should be approximately the same. To study this history, we marked a single row of fibrils (highlighted in Figure 5.5(b), (c)) with symbols 3, 4…8. The deformation histories of these fibrils during sliding are followed by measuring the fibril deflections on a sequence of consecutive still frames. Figure 5.6(b) and c show that the microscope view range is larger than the contact width and the number of fibrils in a row is limited to 6. This means that the history of some fibrils can be traced only partially. Figure 5.7 shows the deflection of fibrils 1, 2…10 as a function of time.

The time origin in Figure 5.7 is set to the time when fiber 1 is about to exits the view scope.

Figure 5.5(b) and (c) shows that when a new fibril enters the contact zone (see highlighted circle), it bends and stretches (see Figure 5.5(b) and (c)). This causes the shear force acting on the fibril to increase until it reaches a critical value. Then it suddenly slips backwards and partially releases its stored elastic energy, as shown in Figure 5.5(b) and (c) (circles). This caused the previously buckled film between this fibril and the fibril to its right to unbuckle partially. Figure 5.7 plots the time history of deflection for fibrils 1 – 10. Note that fibrils 1-5 are already out of the leading edge so complete deformation histories are not recorded. As each fibril enters the contact zone, it first shears at a rate determined by indenter velocity, shown by the slanted lines (fibrils 7–10). At a critical shear, a fibril suddenly slips backwards and releases some of its elastic energy. These slip-stick events occur repeatedly with decreasing magnitude and are shown in more detail for a particular fibril in Figure 5.8. Note that at the end of each slip/stick event, the fibril reloads at the approximately the same displacement rate of the indenter ($5\mu m$/s) as shown by the slant lines in Figure 5.8. As mentioned earlier, we expect that all the fibrils have similar deformation history. That this is indeed the case is shown in Figure 5.9(a) which is a superposition of all 10 curves in Figure 5.7. The main trace in Figure 5.7(a) is the trace of fiber 7 in Figure 5.7. Figure 5.9(b) shows a schematic of a snapshot of the deformation pattern underneath the indenter. Deformation of the fibril at section A, B and C marked in 5.9(a) can be matched to those in Figure 5.9 (b). Figure 5.9(a) shows a very important feature of our film-terminated micro-fibril array that is absent in an array without a *continuous* terminal film. This figure shows the force carried by the film *outside the contact zone* (behind the trailing edge) can actually be greater than the force carried by the fibrils inside the contact zone. The continuous film allows the shear force to be

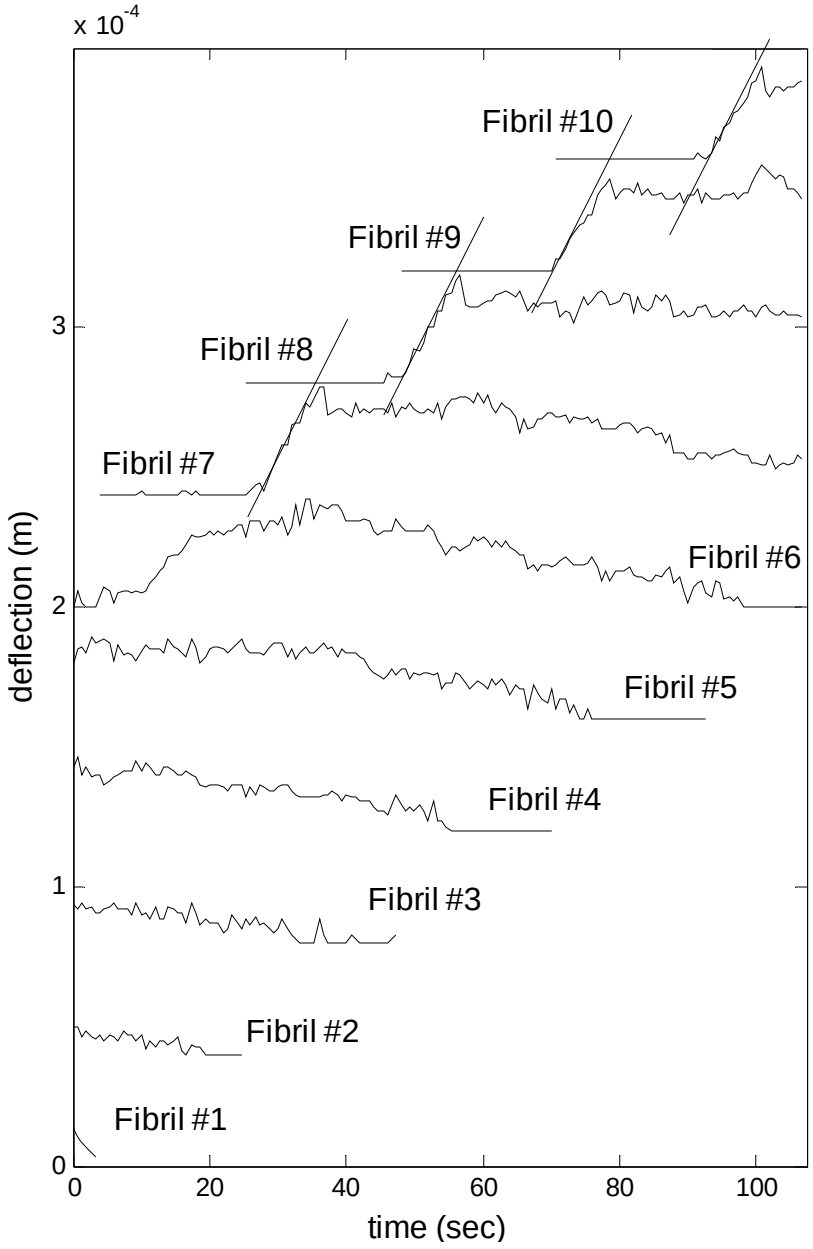

Figure 5.7 Deflections of 10 fibrils as a function of time. Fibril numbers are those marked on Figure 5.5. Solid line has a slope =5.0 $\mu m/s$.

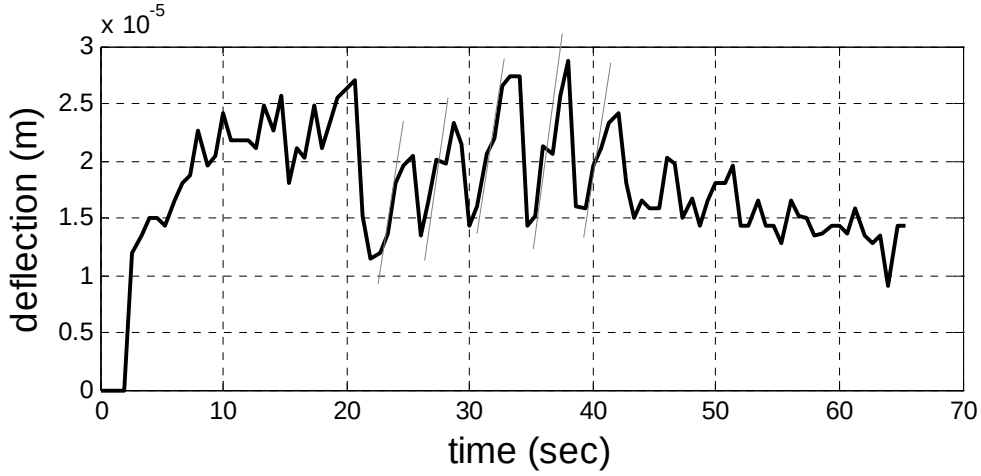

Figure 5.8 Typical slip-stick behavior of one fibril on sample with w =50 μm. Solid line has slope =5.0 $\mu m/s$.

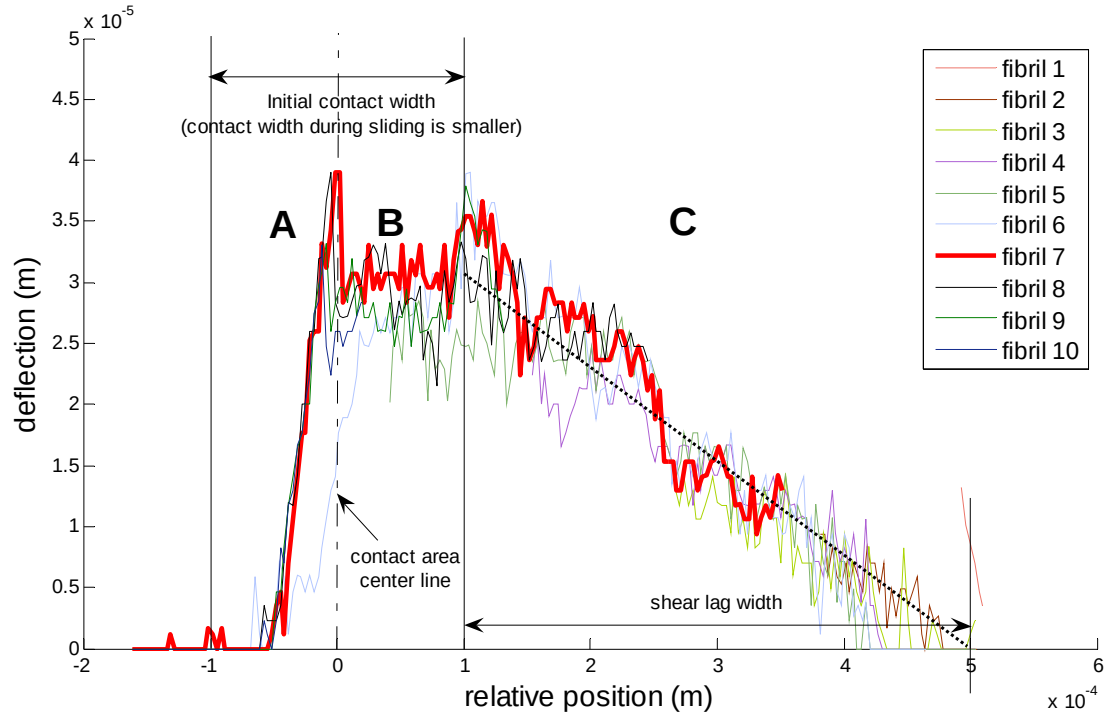

(a)

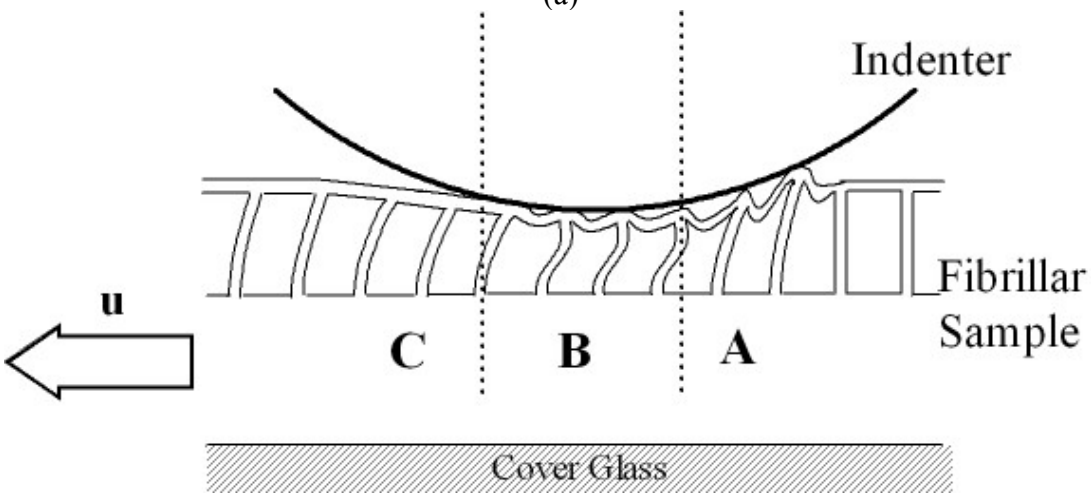

(b)

Figure 5.9 (a) Deflection versus positions of the fibrils in Figure 5.7. These traces are obtained by offsetting the curves in Figure 5.7 by its relative distance to the first fibril. (b) Schematic of deformation of fibrils during sliding. The regions A, B and C correspond to those in Figure 5.9(a).

transmitted to non-contact fibrils, as shown by the shear displacements of fibril outside the contact zone in Figure 5.5(b) and (c). The width of the non-contact region where shear force is non-negligible is defined as the shear lag length. Figure 5.10 plots the shear deflection in region B and the shear lag length in region C as a function of nearest fibril spacing w. Note that the *average* shear deflection in B and the shear lag length increase linearly with w. We will now show that this feature counteracts the quadratic decrease in fibril density with increasing spacing, leading to a dynamic friction that is approximately independent of spacing.

Let us denote the number of fibrils in the contact zone A and B by 1, 2,…n and the numbers of fibers in the shear lag zone C by m + 1, ……n. Thus, $n + m$ is the total number of fibers in regions *A, B, C* in Figure 5.9(a). If we look at Figure 5.9(a), the total load F supported by a single row of fibers is:

$$F = \sum_{j=1}^{n+m} f(d(x_j)) \tag{5.1}$$

where $d(x_j)$ is the deflection acting on the j fiber which occupies the position x_j relative to a coordinate system x attached to the steadily moving indenter (x=0 is the location of start of region B). $f(d(x_j))$ denotes the shear force on fibril j and is assumed to depend on the deflection $d(x_j)$ of fiber j at x_j. Let L_s denote the length of the shear lag region C. Since the crack is normally trapped behind a fiber, we assume that the first fibril in region C is at a distance of w away from the last fiber in region B so

$$m=[L_s/w] \tag{5.2}$$

where $[L_s/w]$ is the greatest integer function. Since there are $1/w$ rows of fibers per unit length of the cylinder, the total force per unit length of the cylinder is

$$F_T = NF = \frac{F}{w} = \frac{1}{w}\sum_{j=1}^{m+n} f(d(x_j)) \tag{5.3}$$

Figure 5.9(a) suggests the following approximation:

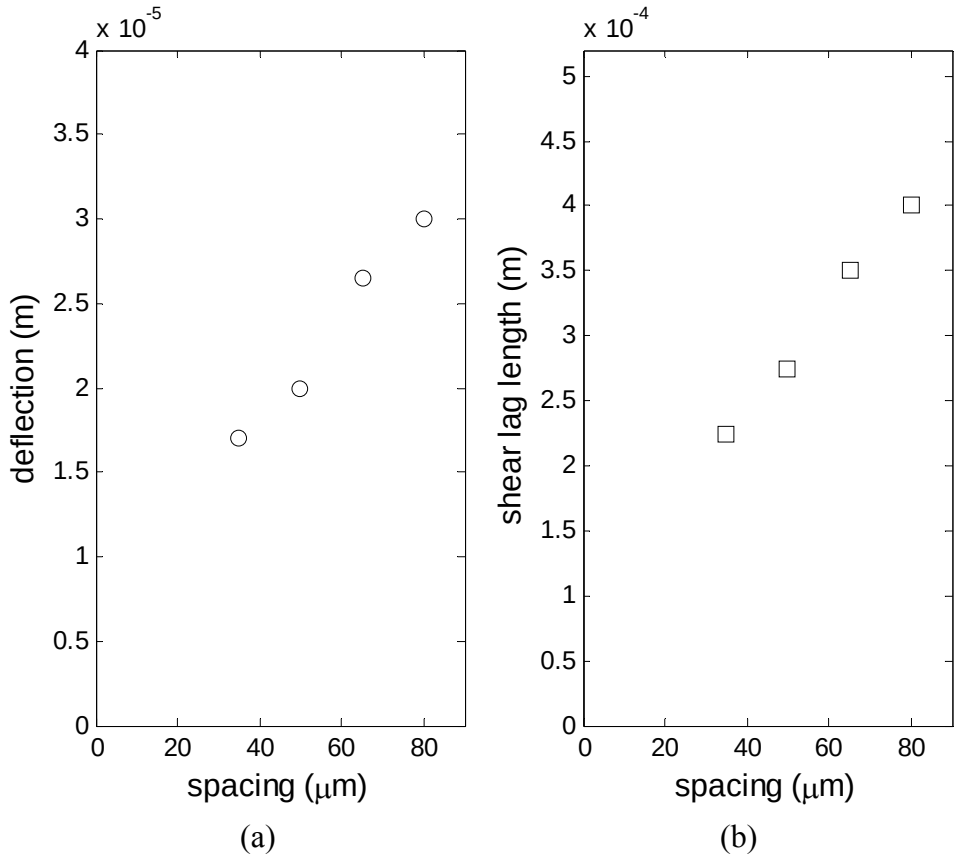

Figure 5.10 (a) Average shear deflection in region B, (b) shear lag length versus spacings. Shear lag length is indicated in Figure 5.9(a).

$$d(x_j)=\begin{cases} d_B & x_j \text{ in B} \\ d_B\left(1-\dfrac{x_j-b}{L_s}\right) & x_j \text{ in C} \end{cases} \qquad (5.4\text{ a,b})$$

where b is the width of region B. Thus,

$$\sum_{j=1}^{m+n} f(d(x_j)) = nf\left(d_B\right) + \sum_{j=1}^{[L_s/w]} f(d(x_j)) \qquad (5.5)$$

Let us assume that there is a linear relation between the shear force and the deflection, that is,

$$F(d)=Ad \qquad (5.6)$$

where A is a constant that depend on the material behavior and geometry of a fibril. Using $x_j-b=jw$, we have

$$\sum_{j=1}^{m+n} f(d(x_j)) = Ad_B\left\{n+[L_s/w]-\frac{w}{L_s}\sum_{j=1}^{[L_s/w]} j\right\} = Ad_B\left\{n+[L_s/w]-\frac{w}{L_s}\frac{[L_s/w]([L_s/w]+1)}{2}\right\} \qquad (5.7)$$

According to Figure 5.10 (a), (b)

$$d_B = p+qw \approx qw, \qquad L_s = \alpha+\beta w \approx \beta w, \qquad (5.8)$$

This means that L_s/w and d_B/w is independent of w. Since

$$F_T = \frac{Ad_B}{w}\left\{n+[L_s/w]-\frac{w}{L_s}\frac{[L_s/w]([L_s/w]+1)}{2}\right\}, \qquad (5.9)$$

F_T is also independent of w. We remark that this analysis is not a model for dynamic friction. It merely confirms our experimental data on slip mechanism are consistent with a dynamic friction that is approximately independent of spacing.

5.4.1.2. Friction of Fibrillar Sample without Terminal Film

It is interesting to compare the shear response of micro-fibril samples with and without terminal films or roofs. Roofless samples are made of the same material. The geometries of these samples are identical to the film terminated samples except a

wider range of w, from 20μm to 125μm is used. All shear experiments are performed with a displacement rate of 0.5 $\mu m/s$ using the same spherical glass indenter of radius 4mm and the same normal force (much smaller than the shear force) is imposed on the indenter. Shear force versus displacement responses for 8 samples with different spacings are shown Figure 5.11. The top curve in this figure corresponds to a flat control sample.

There are two main differences between samples with and without roofs. First, the shear force in the roofless sample initially decreases with shear displacement, reaches a minimum, then increases. Second, there is no static friction peak. A sequence of images of one sample (w = 50 μm) are shown in Figure 5.12(b)-(f). The labels (b to f) correspond to the points on the force-displacement curve in Figure 5.12(a). Figure 5.12(b) is the image of the sample before shear is applied. The contact line is highlighted in this figure. Fibrils in the center of contact were slightly buckled due to the applied compressive load (see insert in Figure 5.12(b)). After shear is applied, these fibers recovered from their buckled state, releasing elastic energy, which performs work on the loading machine. Eventually, fibers bend in the direction opposite to the shear direction and a force resisting motion develops. This adjustment releases energy and is responsible for the initial decrease in shear force from point b to c. For samples with very wide fibril spacing, the compressive force on each fibril is higher and is sufficient to change the buckling mode to resemble that of a fibril bent by shear. For these samples, most of the fibrils are already bent in the direction opposite to the shear direction; as a consequence, the decrease in initial force is less significant or absent. From c to e, contact increases with shear. In Figure 5.12 (d), the four fibrils in the center of contact (see highlight region) are contacting the indenter on their *lateral* sides. The region with lateral contact increases with shear displacement until point (e). After (e), the contact zone as well as the number of fibers making

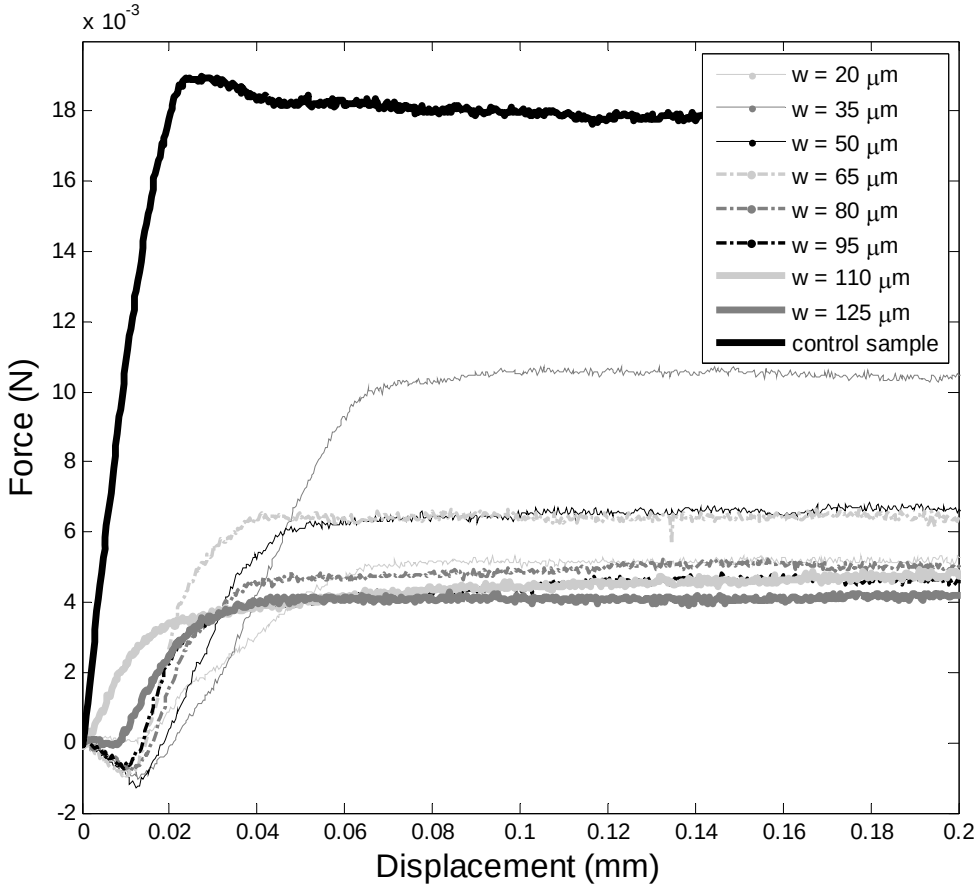

Figure 5.11 Typical force displacement curve of fibril sample without roof under shear. Shear displacement is conducted at rate of 0.5 *μm/s* via a spherical indenter with radius of 4mm.

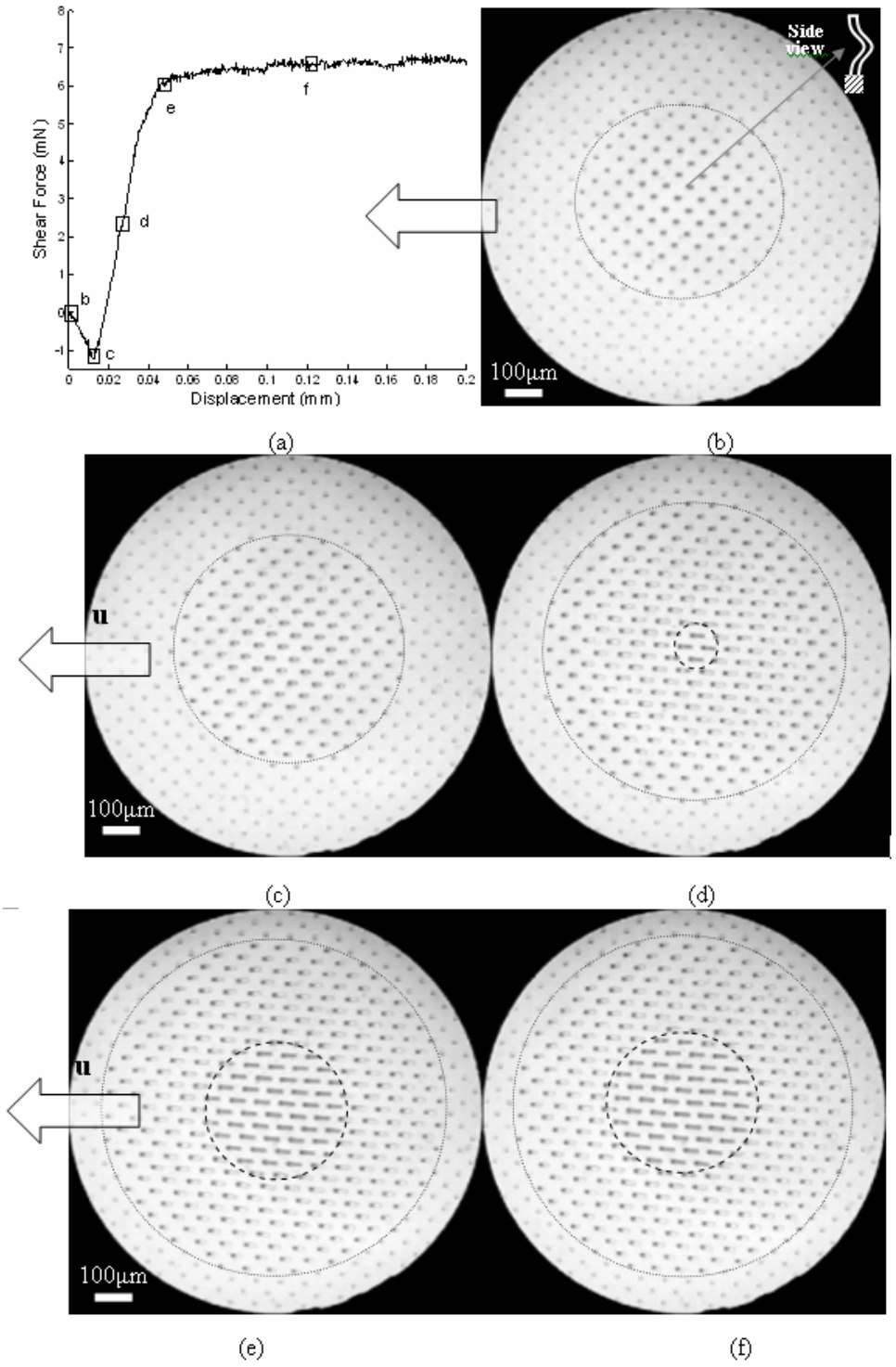

Figure 5.12 (a) Shear force versus shear displacement for a roofless sample with w =50μm. The spherical indenter is sheared at a rate of 0.5$\mu m/s$. 5.12(b-f) Sequences of images of the same sample. Labels (b)-(f) correspond to points in Figure 5.12(a).

lateral contact remains unchanged with shear displacement.

Normalized dynamic friction of the roofless samples F/F_c are plotted against fibril spacing w in Figure 5.13, where F is the dynamic friction force and F_c is the dynamic friction obtained using a flat control sample under the same loading conditions. As a comparison, we include our previous data for film terminated samples (with a spherical indenter of 2mm radius) in the same figure [30]. As shown in Figure 5.13, the dynamic frictions of film-terminated samples are independent of fibril spacing. On the other hand, dynamic frictions of the roofless samples follow a power law in spacing, that is,

$$F / F_c \propto w^{-3/4} \quad . \tag{5.10}$$

It is noted that the roofless sample with $w = 20\ \mu m$ lies below the power law fit. For this case, none of the fibrils makes lateral contact with the indenter. Since lateral contact increases the actual area of contact per fibril, it is not surprising that the dynamic friction is overestimated by the power law fit.

5.4.2 Effect of shear rate on friction

Figures 5.14 show the shear force versus displacement of a film-terminated fibrillar sample with $w = 35\ \mu m$ for five different shear displacement rates. For comparison, the behavior of the flat unstructured control sample is shown in Figure 5.15. A few new observations about the force versus displacement traces are worth mentioning. First, the shear force is insensitive to loading rate before the static friction peak. This suggests that bulk viscoelasticity, if it exists, is weak and that rate effects arise from interfacial processes. Second, the fibrillar samples show an initial stiffening. This stiffening occurs due to an initial increase in contact area despite the fact that the normal load is fixed during the entire test. It can be explained by the fact that as a fibril bends under shear, its normal compliance increases considerably. This

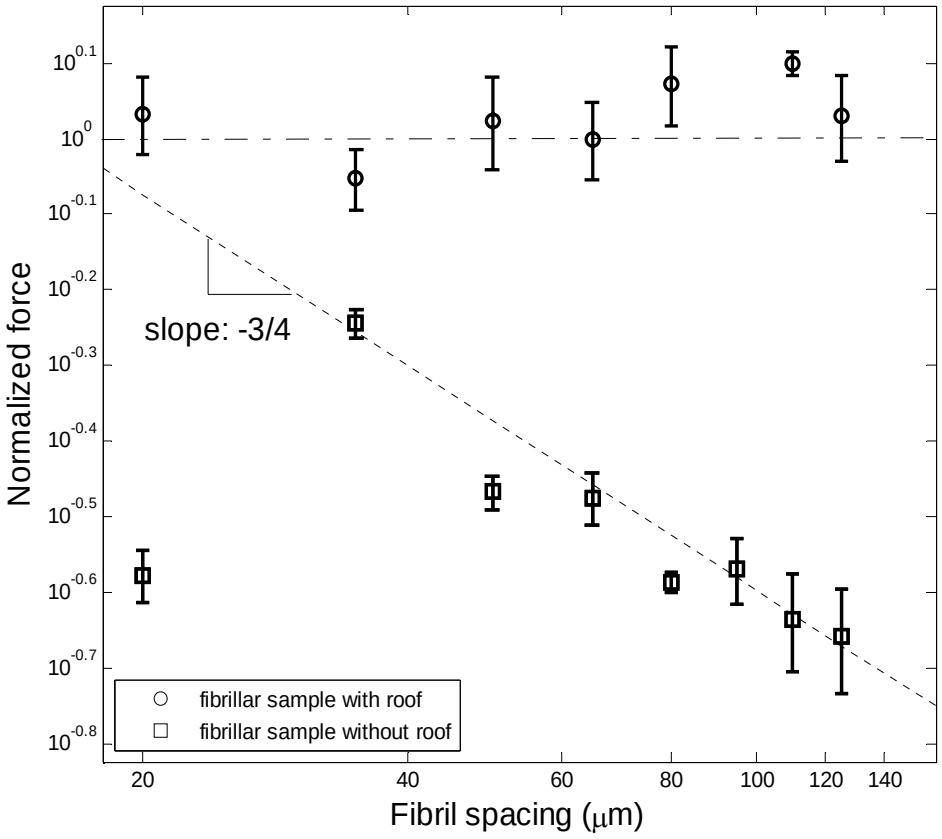

Figure 5.13. Comparison of dynamic friction of fibril samples with and without roof normalized by the dynamic friction of a flat control sample.

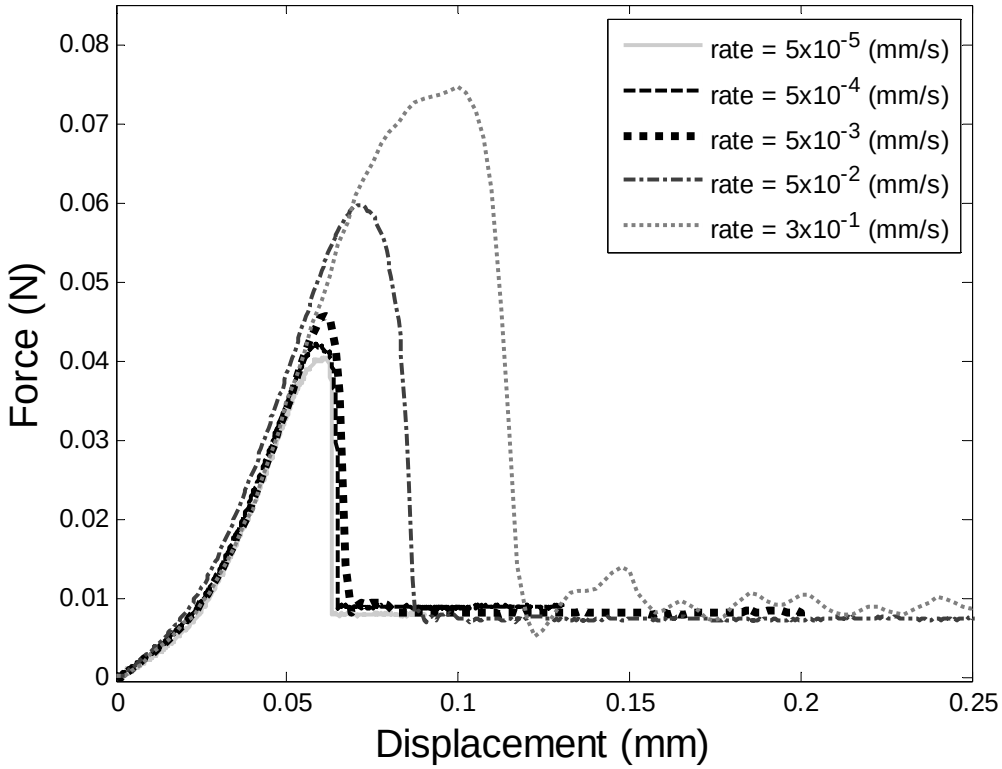

Figure 5.14 Typical shear force response of a film-terminated fibrillar sample with w=35 μm as a function of shear displacement under 5 different displacement rates.

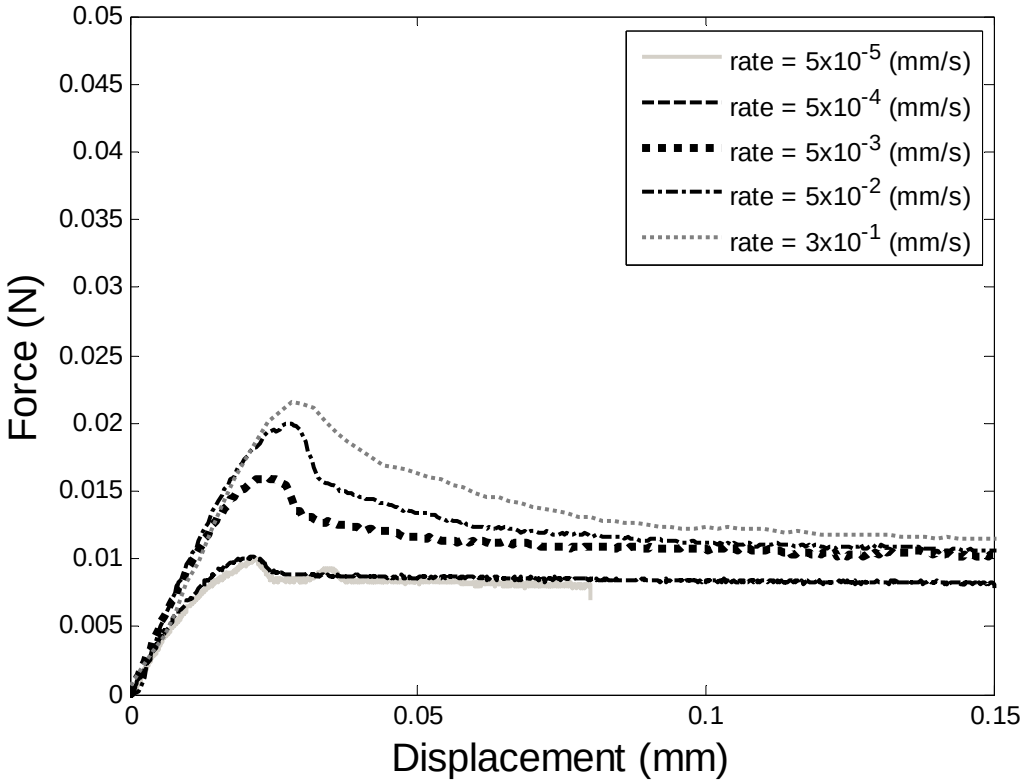

Figure 5.15 Typical shear force response of unstructured flat control sample as a function of shear displacement under 5 different displacement rates.

means that, for a fixed normal load, the contact area first expands, then eventually shrinks due to loss in contact and film buckling. Increase in contact area increases the number of contacting fibrils, resulting in increase in shear force. This stiffens the shear response of the fibrillar layer [31].

For flat unstructured control samples (Figure 5.15), the force response does not experience initial stiffening. Visually, we observe that the contact shrinks monotonically, in quantitative agreement with the Savkoor and Briggs [32] model for adhesive contact in shear. The static friction peak is significantly smaller than those in the fibrillar samples. Increasing shearing rate also increases static friction. The drop after peak load is not as abrupt as the fibrillar samples. In addition, unlike the fibrillar samples, dynamic friction in our control sample increases slightly with shearing rate.

Observations of sliding in the control samples suggest uniform slip between the indenter and the substrate except at the very leading edge. Specifically, if the entire contact region underwent uniform slip, then material points ahead of the front leading edge will enter the contact zone at the same rate. However, we do not observe this. Our video shows that the contact grows in small discrete additions that zip around the contour of the contact line, indicating that material points enter the leading edge at different rates. At the trailing edge, the deformation *before* sliding was similar to our previous work [30], that is, the surface forms a small valley immediately behind the trailing edge (see Figure 5.16(b)).

In our previous sliding experiments on flat control samples, the surface immediately behind the trailing edge periodically comes into partial contact with the indenter. As sliding proceeds, this partial contact region expands, resulting in full contact. The shape of this region at the trailing edge fluctuates between these two states. However, in this set of experiments, we did not observe such a fluctuation of contact. Instead, the deformation at the trailing edge during sliding is similar to that

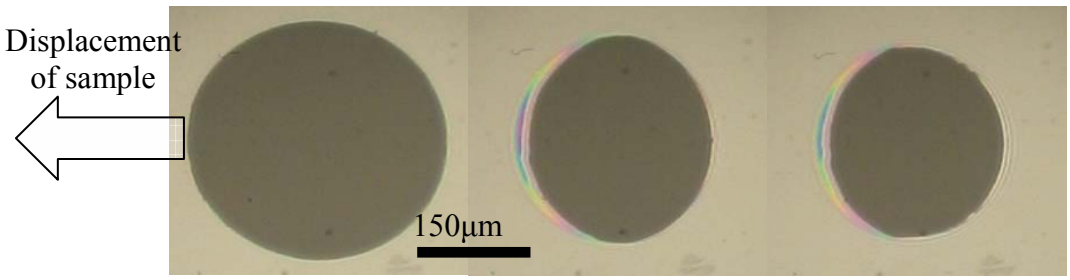

Figure 5.16 micrograph of control sample under shear (a) Initial contact area before shear (b) contact area before sliding, (c) contact area during sliding, the depression or valley is the color thin crescent behind the contact zone.

before sliding (Figure 5.16(b)). It should be noted that our previous experiments were conducted on an indenter with a smaller radius (2mm). Figure 5.17 plots the dynamic friction versus the static friction for a fibrillar sample (w = 35 μm) and the flat control. Again, in the fibrillar samples, dynamic friction remains relatively unchanged while static friction increases significantly with rate of loading. On the other hand, for flat control samples, kinetic and static friction forces are positively correlated. These data suggest that the sliding mechanisms in the two cases are different.

Figure 5.18 plots both the static and dynamic friction of flat control samples and fibrillar samples with w= 35 and 50 μm as a function of displacement rates on a semi-logarithmic axis. Each value on the plot represents the mean of 5 trials under same conditions; the error bars are the standard deviation of the trials. Consistent with the results in [30], the static friction of samples under the same test conditions increases with fibril separation distance, w. For these three samples (including the flat control), the static friction increases monotonically with displacement rate, starting at a lower threshold or plateau value for sufficiently small rates. On the other hand, the *mean* dynamic friction for all three samples remains almost constant under varying velocities (Fig 5.18(b)).

5.5. Summary and Discussion

Our results can be summarized as follows:

1. Film-terminated samples shows a static friction peak which increases with fibril spacing and loading rate for both spherical and cylindrical indenter. The dynamic friction is approximately independent of spacing and rate.
2. A static friction peak does not exist for roofless samples. Dynamic friction of these samples decreases with spacing. Lateral contact of fibril is primarily responsible for

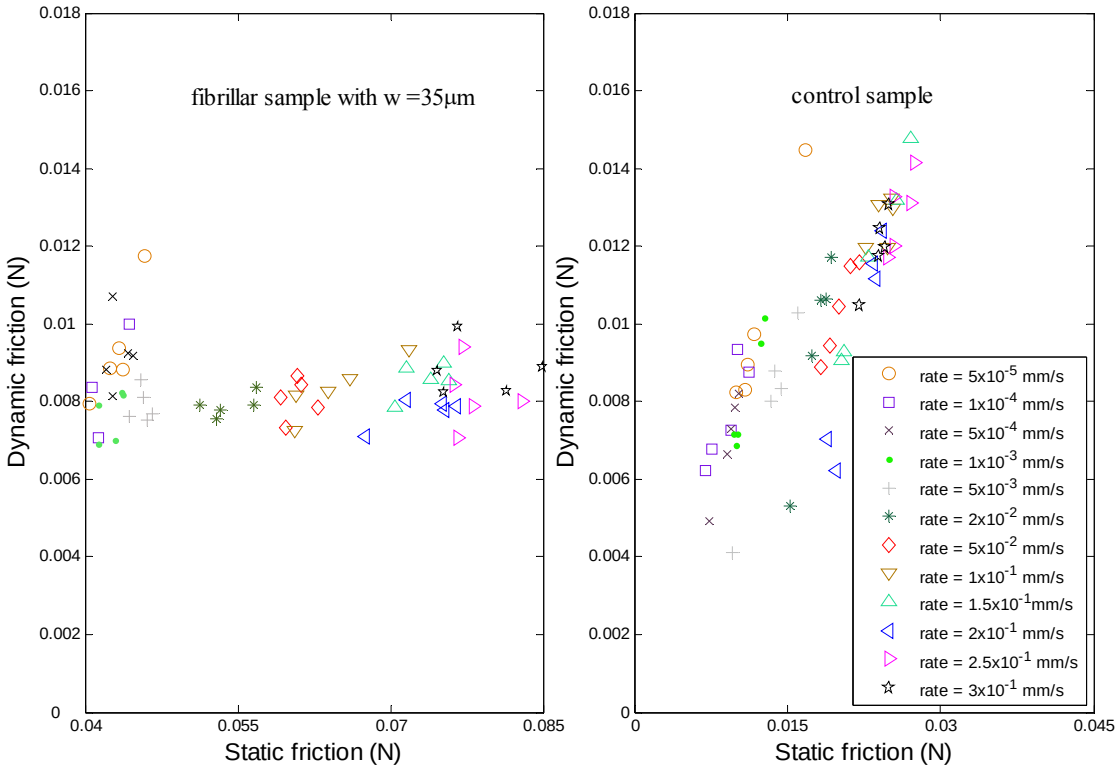

(a) (b)

Figure 5.17 dynamic friction plotted against static friction for (a) fibrillar sample (spacing = 35 μm) and (b) control sample.

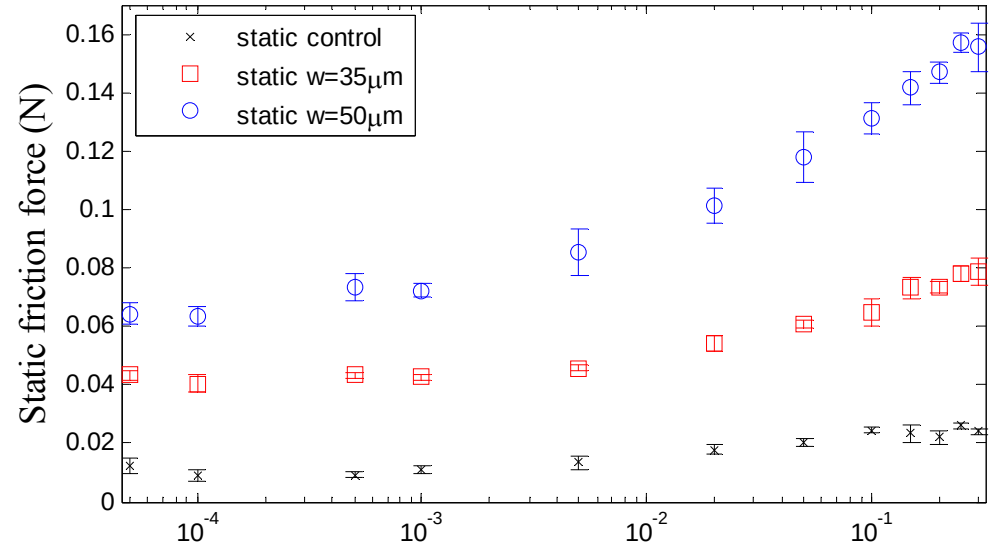

(a)

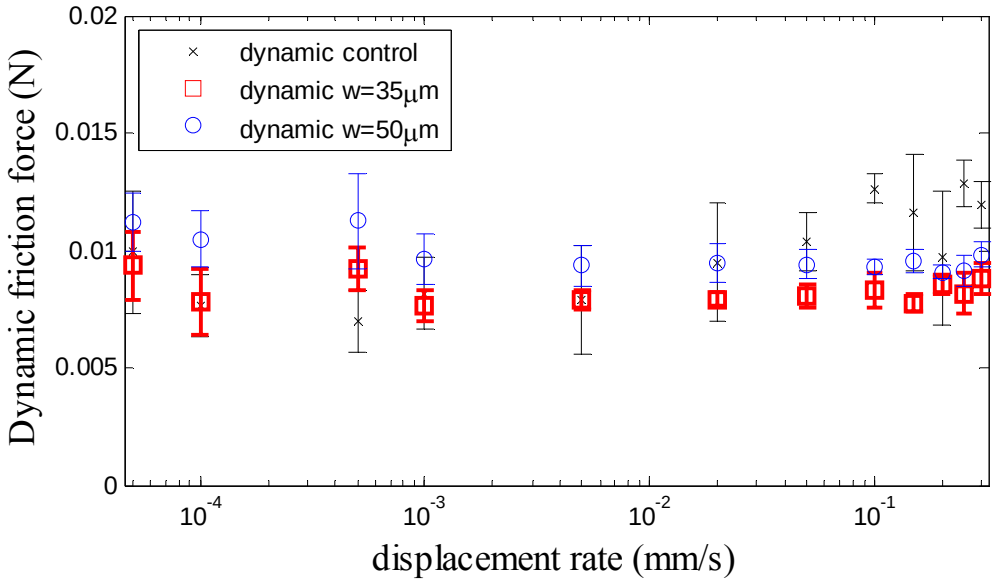

(b)

Figure 5.18 Static (a) and kinetic (b) friction of 2 fibrillar samples and control sample as a function of displacement rate.

the dynamic friction force.

3. Before the static friction peak, fibrils in film-terminated samples with small and intermediate spacings have higher deflections in the contact region to the right of the center of contact. This is consistent with our observation that reduction of contact area before static peak is due to the propagation of a buckled front inward from the leading edge. This means that micro-slip occurs in the trailing edge of contact. It should be noted that this conclusion may not be true for samples with large spacings, since fibrils in these samples are damaged before the static peak.

5. During sliding, *the film is in partial contact with the indenter. Contact regions are separated by buckled film.* A typical fibril in the contact zone undergoes slip-stick. The continuous film behind the trailing edge carries a substantial portion of the friction force.

Two questions remains. Why is the dynamic friction of our fibrillar independent of spacing (geometry) and displacement rate? In addition, why is the dynamic friction for fibrillar samples so close to the flat control sample?

In a previous work [30] we suggested a scenario to explain why the dynamic friction is independent of fibril spacing. From our observation that the film is in partial contact (bubble) with the indenter (see Figure 5.19), we suggested that the indenter motion is accommodated as a synchronization of film peeling and re-adhering at the end and front of the bubble respectively.

However, this mechanism implies that the energy needed to move the contact region a unit length must be equal to the difference of work of adhesion required to open and close a unit length of interface crack , that is:

$$F du = n\,(W^{+}-W^{-})\,b\,du \tag{5.11}$$

where F is the shear force required to maintain sliding, u is the sample displacement W^{+} and W^{-} denote the work of adhesion corresponding to opening and closing a unit

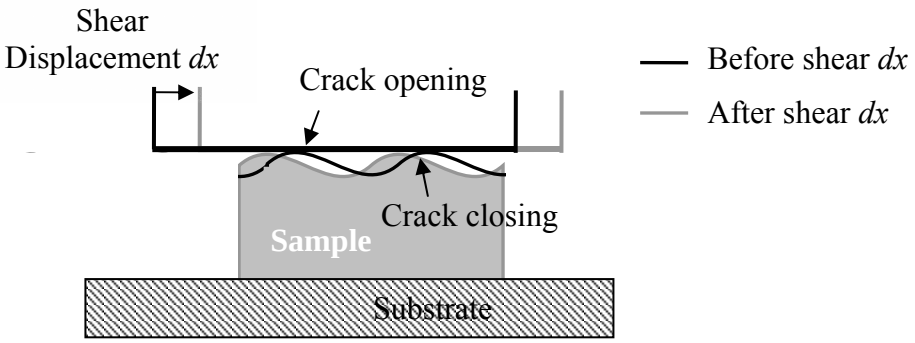

Figure 5.19 a schematic diagram of hard block slides on buckled sample.

length of crack respectively, b is the width of the specimen out of plane direction; and n is the number of bubble in the contact region.. Since the bubble is formed due to film buckling between fibrils, the number of bubbles n is approximately given by *the number of fibrils per unit area times* the nominal contact area. In our experiments (see Table A5.1) the nominal contact area is almost independent of spacing. This means that n is inversely proportional to the square of the spacing w. For our samples, terminated films, $W^- << W^+$ and W^+ increases with spacing as w^2 [29]. In order for the dynamic friction to be independent of spacings, W^+/w^2 must be approximately constant, which is not supported by our previous data using hexagonal arrays [29]. In addition, this picture of synchronizing peeling and re-adhering is inconsistent with our observation of slip-stick of fibrils in the contact zone.

Recently experiments of [33] shows that for PDMS, the dynamic friction F is related to the nominal contact area A by $F = \tau A$， where τ is interfacial shear stress and is a material constant that is independent of contact area. From our experiments, we can estimate how A varies with fibril spacing. To do this, we return to a previous set of friction test which used a small size indenter (2mm in radius) [30]. These samples were compressed with nominally zero preload and sheared at rate of 30μm/s. There is some uncertainty about the exact contact region, especially for samples with wide spacings. We estimated the contact area by treating the contact region as a circle. As shown in table A5.1, for $w \geq 30\mu m$, the contact diameters during steady sliding are approximately independent of spacing (see Appendix 4 for details). Since F is found to be approximately independent of spacing, our results are consistent with this simple model. This model will also explain why film-terminated samples have the same dynamic friction as the unstructured flat control.

There are two difficulties with our argument. First, the equation $F = \tau A$ applies only if the surfaces in contact are undergoing uniform slip, whereas in our case

the fibrils in the contact zone are undergoing slip-stick, this would mean that at least locally, the film is not in perfect contact. If our argument is valid, then this region of imperfect contact, which we associated with local buckling of the thin film, must be small in comparison with the nominal contact area, which is plausible. Second, our observation that the nominal contact area is independent of spacing seems to contradict the fact that the normal compliance should increase with spacing [29]. In fact, the deflection of fibrils in the contact zone is very large, on the order of the length of fibril, this means that the normal compliance of these fibrils are practically zero. There are two possibilities: (1) these fibrils "collapsed" on the backing layer so the thin film is in good contact with the indenter except near the top of the fibrils, where a small buckle must form. (2) the indenter is held up by the thin film which is in tension. Note that in both cases the contact area is approximately independent of the spacing, since the normal compliance of the fibrils is infinite. In the first case, the contact area is determined by the thickness of the backing layer, while in the second, the contact area is determined by the tension of the film. The first possibility is ruled out for our terminated film samples since the contact of the fibrils and the film with the backing surface will lead to different contrast in the video image which we did not observe. However, we believe this is the case for our roofless samples – the contact area of these samples are also approximately independent of spacing (see Table A5.2). For our film terminated samples, It is likely that case 2 applies. This is because the shear-lag region imposes a significant tension on the thin film whereas the fibril underneath the contact region has infinite normal compliance due to very large shear.

REFERENCES

[1] M. Scherge & S.N. Gorb, *Biological Micro and Nanotribology: Nature's Solutions*. Springer-Verlag, Berlin, 2001.

[2] N.W. Rizzo, K.H. Gardner, D.J. Walls, N.M. Keiper-Hrynko, T.S. Ganzke & D.L. Hallahan, *J. R. Soc. Interface,* 2006*,* **3**, 441-451.

[3] K. Autumn, Y.A. Liang, T.S. Hsieh, W. Zesch, W.P. Chan, T.W. Kenny, R. Fearing & R.J. Full, *Nature*, 2000, **405,** 681-685.

[4] T. Eisner & D.J. Aneshansley, *Proc. Natl. Acad. Sci. USA,* 2000, **97,** 6568-6573.

[5] R. Ruibal & V. Ernst, *J. Morphology*, 1965, **117**, 271-294.

[6] U. Hiller and *Z. Morph. Tiere*, 1968, **62**, 307-362.

[7] U. Hiller and *J. Bombay Nat. Hist. Soc.*, 1976, **73**, 278-282.

[8] B.N. Persson, *J. Chem. Phys*., 2003, **118,** 7614-7621.

[9] B.N.J. Persson and S. Gorb, S. *J. Chem. Phys.*, 2003, **119**, 11437-11444.

[10] C.-Y. Hui, N.J. Glassmaker, T. Tang & A. Jagota, *J. R. Soc. Interface,* 2004*,* **1**, 35-48.

[11] E. Arzt, S. Gorb and R. Spolenak, *Proc. Natl. Acad. Sci. USA,* 2003*,* **100**, 10603-10606.

[12] N.J. Glassmaker, A. Jagota, C.-Y. Hui and J. Kim, *J. R. Soc. Interface*, 2004, **1,** 22-33.

[13] B. Yurdumakan, N. R. Raravikar, P. M. Ajayan and A. Dhinojwala, *Chem. Comm.*, 2005, **30**, 3799-3801.

[14] C. Majidi, R.E. Groff, Y. Maeno, B. Schubert, S. Baek, B. Bush, R. Maboudian, N. Gravish, M. Wilkinson, K. Autumn & R.S. Fearing, *Phys. Rev. Lett.*, 2006, **97**, 076103.

[15] A. Peressadko & S.N. Gorb *J. Adhes.*, 2004, **80**, 247-261.

[16] M. Sitti & R.S. Fearing, *J. Adhes. Sci. Technol.,* 2003, **17,** 1055-1073.

[17] S. Kim & M. Sitti, *Appl. Phy. Lett.*, 2006, **89**, 26, 261911.

[18] S. Gorb, M. Varenberg, A. Peressadko & J. Tuma. *J. R. Soc. Interface*, 2006, 1-6.

[19] N. J. Glassmaker, A. Jagota, C.-Y. Hui, W. L. Noderer & M. K. Chaudhury, *Proc. Natl. Acad. Sci. USA*, 2007, **104,** 26, 10786-10791.

[20] B. Aksak, M. Sitti, A. Casell, J. Li, M. Meyyappan, & P. Callen, 2007, *Appl. Phy. Lett.,* **91**, no. 061906.

[21] Y. Zhao, T. Tong, L. Dezeit, A. Kashani, M. Meyyapan, & A. Majumdar, 2006, *J. of Vacuum Science B,* **24** 331-335, No.1 2006

[22] L. Ge, S. Sethi, L. Ci, P.M., & A. Dhinojwala, 2007 *Proc. Natl. Acad. Sci.* USA **104,** 10 792-10 795. (doi:10.1073/pnas.0703505104).

[23] S. Kim, B.Aksak & M.Sitti, 2007 *Appl. Phy. Lett*., **91** 221913.

[24] B. Bharat & A. Robert 2007, *Microsyst Technol* **13** 71-78.

[25] H. Yao, G. Della Rocca, P.R. Guduru & H. Gao, 2007 *J. R. Soc. Interface*, DOI: 10.1098/rsif.2007.1225.

[26] Murphy, M. P.; Aksak, B.; Sitti, Metin, 2007, *J. of Adhes. Sci. and Tech.*, **21**, No. 12-13, 1281-1296.

[27] J. Lee, C. Majidi, B. Schubert, & R.S. Fearing, 2008, *J. R. Soc, Interface*, 10.1098/rsif.2007.1308.

[28] B. Schubert, J. Lee, C. Majidi, & R.S. Fearing, 2008, *J. R. Soc, Interface*, 10.1098/rsif.2007.1309

[29] W.L. Noderer, L. Shen, S. Vajpayee, N.J. Glassmaker, A. Jagota & C.-Y. Hui, *Proc. R. Soc. London, A*, 2007, **463,** 2631-2654.

[30] L. Shen, N. Glassmaker, A.Jagota, & C-Y. Hui 2008, *Soft Matter*, **4**, 618-625.

[31] J. Liu, C-Y. Hui, L. Shen & A. Jagota, 2008, *J. R. Soc., Interface*, 18270150.

[32] A.R. Savkoor & G.A.D. Briggs, *Proc. R. Soc. London, A,* 1977, **356,** 1684, 103-114.

[33] Carpick, R.W., Agrait,N., Ogletree, D.F. & Salmeron, M. 1996, *Langmuir, **12**,* 3334-3340.

APPENDIX 5

Table A.5.1 Nominal contact area of film-terminated samples with different spacing during sliding

Fibril spacing *w* (μm)	Contact 'diameter' (μm)
0 (control)	160
20	360
35	490
50	550
65	520
80	480
110	495
125	470

Table A.5.2 Nominal and actual contact area of roofless samples with different spacing during sliding.

W (μm)	Nominal diameter d (μm)	Actual contact area (m^2)	Dynamic friction (N)
35	487.6003782	2.1E-08	0.5704
50	482.2970773	1.53E-08	0.3408
65	487.6003782	9.9E-09	0.335
80	485.8326112	8.1E-09	0.2591
95	508.8135816	6.9E-09	0.2693
110	510.5813485	5.7E-09	0.2311
125	491.1359121	4.5E-09	0.2193

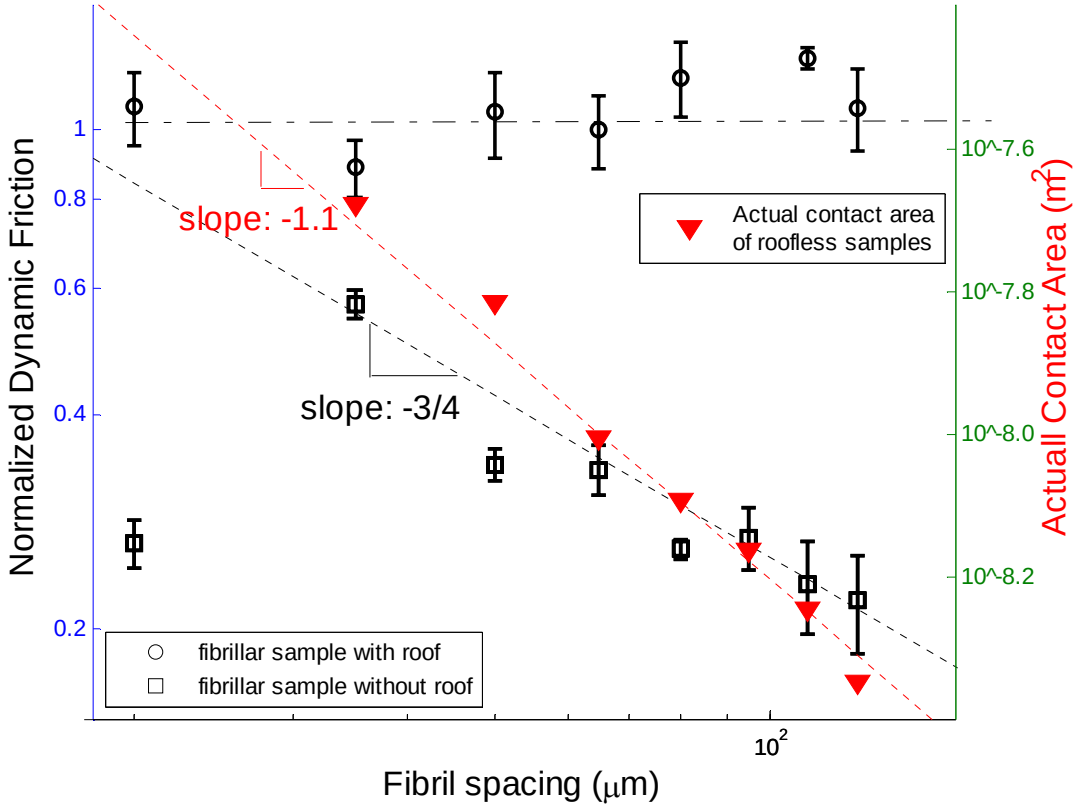

Figure A5.1 Actual contact of roofless fibrillar samples during sliding plotted versus fibrillar spacings.

The nominal contact area for the roofless samples is also approximately independent of fibril spacing as shown in Table A.5.2. For roofless samples it is possible to estimate the actual contact area A^*. As mentioned earlier, there are two types of contacts: one in which the top *edge* of a fibril is in contact with the indenter, in the other the fibrils are in lateral contact. Assuming the area due to edge contact is negligibly small, A^* is estimated by summing the contact area of each fibril inside the lateral contact zone in the video image. These estimates are listed in Table A.5.2 and is plotted in Figure A5.1. The dashed the line indicates $A^* \propto w^{-1.1}$. Included in this plot is the dynamic friction force on sample. Our result shows that the actual area of contact of roofless samples decreases with increase spacing.

CHAPTER 6

SUMMARY AND FUTURE WORK

Indentation experiments are designed to measure the normal adhesion and shear behavior of a film-terminated fibril array. Our experiments showed that normal adhesion is governed by a crack trapping mechanism. Finite element modeling suggested that adhesion enhancement can be controlled by changing the geometry of the microstructure such as fibril spacing, fibril length and film thickness. The shear experiments showed that static friction can be correlated to normal adhesion. The static friction and the normal adhesion energy both increase with the loading rate. The dynamic friction, however, is found to be independent of inter-fibril spacing and has approximately the same value as the flat control sample. In addition, the dynamic friction is approximately independent of the slip velocity. A simple model of a constant friction stress is consistent with our experimental data.

Our two dimensional model of crack trapping is simplistic and cannot capture many aspects of our experiments. For example, it overestimates the adhesion energy and the pull-off force. This is due to the fact that our model assumes that the crack front is a straight line while in reality it is not. Indeed, crack advance is local, that is, not all the fibrils ahead of the crack front fail at the same time. In a three dimensional model, the arrangement of the fibrils in the plane (e.g. a hexagonal pattern versus a square pattern) will lead to different pattern of crack advances, resulting in different adhesion energies. Future work should consider including these features.

Our experimental setup does not allow us to measure the normal load imposed on the cylindrical indenters in our friction experiments. We need to devise a different set up which will allow us to control and to measure the normal load. We also need to

improve our fabrication technique so samples with larger inter-fibrillar spacing can be tested without damage. Further studies on the shear response of the interface should be carried out using more complicated loading paths. We need to develop a theory to study the mechanics of contact under combine normal and shear loading. Such a model will allow us to quantify the transition from static to dynamic friction and to determine how the static friction peak depends on the geometry of the fibrillar structure. This contact mechanics model must address the fact that the fibrils are subjected to very large deformation so linear elasticity theory may not be applicable. Furthermore, our experiments have indicated that local slip occurs in the trailing edge of contact before sliding. This effect should be incorporated in the contact mechanics model.